POLITECNICO
MILANO 1863

School of Industrial and Information Engineering

Master of Science in Mechanical Engineering

An offline algorithm to compensate the geometric error of Staübli TX200 in Incremental Sheet Forming application

Supervisor: Prof. Laura VERGANI

Co-Supervisor: Prof. Eric COURTEILLE

Co-Supervisor: Prof. Dominique GUINES

Adriano ASTARITA

I.D. 842523

Academic Year 2018/19

Ut tensio, sic vis

Robert Hooke

Abstract

In the last decades the purpose of reducing costs, maintaining a high standard quality and an affordable production time, makes Robotized Incremental Sheet Forming (RISF) very attractive for industrial applications. The possibility of using an anthropomorphic robotic arm extremely increases the level of flexibility in terms of shapes and setup times, ensuring evident benefits with respect to standard metal forming procedures. Focusing the plastic deformation in small areas, Forming Limit Curve (FLC) of the material is improved and, at the same time, the forces needed for the machining decreases. On the other hand, this technology is also affected by some drawbacks; in addition to classical problems such as springback and thinning, the implementation of a robotic arm introduces an issue related to its compliance. In order to counteract the dimensional error due to the deformation of the joints, a compensation algorithm must be invoked to match the design requirements.

In this work an approach based on Finite Element (FE) will be used to generate the ideal forces acting on the deforming tool and will be coupled to an elastic characterization of the robot derived by an experimental test. The optimal compliance matrix will be derived by means of an Ordinary Least Square (OLS) optimization and the nominal trajectory will be compensated by using the Hooke's law.

The analyzed specimen is a straight groove having a length of 70 mm and a depth of 10 mm; it is placed at the center of a 270×270 mm 5086-H111 aluminum metal sheet having 1 mm thickness. The piece is machined by a 7.5 mm radius hemispherical punch moved by a 6-axis Staübli TX200.

Keywords: Incremental Sheet Forming, Finite Elements, Staübli TX200

Estratto

Negli ultimi anni, con una crescente attenzione da parte di industrie e ricercatori, l'Incremental Sheet Forming (ISF) ha assunto un ruolo chiave nel panorama delle lavorazioni di lamiere tramite deformazione plastica. Con l'obbiettivo di proporsi come alternativa a tecnologie classiche quali stampaggio e imbutitura, questa lavorazione introduce una serie di benefici che la rendono attrattiva dal punto di vista sia economico che di processo. La principale innovazione introdotta riguarda la metodologia di fabbricazione, che – a differenza dei suoi competitors – avviene tramite una deformazione progressiva della lamiera per mezzo di un utensile che si muove lungo una traiettoria predefinita. Ciò induce una localizzazione delle deformazioni, confinando le concentrazioni di sforzi in zone specifiche e donando una maggiore formabilità al materiale lavorato. La presenza di un utensile di piccole dimensioni che dona al metallo la forma prescelta tramite una serie di passate programmate sostituisce l'esigenza di progettare uno stampo dedicato, diminuendo fortemente i costi e i tempi di sviluppo e rende l'Incremental Sheet Forming la scelta privilegiata per la prototipazione e la produzione di piccoli volumi. L'aumento della capacità di deformazione conferisce al materiale lavorato una maggiore resistenza prima di essere soggetto a rottura. Nel caso dell'alluminio, spesso utilizzato come materiale di riferimento dai ricercatori, si mostrano picchi fino al 120% di elongazione lungo l'asse di deformazione primaria per poi ridursi linearmente all'aumentare della deformazione lungo la direzione di minor deformazione, mantenendosi comunque ben al di sopra dei livelli raggiunti dallo stampaggio.

A seconda del pezzo che si vuole realizzare esistono due principali tecniche che rendono possibile la lavorazione tramite ISF. Forme semplici, caratterizzate da assi di simmetria e geometrie facilmente realizzabili, ricorrono all'utilizzo del Single Point Incremental Forming, che lavora il foglio metallico tramite un unico punto di contatto

rappresentato dall'utensile. Per profili più complessi, invece, si può utilizzare il Two Point Incremental Forming, che introduce una matrice di supporto per facilitare il raggiungimento delle tolleranze richieste, aggiungendo – allo stesso tempo – complicazioni nella strumentazione (come ad esempio la necessità di un' intelaiatura mobile che possa seguire la lavorazione). Il processo di deformazione, in entrambi i casi, viene realizzato tramite l'utilizzo di una macchina a controllo numerico propriamente programmata per percorrere la traiettoria richiesta per la realizzazione dell'oggetto. La struttura estremamente rigida delle CNC permette un elevato livello di dettaglio del prodotto finito e il rispetto delle specifiche geometriche richieste; allo stesso tempo permette l'applicazione di carichi notevoli e un ottimo grado di ripetibilità. Tuttavia la rigidezza della macchina, appena annoverata come punto di forza, richiede d'altro canto una lavorazione fortemente sintetica e priva di un'adeguata flessibilità. Questo fa sì che il processo sia vincolato alla realizzazione di parti che coinvolgono nella lavorazione un numero limitato di gradi di libertà, rendendo così impossibile – ad esempio – la realizzazione di sottosquadri. Negli ultimi anni si è quindi rivolta l'attenzione verso l'utilizzo di robot antropomorfi che, a differenza delle macchine a controllo numerico, sono caratterizzati da un'estrema libertà di movimento e da spazi di lavoro notevolmente più grandi. L'utilizzo di tale strumentazione richiede però una maggiore attenzione al rispetto delle tolleranze geometriche, dal momento che l'elevato numero di giunzioni, ingranaggi e la struttura particolarmente snella dei robot antropomorfi li rende soggetti a deformazioni meccaniche che alterano la performance della lavorazione. La forza idealmente trasmessa dagli attuatori del robot all'utensile e poi alla lamina è infatti redistribuita in due frazioni: una effettivamente trasmessa al pezzo lavorato e un'altra – non trascurabile – assorbita internamente dal robot. Questo comporta un forte disallineamento fra la forma finale desiderata e quella realmente ottenuta. Per affrontare questa tematica e contrastarne l'errore geometrico derivante, possono essere implementate svariate tecniche basate su differenti approcci. Lo scopo di questo lavoro è la definizione di un procedimento offline che permetta di bilanciare le deformazioni interne del robot tramite un opportuno sovradimensionamento della traiettoria di input. Il caso analizzato in questa tesi consiste nell'applicazione, tramite un robot Staübli TX200, di un solco lungo 70 mm, largo 15 mm e profondo 10 mm nel centro di una lamina di alluminio 5086-H111 di spessore 1 mm.

Il primo passo consiste in un accurato studio del processo, atto alla definizione di un modello agli elementi finiti in grado di fornire le forze ideali scambiate tra l'utensile e la lamina nell'ipotesi di assenza di deformazioni interne della macchina. Successivamente si studia il comportamento elastico del robot per definire la matrice di rigidezza complessiva che guida le deformazioni dei componenti meccanici del braccio. Infine, il contributo della deformazione indotta dalla lavorazione è calcolato adoperando la legge di Hooke sulla base dei risultati precedentemente raccolti e viene poi opportunamente sommato alla traiettoria ideale da far seguire al robot per eseguire correttamente il solco.

La simulazione numerica del processo di fabbricazione, sviluppata mediante ABAQUS 6.13, richiede un elevato numero di informazioni riguardanti il materiale coinvolto, la tipologia di lavorazione, i parametri di processo e l'output richiesto. Una caratterizzazione dell'alluminio 5086-H111 è stata quindi svolta per determinarne il comportamento in fase di deformazione plastica, constatando che la legge di Voce appare essere la più coerente per descriverne l'incrudimento. Il sistema di serraggio della placca metallica è stato modellato per determinare la forza trasmessa alla placca stessa da poter utilizzare successivamente come condizione al contorno per la simulazione numerica. La traiettoria è stata selezionata prendendo in considerazione varie alternative; si è infine optato per una traiettoria a *zig-zag*, che incrementa di un millimetro ad ogni passata la sua progressione lungo lo spessore della lamina deformata e allo stesso tempo diminuisce di un millimetro la propria corsa longitudinale. Gli elementi selezionati per discretizzare il modello agli elementi finiti sono stati opportunamente scelti per minimizzare la presenza di *shear locking* e *hourglassing* e garantire la miglior previsione possibile dei livelli delle forze; la placca di alluminio è stata dunque divisa in 5 layers di 0.2 mm ciascuno utilizzando elementi solidi lineari di tipo C3D8R. La densità di elementi utilizzati per riprodurre la lamina è stata variata tramite appropriate partizioni della superficie a seconda dell'incidenza degli sforzi, optando per una distanza dei *seeds* variabile fra 0.5 mm nella zona di principale deformazione fino a 5 mm nelle sezioni periferiche. Il modello è stato progettato sfruttando ogni simmetria e semplificazione in grado di fornire un guadagno in termini di tempo di calcolo senza deteriorare le prestazioni; il risultato è stato un tempo di simulazione di circa 40 ore con una stima delle forze pressocché analoga ai valori ideali attesi. La simulazioneè

stata validata da un test sperimentale utilizzando una macchina a controllo numerico e ipotizzandone un comportamento ideale e senza deflessioni interne.

In parallelo allo sviluppo del modello numerico simulante la lavorazione ideale, sono stati condotti dei test sperimentali di laboratorio per valutare il comportamento elastico dello Staübli TX200. Tramite un sistema di pesi e cavi, il robot è stato sollecitato da diverse combinazioni di carico e ne sono stati misurati gli spostamenti lungo tre assi ortogonali. Dal momento che la matrice di rigidezza è attesa essere funzione della posizione del braccio meccanico, il robot è stato configurato con un posizionamento analogo a quello utilizzato in seguito per l'esperimento. I test di misurazione sono stati ristretti al calcolo delle componenti di traslazione, trascurando le rigidezze torsionali dal momento che l'influenza delle coppie agenti sull'utensile è considerata ininfluente rispetto ai carichi. Mediante un processo di ottimizzazione delle misurazioni effettuate, la matrice di rigidezza dello Staübli TX200 è stata determinata. Un secondo metodo, volto a confermare tale procedura, è stato sviluppato sfruttando le misurazioni ottenute da un test sperimentale svolto in condizioni nominali (cioè senza considerare alcuna compensazione elastica); la traiettoria seguita dalla flangia del robot è stata confrontata con il percorso ideale atteso e – utilizzando le forze provenienti dal modello numerico – una seconda matrice di rigidezza è stata definita. I due output risultano essere confrontabili, confermando la metodologia usata e consentendo il calcolo finale del termine da dover aggiungere alla traiettoria nominale per ottenere la geometria richiesta.

Come ultimo passaggio, le deformazioni attese durante la lavorazione sono state calcolate come prodotto fra la matrice delle forze derivante dal modello ABAQUS e la matrice di rigidezza calcolata sperimentalmente. La traiettoria così compensata è stata trasferita al robot e la lavorazione è stata effettuata. Una discrepanza geometrica è stata comunque riscontrata dai risultati ottenuti dall'esperimento; ma dopo un'attenta revisione della procedura, un errore è stato trovato all'interno del codice necessario per la computazione della traiettoria finale. Incrociando i valori derivanti dall'introduzione dell'errore con l'effettiva deviazione geometrica misurata dall'esperimento, è comunque possibile confermare l'efficacia del procedimento al netto dell'errore umano.

Acknowledgements

In questo giorno speciale, rappresentante il coronamento di un sogno, voglio innanzitutto ringraziare i miei genitori Graziella e Vincenzo per il loro supporto morale, psicologico ed economico. Inutile dire che non sarei qui oggi senza il loro sostegno, i loro sforzi, la loro passione e fiducia in me. Siete il mio orgoglio ed esempio migliore.

Voglio inoltre ringraziare mia sorella Alessandra per la quale, nonostante i litigi giornalieri, provo un affetto speciale e poco convenzionale.

Grazie ai miei nonni e ai miei zii, a chi è qui e a chi non c'è più, per avermi trattato come un figlio in ogni giorno della mia vita.

Grazie ad Andrea e Manuel, i fratelli che ho scelto, per essermi stati sempre accanto nonostante gli anni e le distanze.

Grazie a Sara e Cristina, le mie più care amiche negli anni più significativi della mia vita.

Grazie a Jacopo, Laura e Luca, con i quali ho condiviso i fantastici anni a Milano.

Grazie a tutte le persone incontrate a Lecco durante gli anni della Laurea Triennale.

Grazie a tutte le straordinarie persone conosciute durante l'entusiasmante esperienza di Expo.

Gracias a tutte le persone con cui ho condiviso la fantastica esperienza a Gijón, di cui porteró sempre con me i ricordi.

Merci a tutte le persone incontrate a Rennes durante i mesi trascorsi in Francia per dar vita a questa tesi, che mi hanno aiutato a superare i momenti forse più duri della mia carriera accademica.

E infine un ringraziamento davvero, davvero speciale al mio amore Martina; grazie per ogni sorriso ed ogni attimo trascorso assieme. Grazie per il tuo supporto in questo viaggio, grazie per aver sopportato distanza, giorni bui e giorni tristi. Grazie di esser parte della mia vita.

Inoltre, penso sia doveroso ringraziare la Prof.ssa Laura Vergani per la sua disponibilitá ad essere la relatrice di questa tesi. Allo stesso modo, grazie al Prof. Eric Courteille, al Prof. Dominique Guines e a tutto lo staff del dipartimento Génie Mécanique et Automatique dell'Institut National des Sciences Appliquées di Rennes per avermi dato l'opportunità di lavorare a questo magnifico progetto. Infine vorrei estendere i miei ringraziamenti a tutti i professori del Politecnico di Milano e della Escuela Politécnica de Gijón per avermi trasmesso la passione e le conoscenze che hanno trasformato il mio sogno in realtà.

A tutte le persone che ho menzionato, e a tutte le altre che ho incontrato e conosciuto durante questa fantastica esperienza, voglio dire nuovamente grazie. Grazie, perché senza di voi – senza nessuno di voi – oggi probabilmente non sarei qui e, sicuramente, non sarei la persona che sono adesso.

Grazie. Davvero.

Milano, 3 ottobre 2019

Contents

List of Figures

List of Tables

List of Symbols

A	First Voce's parameter
B	Bottom length of the groove
E	Young's modulus of 5086-H111 aluminum
F_S	Tension of the screw
H	Height of the groove
H_{BH}	Height of the blank holder
L	Top length of the groove
L_T	Length of the tool
N	Number of passes
$R_{BH,int}$	Inner radius of the blank holder
$R_{BH,out}$	Outer radius of the blank holder
$R_{CB,int}$	Inner radius of the circular base
$R_{CB,out}$	Outer radius of the circular base
$R_{S,int}$	Inner radius of the pressure surface
$R_{S,out}$	Outer radius of the pressure surface
R_S	Radius of the circumference hosting the screws
R_T	Radius of the deforming tool
RpP	Groove's horizontal length reduction per pass
S	Pressure surface
T	Tightening torque of the screw
W	Width of the groove
α	Wall angle
$\bar{\sigma}$	Voce's plastic stress
$\bar{\varepsilon}_p$	Plastic strain
$\mathbf{J}$	Jacobian matrix

$\mathbf{\Gamma}$	Torques acting on the joints
$\mathbf{B_{FE}}$	Strain-Displacement matrix of the FE
$\mathbf{E_{CNC/AB}}$	Error between CNC and ABAQUS
$\mathbf{E_{FE}}$	Constitutive matrix of the finite element
$\mathbf{F_{AB}}$	Force matrix (ABAQUS)
$\mathbf{F_{CNC}}$	Force matrix (CNC)
$\mathbf{F_{ID}}$	Ideal forces
$\mathbf{J_{FE}}$	Jacobian matrix of the finite element
$\mathbf{K_q}$	Joints' stiffness matrix
$\mathbf{K_{FE}}$	Stiffness matrix of the finite element
$\mathbf{K}_C$	Complementary stiffness matrix
$\mathbf{K}_R$	Global robot sfiffness
$\mathbf{K}_{R(1)}$	Global robot sfiffness (Method 1)
$\mathbf{K}_{R(2)}$	Global robot sfiffness (Method 2)
$\mathbf{U_{ALG}}$	Compensated trajectory (measured)
$\mathbf{U_{ID}}$	Ideal trajectory
$\mathbf{U_{NT}}$	Nominal trajectory (measured)
$\mathbf{\Delta U_{NT}}$	Deflections of the nominal test
$\mathbf{f}_{ee}$	Forces and torques acting on the end effector
$\mathbf{q}$	Degrees of freedom of Staübli TX200
ν	Poisson's ratio of 5086-H111 aluminum
ρ	Density of 5086-H111 aluminum
σ_Y	Yielding stress of 5086-H111 aluminum
b	Second Voce's parameter
f_{SS}	Sheet-Support friction coefficient
f_{ST}	Sheet-Tool friction coefficient
p	Contact pressure

List of Acronyms

D-H	Denavit-Hartenberg
DoF	Degrees of freedom
FE	Finite Element
FLC	Forming Limit Curve
ISF	Incremental Sheet Forming
OLS	Ordinary Least Square
RISF	Robotized Incremental Sheet Forming
SPIF	Single Point Incremental Forming
TPIF	Two Point Incremental Forming

Chapter 1

Introduction

1.1 State of the art of Incremental Sheet Forming

Incremental Sheet Forming (ISF) was patented in 1967 by Edward Leszak [1], introducing the possibility of forming materials without the use of dies, forms or mandrels. It consists in the shaping of sheet metals by means of a tool movement continuously deforming the material and it represents a valid alternative to conventional manufacturing processes such us stamping and deep drawing. The strength of this technology is its ability to form parts through a localized deformation process, which increases the forming limits of the material and allows a high rate of flexibility in terms of final shapes. The affinity of this technology with CNC machines and the economic advantages due to the usage of low-cost tools instead of tailored punches makes it very profitable for prototyping purposes and for small batch productions.

In the last decades academic researches primary focused on simple geometries characterized by symmetry axis and, in particular, on shapes of revolution such as truncated cones and pyramids. The aim was to understand the main aspects related to this technology and which variables mainly affect the process. Thinning of the material, evolution of the forces during the machining and formability of the materials are the most common process parameters taken into account, but the exact mechanism of the machining is still not well understood.

In order to analyze the deformation behavior, two main approaches are reported in literature: experimental measurements and numerical simulations. Jackson at al. [2] proposed the investigation of deformation mechanism through the analysis of a copper

sheet having a grid along the transversal area in correspondence of the middle of the plate by means of cutting, marking and subsequent brazing of the two halves. Kim et al. [3] used a "non-invasive" procedure defining a grid on the bottom surface of the specimen and analyzing the deformation pattern at the end of the test to define a Forming Limit Curve of the material. Conversely, Allwood et al. [4] proposed a finite element model to describe the evolution of stresses during the process and consequent deformations. Many other examples of numerical models can be found in literature and they all are united by the very high time consumptions.

Thickness of the specimen is often lower than 2 millimeters and the final shape shows a plastic deformation well over the levels achieved by tensile test. Aluminum is the prevailing material used in experiments, but the employment of other alloys – especially titanium – have been investigated for bio-medical [5] and aeronautic [6] applications. A recent and detailed review of the process was presented in 2017 by Li et al. [7].

1.1.1 Key features of ISF

Manufacturing process is performed following a designed path coming from the result of a CAM/CAD software or, for the simpler cases, directly from the analytical trajectory of the geometry. According to the instrumentation used for the machining, Incremental Sheet Forming can be classified in two categories:

- Single Point Incremental Forming (SPIF)
- Two Point Incremental Forming (TPIF)

The difference lies into the adoption of a die supporting the machining; in SPIF this die is not present while it appears in TPIF to help the achievement of suitable tolerances in case of complex geometries. Implementation of such die does not represent a relevant cost, but it may lead to the adoption of different setup (i.e. moving support) and to a different trajectory of the tool.

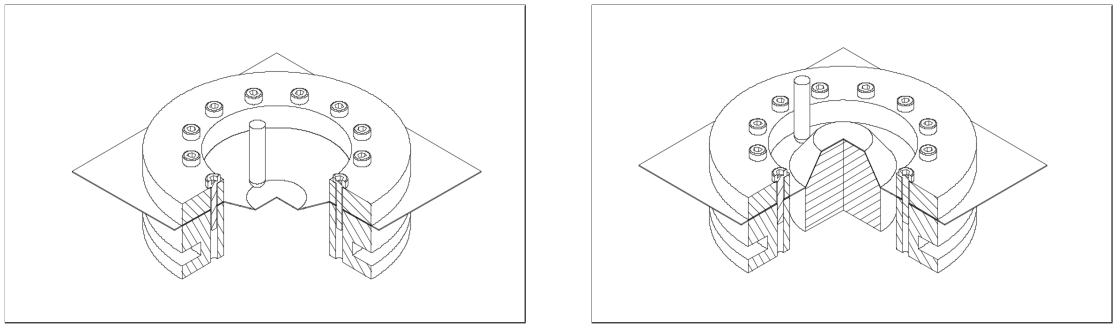

(a) *(b)*

Figure 1.1: SPIF (a) vs TPIF (b)

Regardless the adopted configuration, Incremental Sheet Forming shows important advantages with respect to stamping. Apart from the above-mentioned economic saving, ISF exhibits some mechanical peculiarities making it very attractive for industrial purposes.

The first advantage is the high rate of formability. It is well known that FLC of Incremental Sheet Forming reaches higher values with respect to stamping; an evidence is the analysis made by Filice et al. [8] on 1mm thick AA 1050-O showing a maximum strain of 110% at the collapse point versus the classical 70% achieved through stamping. This is due to the deformation mechanism involved within the process: thanks to the small stressed zone, effects of the machining are ranged in a restricted area allowing a higher global endurance to failure. As explained by Kim et al. [9], the presence of a blank holder allows the assumption of shear-dominant deformation and, consequently, higher deformability is expected. Shim et al. [10] observed the effect of the final shape on formability noting that, in proximity of a corner, equi-biaxial stretching appears while, in correspondence of straight path, plane-strain stretching is the dominant character. By the way, all the studies available in literature agree about the shape of forming limit curve, approaching a straight line with negative slope in the positive quarter of a minor-major strain plot (*Figure 1.2*).

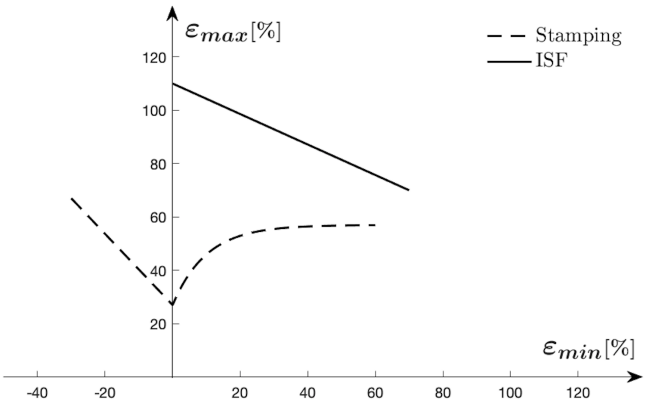

Figure 1.2: Typical Forming Limit Curve of aluminum

The other point of strength is the low level of forming forces and, also in this case, the principal explanation lies in the restricted machined area. Wang et al. [11] demonstrated the absence of correlation between forces and tool path, identifying the increasing depth as a critical aspect. Bagudanch et al. [12] attributed the friction generated by high feed rate of the tool as favorable effect to reduce the forming load. Duflou et al. [13] found a correlation between the high wall angles and the necking appearance, judging it the crucial point from which forces become to drop and specimen starts to fail.

On the other hand, this manufacturing process is characterized by some negative issue that inhibits the extensive appliance of ISF in industry. Due to its functioning, the required time to perform a piece is greater than the one needed by classical stamping and, moreover, the multiple passes generate streaks that drastically affect the surface finish. However, the most relevant diseases related to Incremental Sheet Forming are the excessive thinning and the geometrical errors due to springback. Thinning is related to the variation of volume of the specimen: deformation procedure occurring during the process stretches the surface and, as a consequence, introduces a thickness reduction [14]. Under a theoretical point of view, this phenomenon can be described by the so-called sine law:

$$t = t_0 \cdot sin(90^\circ - \alpha) \tag{1.1}$$

Equation 1.1 simply states a correlation between the original thickness t_0 with the actual thickness t and the wall angle α. By the way, the work of Li et al. [15] showed that real thinning rate is higher than the theoretical one evaluated by the sine law and that the minimum value is reached at a fixed depth. Moreover, Hussain et al. [16] demonstrated that the machining of a part designed with a constant wall angle (frustrated cone for example) allows to reach a higher thinning level with respect to more complex geometries having a varying inclination angle of the surfaces (half-domes, hemispherical profiles, etc.). In addition, Yang et al. [17] found a relation between process parameters and thinning ratio, confirming the main influence of the inclination angle and suggesting the role played by other parameters like the radius of the tool, its feed rate and the step down. All these aspects drastically affect the mechanics of the process and may reasonably explain the divergence between the theoretical formulation of the thickness and the experienced results. Furthermore, as already said, deformation mechanism occurring in ISF is not classified as simple stretching: shear stresses must be thus taken into account in the thinning evolution.

The other crucial drawback is springback and it is due to the mechanism that rules the deformation process. It is well known, in fact, that a specimen subjected to a load experiences a deformation due to the sum of an elastic (and reversible) contribution and a plastic (and irreversible) one. When the load is removed, the specimen is able to partially recover its original shape since the elastic effect vanishes too. Any material follows this trend, but it especially affects sheet metals with high strength-to-modulus ratio, that's the category particularly fitting ISF purposes. In terms of defects, springback appears as a geometric discrepancy between the designed value and the effective one due to the elastic relaxation of the material after the machining. Several techniques were developed in the years accounting feedback control [18] and neural network strategies [19] to balance the deviation between expected and obtained shape.

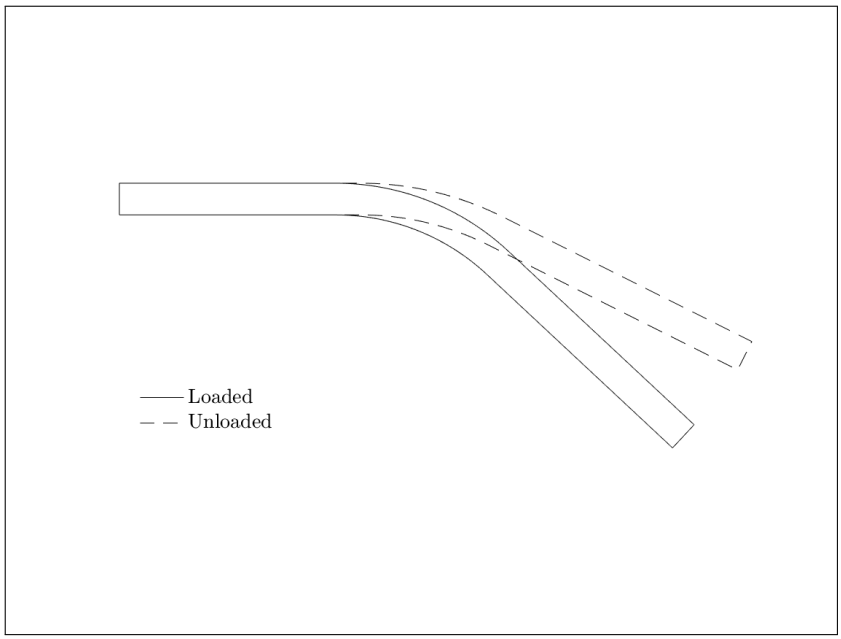

Figure 1.3: Springback effect

1.1.2 Implementation of robotics

Nowadays, the possibility of replacing CNC with serial robots represents one of the most interesting challenges for industrial researchers. The versatility characterizing the robots is the main reason that makes this technology attractive for manufacturers; unlike CNC, a serial robot can easily switch its application and can be adapted to fulfill factory requirements. Thanks to its design, it can be manipulated in order to perform machining involving up to 6 Degrees of freedom (DoF), while a classical numerical control machine is often restricted to 3 or 4. The investment cost is almost equal, but the higher flexibility of a robot plays a determinant role in the associated operational costs and makes it the privileged choice in terms of economic effort. Moreover, serial robots are characterized by working spaces much larger, allowing applications that would be unfeasible for their rivals.

On the other hand, serial robots show unsatisfactory aspects in terms of performances. Today they are not able to reach the same level of payloads of CNC, making them not proper for some industrial applications in which higher machine efforts are required. In addition, the models currently available on the market exhibit lack of accuracy and repeatability, endangering the precision of the machining and the achievement of predefined standard requirements.

In accordance with the considerations mentioned in *Subsection 1.1.1*, the employment of serial robots seems to be a proper choice in case of ISF, since the level of forces required for the machining drastically decreases with respect to other forming processes. High rate of flexibility can be guaranteed by using an anthropomorphic 6-axis robot: it is able, in fact, to freely move in the three-dimensional space combining the translation and the rotation along three orthogonal axis. RISF was proposed the first time by Timo Tuominen in 2004 [20] in order to overcome the restrictions of the classical dieless forming in terms of flexibility. The study was further investigated by Vihtonen et al. [21] that compared different robot-assisted forming methods. But the main aspect currently focusing the attention of researchers is how to counteract the error positioning due to the compliance of robots.

Certain applications such as pick-and-place, polishing, deburring, etc. require a high robot compliance to adapt the exerted force according to the given object; on the contrary, for machining application (requiring univocal force and univocal position) compliance on the end effector is an undesired issue. Online feedback control is a well established methodology to control the position of the end effector; several linear models [22] exist to properly deal with robot compliance and some more sophisticated algorithms [23] can be found in literature accounting nonlinear effects. The weakness of this approach is that, according to the experimental system under analysis, it requires a huge amount of sensors, cables, computing power and a good knowledge of the system. Since is not always possible to access to all the required informations (or it's not cost profitable) other techniques are available based on the experimental evaluation of the stiffness matrix [24]. This second method allows to reduce the cost of the experiment, simplify the instrumentation and use a relatively simple mathematical model; as drawback it requires a huge set of experimental data in different loading configurations to properly estimate the stiffness behavior of the robot.

The common setup for a simple RISF application is characterized by the following elements:

- Anthropomorphic robot
- Pressing device
- Holding mechanism

- Metal sheet
- Controller

The metal sheet is clamped by the holding mechanism and the pressing device – attached to the flange of the robot – moves on the sheet following the instruction provided by the controller. A schematic arrangement of the setup is reported in *Figure 1.4a*. More complex systems can be designed according to the requirements: in case of TPIF a supporting die and a moving support can be added (*Figure 1.4b*) or, as suggested by Maier et al. [25], two robots can be coupled together to perform the machining (*Figure 1.4c*).

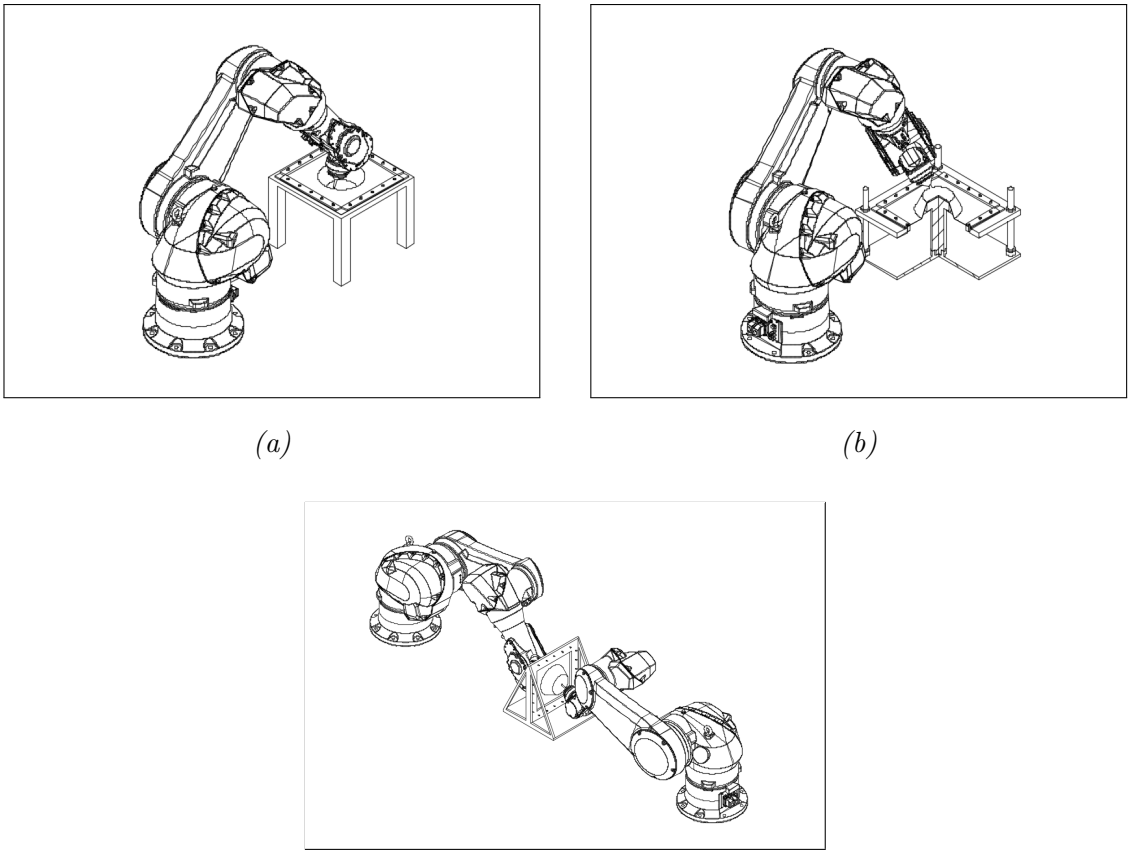

(a) *(b)*

(c)

Figure 1.4: Robotized version of Single Point Incremental Forming (a); Robotized version of Two Point Incremental Forming (b); Example of an advanced configuration of Robotized Incremental Sheet Forming (c)

1.2 Case of study

The aim of this work is to derive a procedure to properly machine simple geometries by means of RISF. The robot used for the test is a Staübli TX200 and the desired final part is a straight groove, dug in a metal sheet, constantly decreasing its length through the depth.

The top length of the furrow L is equal to 70 mm and the width W is defined by the size of the deforming tool having a radius R_T equal to 7.5 mm (i.e $W = 15$ mm). After each pass the horizontal stroke of the robot is reduced of 1 mm and the depth of the part is increased of 1 mm. The machining stops after 10 passes, corresponding to a bottom length of the groove B equal to 61 mm and a height H equal to 10 mm.

The furrow is positioned in the centre of a 270×270 mm 5086-H111 aluminum metal sheet having 1 mm thickness and constrained by a circular clamping system connected to the ground.

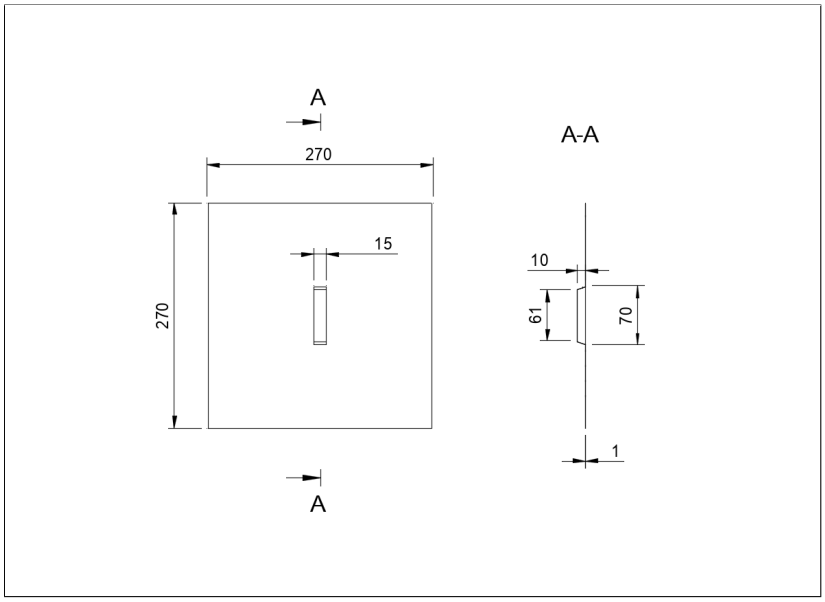

Figure 1.5: Groove (dimensions in millimeters)

1.2.1 Clamping system

Clamping system consists in a ring-shaped blank holder with a height H_{BH} of 25 mm and supported by a concentrical circular base. The internal radius of the two elements $R_{BH,int}$ and $R_{CB,int}$ is equal to 70 mm and they extend till external radii $R_{BH,out}$ and $R_{CB,out}$ both equal to 95 mm. The base is fixed to the upper part by

means of 12 equally spaced M10 screws lying on a circumference – concentric to the clamping system – having a radius R_S equal to 82.5 mm.

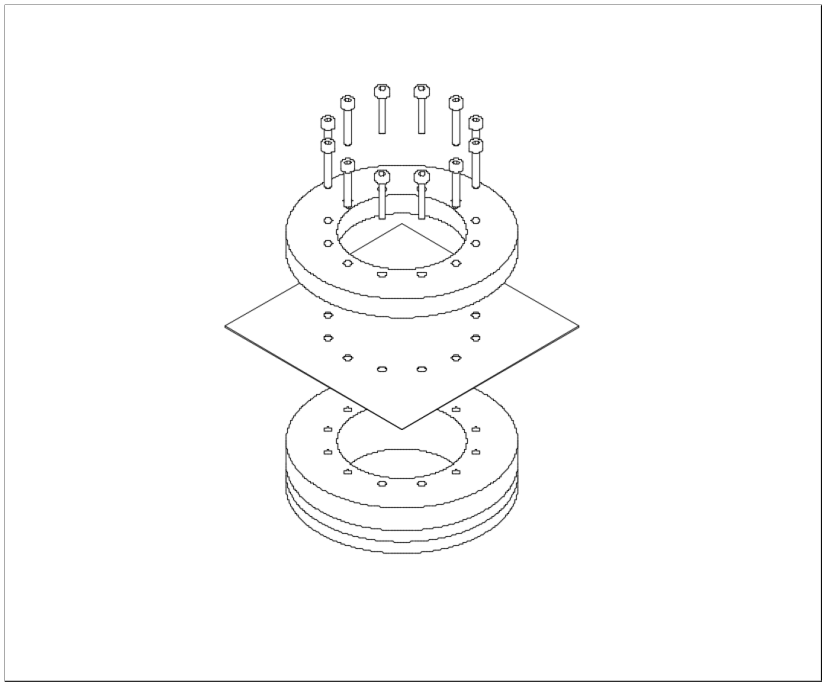

Figure 1.6: Clamping system

The same device was already proposed by J. Belchior in his Ph.D. dissertation [26]. The hypothesis suggested by the author is that, for a good modeling of the tightening, the assumption of encastre between the clamping system and the sheet is not very appropriate; for this reason he describes the interaction between the elements through a pressure model, starting from the empirical equation proposed by J. L. Fanchon [27]:

$$T = F_S \cdot [\ 0.16 \cdot p_S + 0.58 \cdot f_t \cdot D_S + 0.50 \cdot f_h \cdot D_H\ ] \qquad (1.2)$$

The above equation links the tightening torque T to the tension of the screw F_S and its geometrical parameters, where:

- p_S : Pitch of the screw
- f_t : Friction coefficient of the thread of the screw
- D_S : Mean diameter of the body of the screw
- f_h : Friction coefficient between the head of the screw and the blank holder

- D_H : Diameter of the head of the screw

Using a torque wrench is possible to set $T = 20\ Nm$ and then, knowing the geometry of the screws and assuming a value of 0.3 for both the friction coefficients, the magnitude of the force exerted by each screw can be determined ($F_S = 4.60\ kN$). Under the assumption of a pressure cone having an inclination angle of 28° [28], the pressure field on the metal sheet can be assumed quasi-uniform within the circular crown S having the inner radius $R_{S,int} = 70\ mm$ and the outer radius $R_{S,out} = 95\ mm$ (*Figure 1.8*). Contact pressure p acting on the metal sheet can be thus obtained multiplying the force exerted by each screw times the total number of the screws and dividing by the contact surface on which they act, obtaining $p = 4.3\ MPa$.

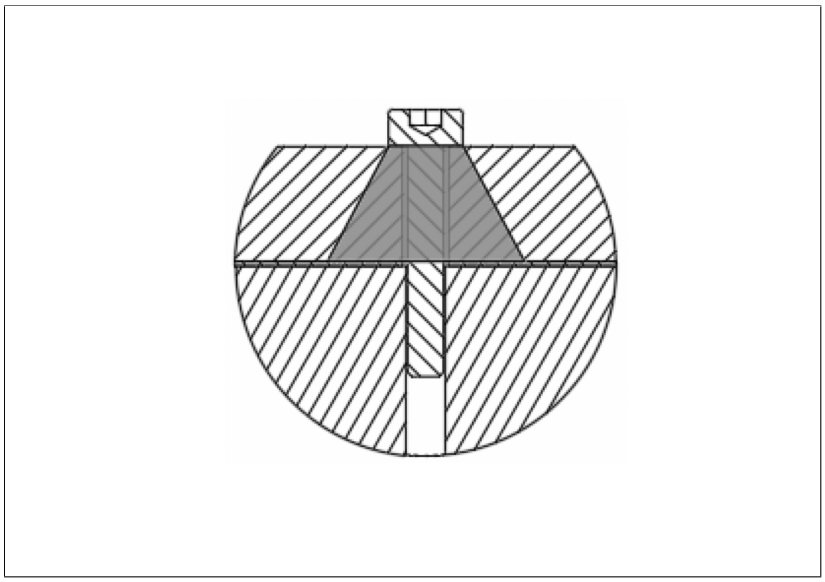

Figure 1.7: Pressure cone

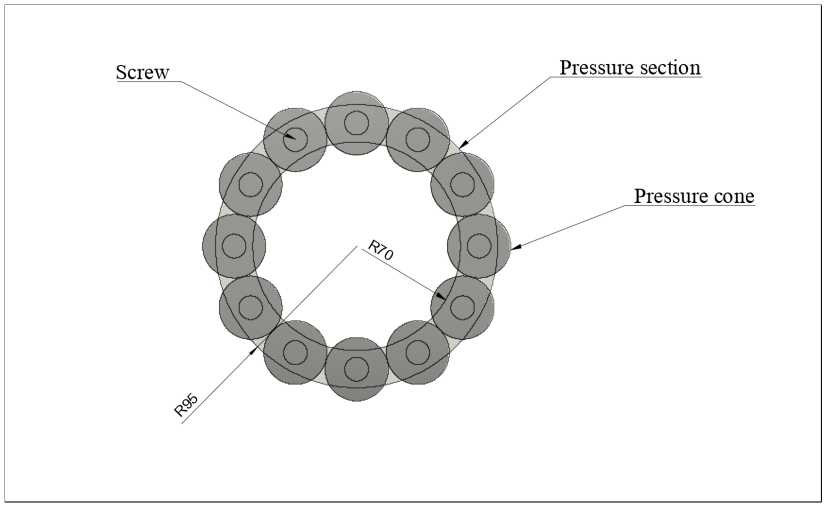

Figure 1.8: Clamping surface

1.2.2 Characterization of 5086-H111 Aluminum

The behavior of the material is a crucial aspect in ISF applications; a detailed knowledge of the deformation mechanism is thus required in order to obtain a feasible mathematical description of the phenomena.

There are a lot of findings in literature regarding the analytic relationship between stress and strain for metallic alloys in plastic domain [29, 30] but they can be roughly classified in two main categories: isotropic hardening and kinematic hardening. In the first class the yield surface only increases its size without changing the shape (*Figure 1.9a*), while in the second class the yield surface translates from its original position accounting the so called Bauschinger effect (*Figure 1.9b*).

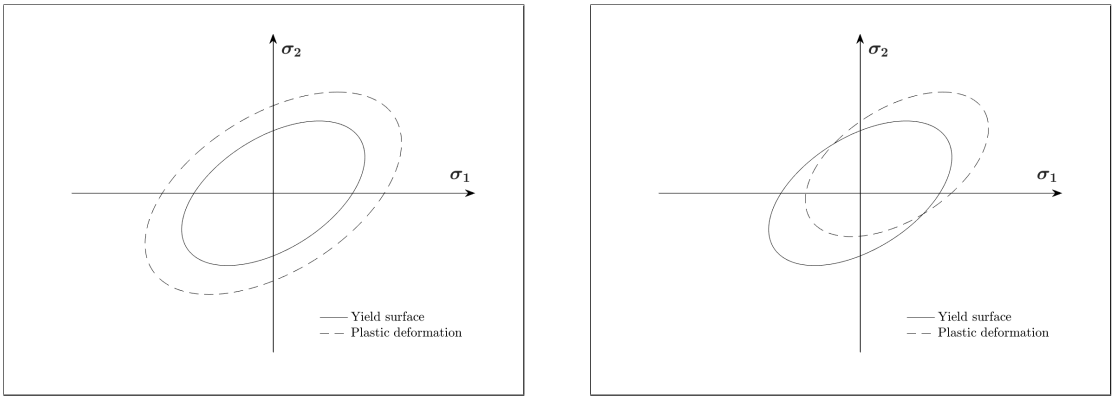

(a) *(b)*

Figure 1.9: Isotropic hardening (a) vs kinematic hardening (b)

A complete description of the forming forces generated by ISF is provided by Henrard et al. [31], which focused the attention on the work hardening of the material through a parametric approach. Zhang et al. [32] investigated the characterization of 5086-H111 aluminum subjected to a wide range of temperatures and identified in Voce's law (*Equation 1.3*) the most coherent description for the hardening of the specimens.

Figure 1.10 shows the asymptotic attitude of Voce's plastic stress $\bar{\sigma}$ to reach a saturation value and then to remain constant for any increasing plastic strain $\bar{\varepsilon}_p$. The mathematical law is ruled by the yielding stress σ_Y and by two parametrs A and b reported in *Table 1.1*.

$$\bar{\sigma} = \sigma_Y + A \cdot \sqrt{1 - e^{-b \cdot \bar{\varepsilon}_p}} \tag{1.3}$$

Voce's parameters for 5086-H111 aluminum

Yielding stress	σ_Y	130.2 MPa
First Voce's parameter	A	300.37 MPa
Second Voce's parameter	b	3.94

Table 1.1: Voce's parameters for 5086-H111 aluminum

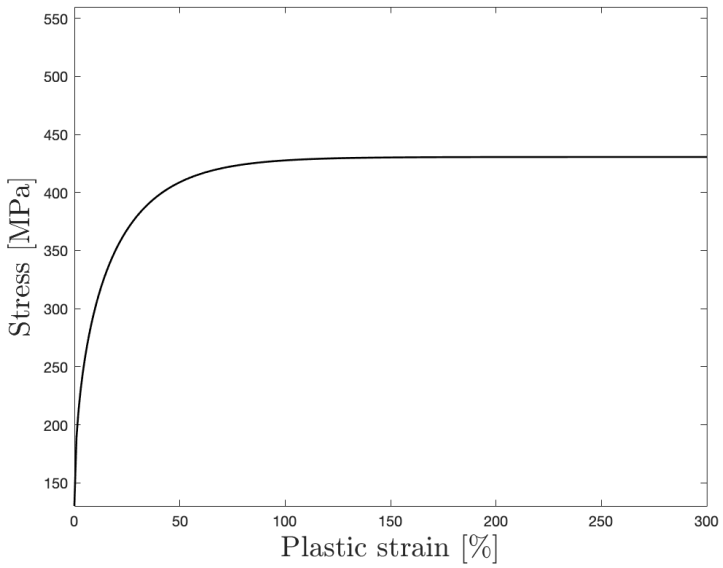

Figure 1.10: Voce's hardening law

In addition, Belchior et al. [33] tested incremental sheet forming on the same aluminum alloy, proving a quasi-isotropic plane behavior and a low transversal thickness anisotropy. Based on these results, an isotropic behavior will be assumed also in this work and Voce's law will be used to describe the plastic deformation of the plate.

Mechanical parameters of 5086-H111 aluminum

Young's modulus	E	66 GPa
Poisson's ratio	ν	0.3
Density	ρ	2.7 kg/dm^3

Table 1.2: Mechanical parameters of 5086-H111 aluminum

1.2.3 Trajectory

As a general rule, the pattern followed by the tool should be generated by a CAM software; but in the considered case the geometry is sufficiently simple that is possible to use a mathematical description of the trajectory. Once the dimensions of the groove are defined, the feed of the tool must be imposed. Two possibilities are taken into account: a constant increment of the depth within the pass and a step increment of the depth at the beginning of each pass.

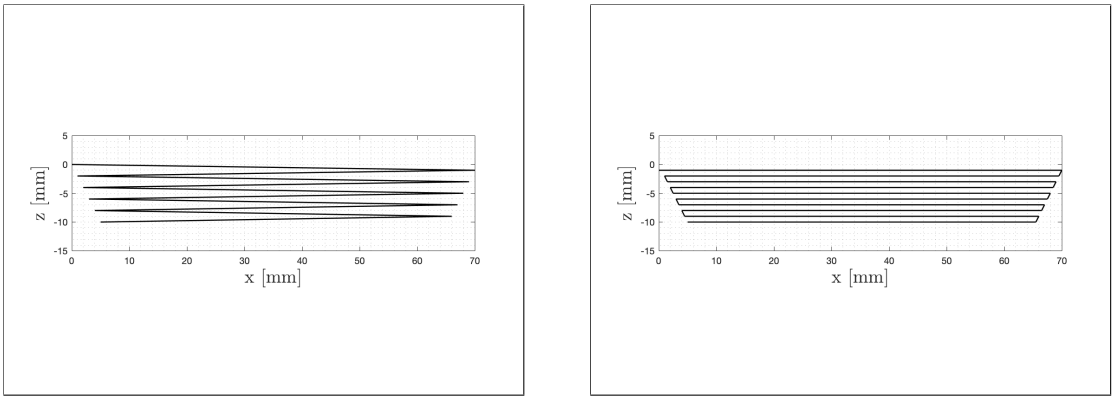

(a) *(b)*

Figure 1.11: Constant increment (a) vs Step increment (b)

The difference lays in the interaction between the pressing device and the sheet. In the first case the contact is smooth and the forming head progressively penetrates the metal sheet; shear stress plays a dominant role, dislocations are favored and vertical

force reaches acceptable values. Vice versa, in the second case the interaction is brute and stretching appears leading to higher vertical force values, especially in the first part of the stroke. Thereby, the first option is selected.

Other important parameter is the feed rate; selecting a velocity slow enough, it's possible to assume a quasi-static behavior of the process. Velocities commonly used in metal forming applications are generally in the range of $1 \div 2$ m/min and this simplification allows to strongly simplify the analysis. The feed rate of the tool will be selected equal to 2 m/min for the numerical test but will be reduced in the experimental test according to the robot capabilities (saturation of the actuator due to the high discretization of the trajectory). Anyway, under the hypothesis of quasi-static process any reduction of the feed rate will not affect the results.

1.3 Stages of the experiment

The experiment can be schematized in three main stages:

- The first part will concern the achievement of a model able to estimate the ideal forces exchanged by the end effector and the worked surface during the whole process. The trajectory of the tool will be computed and, through a FE environment, a realistic simulation of the machining will be generated taking into account all the main parameters affecting the metal forming. To validate the model the numerical curve will be compared with an experimental test performed on a CNC machine assuming a rigid behavior of the machine.

- The next step will focus on the robot side. The trajectory will be "translated" in robot language and an equivalent test will be preformed using the Staübli TX200: the output will be affected by the compliance of the joints, resulting in a wrong machining of the part. The path and the forces measured on the tool during the process will be stored and used as input for the third phase.

- The data collected during the robot machining will be compared with the ideal simulation and – by means an optimization procedure – a feasible compliance matrix will be derived. Some experimental tests will be carried out in parallel to estimate the same compliance matrix in a different way and the two results will

be compared. The initial trajectory will be adjusted by adding a term related to the internal deflection of the joints obtaining a compensated trajectory able to correctly machine the desired part. A new experiment will be performed and a new numerical model will be designed accounting the deflections of the robot to confirm the procedure.

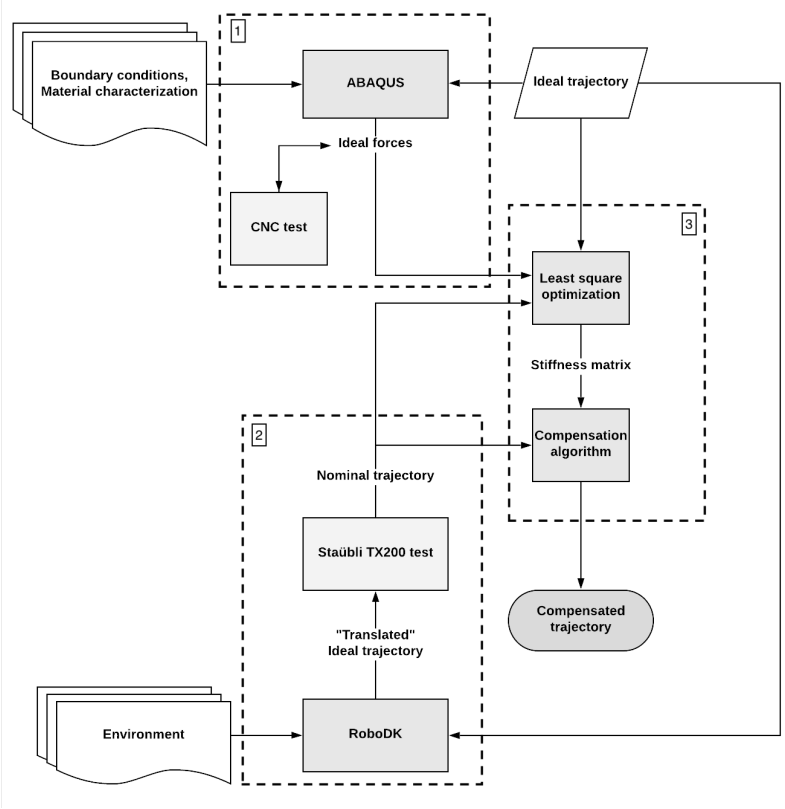

Figure 1.12: Scheme of the work

1.3.1 Stage 1: FE simulation and model validation

The trend of the forces is drastically affected by the deformation mechanism of the plate during the machining. A good knowledge of the phenomena appearing within the metal sheet is thus required to perform a suitable simulation of the process.

Once the material has been characterized, the boundary conditions have been defined and the trajectory has been chosen, an analysis of the forming process is needed. In this regard, Emmens [34] proposes a complete review on the possible effects, identifying four main aspects: through-thickness stress, contact stress, bending under tension and cyclic effect. A feasible FE model must consider these issues in order to

choose the proper type of elements, the integration method, the type of analysis and any relevant characteristic for the description of the process. Any choice will affect the weight of the model, for this reason a good trade-off between performances and time consumption is necessary. Such evaluations will be the topic of the first part of *Chapter 2*.

The second part of the chapter will focus on the definition of the model in terms of geometries, interactions among parts, boundary conditions, etc. Symmetries will be underlined to lighten the model and any component of the setup will be properly meshed. The output of the simulation will be compared with the experimental results of an equivalent ISF test performed on a FAMUP MCX600.

1.3.2 Stage 2: Nominal trajectory using Staübli TX200

Chapter 3 will start with the characterization of Staübli TX200: being a 6-axis robot, it is able to freely move in each space direction with any possible orientation according to its dimensional constraints. An overview of its working space and singularities will be exploited and then – following the Denavit-Hartenberg formulation – the kinematic model of the robot will be presented.

Afterwards, Staübli TX200 will be set for the experiment. By means of RoboDK, laboratory environment will be digitally reproduced and the trajectory for the end effector will be produced with a Phyton code. RoboDK will allow to generate the G-code containing all the information needed to the robot to follow the required instructions and the code will be implemented on the controller. An experimental test will be thus performed in order to evaluate the stiffness deviation. The same force sensor of the previous test will be used and, in addition, movements of the end effector will be tracked thanks to a triangulation camera.

1.3.3 Stage 3: Error compensation and final trajectory

The third part of the work concerns the study of the compliance of Staübli TX200. A general model to describe the joint stiffness matrix will be presented and a new procedure to estimate the stiffness matrix will be exposed, following a numerical optimization based on ordinary least square method. Once the results of the kinetostatic analysis are available, the deviation term due to the compliance of the robot can be

simply evaluated and summed up to the nominal trajectory. In this way the compensated trajectory can be easily obtained; this trajectory will overestimate the ideal one and, implementing it on the controller of Staübli TX200, the machining is expected to be optimal.

Chapter 2

Modeling of the ideal process

2.1 ABAQUS background

The entire numerical analysis is performed using ABAQUS 6.13. The definition of the model starts with the choice of the elements, the integration method and the mathematical theory used to define the element behavior. Several options are available in the ABAQUS library and the decisions must reflect the nature of the problem under analysis. The degree of complexity of the parameters selected for the simulation may drastically affect the result; some aspects may be accidentally underestimated or completely neglected according to these primary choices. Vice versa, some behaviors may be magnified and distort the output accounting non realistic effects. The computational time may significantly increase due to unnecessary mathematical steps and the analysis may become obsolete or unfeasible.

The reader can thus understand the importance in the decision of this framework of the model.

2.1.1 Types of elements

Regardless the element type associated to the problem, the procedure solution is still the same. The philosophy of finite elements method is to discretize a continuum problem into a countable set of unknowns and reconstruct the complete response starting from these finite number of points. The original structure is thus divided in several simple elements connected one to each others by means of characteristic points called *nodes*. How to discretize the structure is the first issue that has to be solved.

ABAQUS classifies all the possible types of element in families, grouping them according to their geometry and the number of spatial dimensions (*Figure 2.1*).

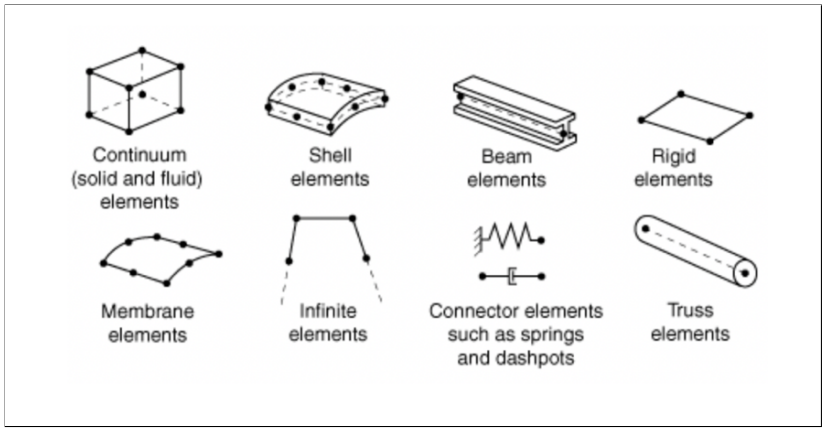

Figure 2.1: Element families [35]

According to the modeling of the structure, the typical mechanical analysis usually restricts the choice to continuum elements and shell elements only. Continuum element discretizes the system using 3D bricks, while shell element simplifies the domain to only two dimensions, introducing a strong simplification in terms of calculations. The implementation of shell elements is commonly accepted if one dimension is at least 10 times smaller than the others and admits some differences in the schematization of the problem.

Dynamics of finite elements follow the so called *isoparametric formulation* that corresponds to a transformation from the global reference frame $\mathcal{F}(x, y)$ to a local frame within the single element $\mathcal{F}(\xi, \eta)$. It allows to deal in a simpler way the distortion of the elements, relating local displacements and strains with the global reference frame. Horizontal and vertical displacements u and v derive from the definition of the shape functions (defined in the local frame of the elements) and strains are determined evaluating the partial derivatives with respect to the reference coordinates. Since the goal is to define the strains in global reference frame, chain rule is adopted to find the relationship between the derivatives of the displacements from the local to the global reference frame. For example, taking into account the horizontal displacement of the node:

$$\frac{\partial u}{\partial \xi} = \frac{\partial u}{\partial x} \cdot \frac{\partial x}{\partial \xi} + \frac{\partial u}{\partial y} \cdot \frac{\partial y}{\partial \xi} \tag{2.1}$$

$$\frac{\partial u}{\partial \eta} = \frac{\partial u}{\partial x} \cdot \frac{\partial x}{\partial \eta} + \frac{\partial u}{\partial y} \cdot \frac{\partial y}{\partial \eta} \tag{2.2}$$

Collecting *Equation 2.1* and *Equation 2.2* in matrix form, the so called Jacobian matrix $\mathbf{J_{FE}}$ is derived.

$$\begin{Bmatrix} \frac{\partial u}{\partial \xi} \\ \frac{\partial u}{\partial \eta} \end{Bmatrix} = \begin{bmatrix} \frac{\partial x}{\partial \xi} & \frac{\partial y}{\partial \xi} \\ \frac{\partial x}{\partial \eta} & \frac{\partial y}{\partial \eta} \end{bmatrix} \cdot \begin{Bmatrix} \frac{\partial u}{\partial x} \\ \frac{\partial u}{\partial y} \end{Bmatrix} = \mathbf{J_{FE}} \cdot \begin{Bmatrix} \frac{\partial u}{\partial x} \\ \frac{\partial u}{\partial y} \end{Bmatrix} \tag{2.3}$$

Since the variables of interest are strains in global reference frame, *Equation 2.3* has to be inverted requiring a non-null determinant of $\mathbf{J_{FE}}$. Under a physical point of view, the determinant of the Jacobian is a scale factor able to quantify the distortion of the element. A null determinant implies the annihilation of the element to a single point, a negative determinant indicates that a part of the element is projected outside the boundaries of its local frame.

Formulation of shell elements helps the achievement of positive Jacobian determinant, avoiding convergence problems during the analysis and strongly simplifying the computations. Shells are characterized by translational and rotational degrees of freedom, whereas solids only have translational ones. This implies a better behavior of shell elements under bending conditions, reproducing the gradient stress across the thickness. By the way, shell elements are not convenient for nonlinear analysis and, moreover, the localized deformation process under analysis makes the hypothesis of thin plate no further reliable. Experience suggests a global stiffer behavior of shell model with respect to ISF tests and finds in solid elements a better choice for simulations.

2.1.2 Shape functions and bending description

Adopting continuum elements for the analysis, some considerations on the bending mechanism are mandatory to well understand how ABAQUS deals with this phenomena. The software provides two main possible classes of elements: linear elements

and quadratic elements (a third class called modified second-order interpolation exists, but will not be treated in this work). The difference concerns the number and the position of the nodes within the element; linear element has a node in each vertex, while quadratic element has additional nodes placed in the middle of each edge. In a mathematical sense, the distinction lies in the order of the polynomials describing the displacement of the element between one node and the other (i.e. the shape functions): linear elements refer to first order polynomials, quadratic elements use second order functions.

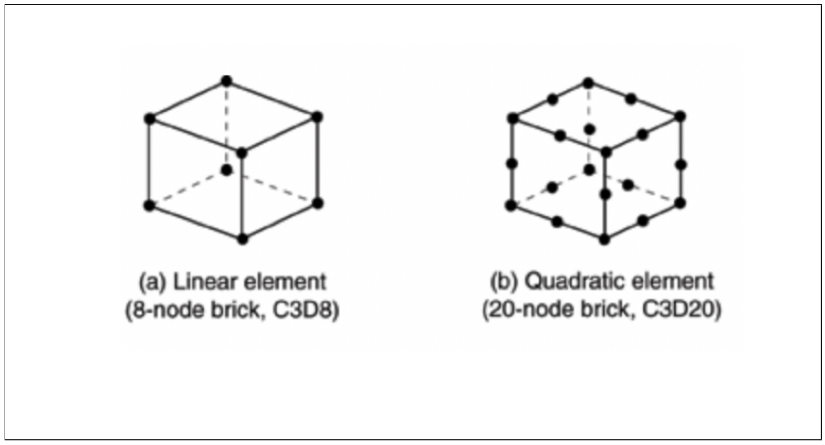

Figure 2.2: Order of interpolation [35]

Mathematical description of pure bending assumes a linear distribution of the strain along the axial direction with a null value in correspondence of the neutral axis. Moreover, plane cross-sections are assumed to remain plane throughout the deformation and no membrane shear strain is allowed; the latter assumption implies that the virtual lines parallel to the neutral axis lie on a circular arc.

According to this formulation and accounting the properties of solid elements, quadratic solid elements should be used in presence of bending to have a reliable simulation of the process. However this choice implies a significant weighting of the model that cannot be accepted for test involving nonlinear dynamics. In order to understand how to select linear elements for the analysis, the concept of Gauss quadrature has to be introduced.

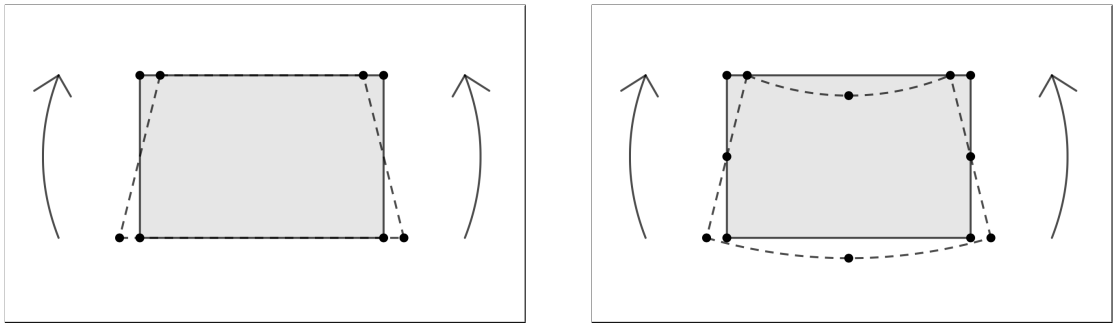

(a) *(b)*

Figure 2.3: Linear (a) and quadratic (b) elements subjected to bending

2.1.3 Integration method

The solution of FE problem goes through the evaluation of an integral expressing the stiffness matrix $\mathbf{K_{FE}}$ of the element [36].

$$\mathbf{K_{FE}} = \int_V \mathbf{B_{FE}}^T \cdot \mathbf{E_{FE}} \cdot \mathbf{B_{FE}} \, dV \tag{2.4}$$

Equation 2.4 comes from the classical formulation of stiffness as function of strains ($\mathbf{B_{FE}}$ represents the strain-displacement matrix derived from the shape functions) and the constitutive matrix $\mathbf{E_{FE}}$. A detailed discussion on how matrices $\mathbf{K_{FE}}$ and $\mathbf{B_{FE}}$ are computed can be found in *Appendix A*.

A common way to numerically solve an integration problem is the Gauss quadrature: it finds the solution of the integral reducing the computation to the sum of a finite number of terms.

$$\int_{L_\xi} \Phi(\xi) \, d\xi \approx \sum_i^n W_i \cdot \Phi(\xi_i) \tag{2.5}$$

W_i represents the weight associated to the $\Phi(\xi_i)$ discrete point of the generic function $\Phi(\xi)$ integrated along the domain L_ξ and n is the number of points with which the function is discretized.

If $\Phi(\varepsilon)$ is a polynomial, the exact value of the integral can be evaluated using a number of point able to satisfy *Equation 2.6*.

$$m \leq 2 \cdot n - 1 \tag{2.6}$$

With m the degree of the polynomial.

If $\Phi(\xi)$ is not a polynomial, the result is an approximation and the accuracy improves increasing the number of points (but the convergence may not be monotonic). In the same way, the procedure can be extended for the bidimensional element having an area $A_{\xi\eta}$ discretizing the polynomial in correspondence of $\Phi(\xi_i, \eta_j)$ for a total number of points equal to n^2 (and also for the 3D case using n^3 points).

$$\iint_{A_{\xi\eta}} \Phi(\xi, \eta)\ d\xi\ d\eta \approx \sum_{i}^{n} \sum_{j}^{n} W_i \cdot W_j \cdot \Phi(\xi_i, \eta_j) \tag{2.7}$$

n	Φ_i	W_i
1	0	2
2	$\pm\frac{\sqrt{3}}{3}$	1 ; 1
3	$\pm\sqrt{0.6}$; 0	$\frac{5}{9}$; $\frac{8}{9}$
4	± 0.861 ; ± 0.340	0.348 ; 0.652

Table 2.1: Parameters for Gauss quadrature over the interval $\xi = \pm 1$

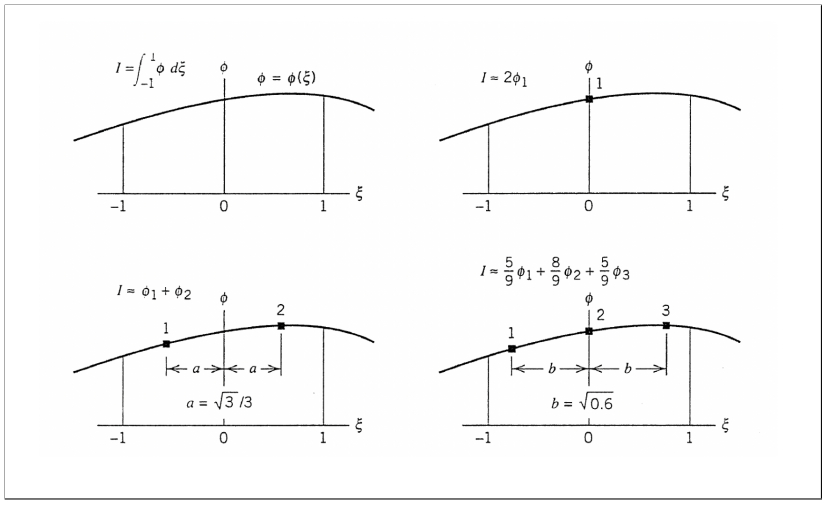

Figure 2.4: Integration points for one-dimensional element [36]

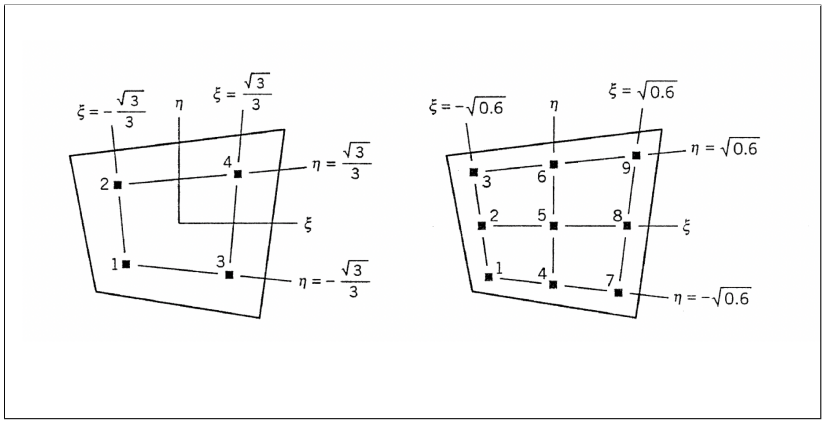

Figure 2.5: Integration points for two-dimensional element [37]

FE method evaluates every variable of interest in correspondence of Gauss points and then extrapolates the results to the whole element by means of the shape functions.

ABAQUS proposes a fully integrated linear brick element (C3D8) characterized by $n = 2$, for a total number of 8 Gauss integration points. Due to the mathematical formulation of the element, the edges must remain straight also in bended configuration, introducing a violation of the orthogonality of the isoparametric lines (*Figure 2.7*). As a consequence an overly stiff behavior results, since the energy contained in the element tends to shear the brick instead of bending it; this effect is called *shear locking.*

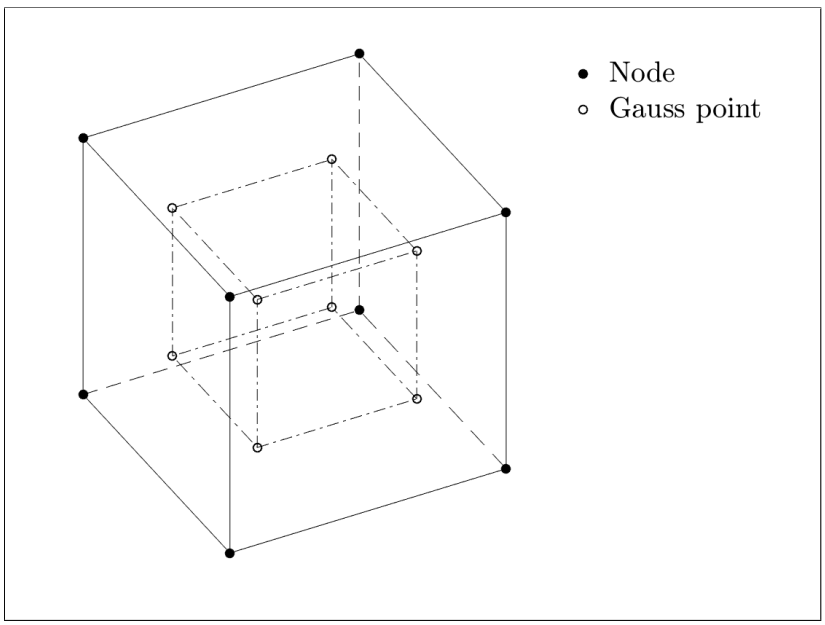

Figure 2.6: C3D8 element

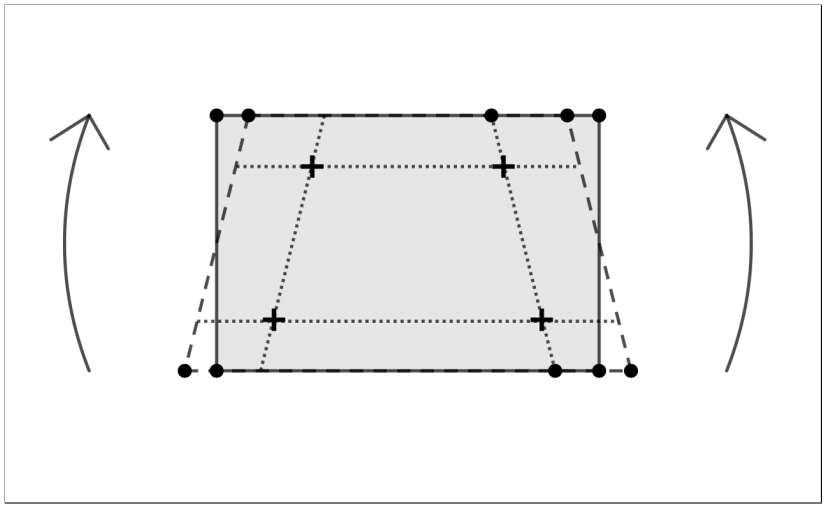

Figure 2.7: Shear locking

A solution to this issue is given by the element C3D8R. It is a linear brick element characterized by a reduced integration; it means that it is characterized by a single integration point placed in the centre of the brick. Thanks to its position, isoparametric lines in the Gauss point remain perpendicular also when the element is subjected to bending. It allows to eliminate shear locking, but – at the same time – it introduces another problem: *hourglassing*. The particular position of the integration point provides a null deformation of the element in that point (deformed isoparametric lines coincide with the non-deformed configurations); the result is that the element experiences a global deformation but no strain is associated to the process.

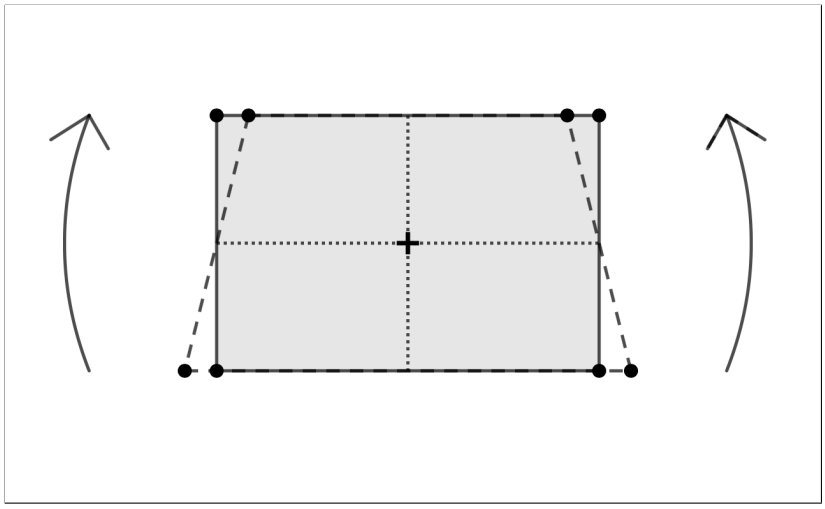

Figure 2.8: Hourglassing

An effecting way to reduce hourglassing is to model the thickness by means of

multiple elements. In this way each element detects compressive or tensile strain but not both. At the same time, axial strain can be correctly measured and no shear strain appears. It is an effective way to model structures subjected to bending, since it describes an optimal tradeoff between computational time and accuracy of the results.

That's the reason why it represents the choice selected for this work.

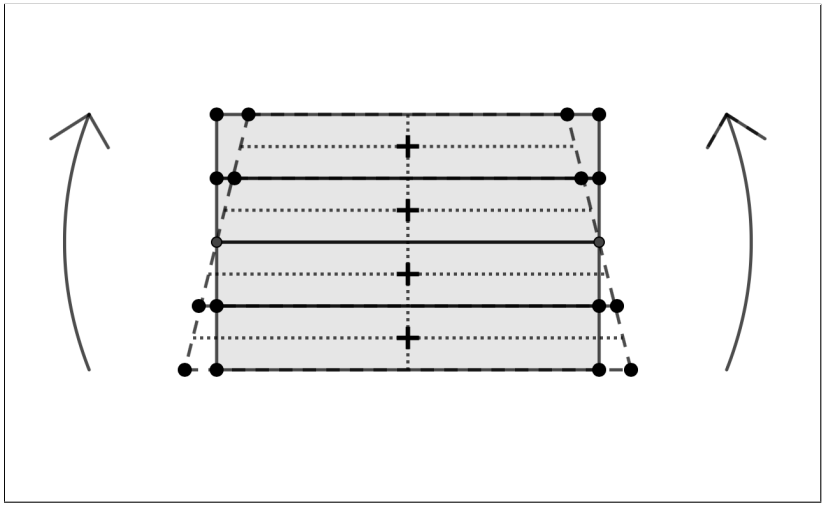

Figure 2.9: Multiple C3D8R elements through the thickness

2.1.4 Meshing techniques

ABAQUS provides different algorithms to propagate the mesh through a defined geometry. The choice is related to the complexity of the part and the element shape selected for that region. The default criterion is the *top-down* meshing, defined by the software user's manual as follow: "*top-down meshing relies on the geometry of a part to define the outer bounds of the mesh*" [35]. As alternative, for more complex cases, *bottom-up* criteria can be used; in this case the part geometry is used as a guideline for the outer bounds of the mesh, but no constraints are imposed to the mesh about the conformity to the geometry.

The model of this case of study – presented in the next section – follows the top-down criterion, using different strategies for different regions. Three different options are available on ABAQUS:

Structured meshing It provides the higher control and forecasting of the mesh. Structured meshing adapts the actual geometry to a sampling topology selected from

a set of elementary meshed geometries. This technique allows to mesh simple bidimensional regions and can be extended to simple three-dimensional regions using Hex or Hex-dominated element shape option.

Swept meshing It allows the definition of the mesh for complex 2D or 3D parts. An edge or a face is initially meshed (source side) and then is propagated till the target side, following a sweep path.

Free meshing It represents an alternative to structured meshing and allows the meshing of complex parts without any predefined pattern. Three-dimensional parts meshed using tetrahedral element shape follow this meshing technique. It represents the most flexible methodology, making difficult any prevision about the final mesh mapping.

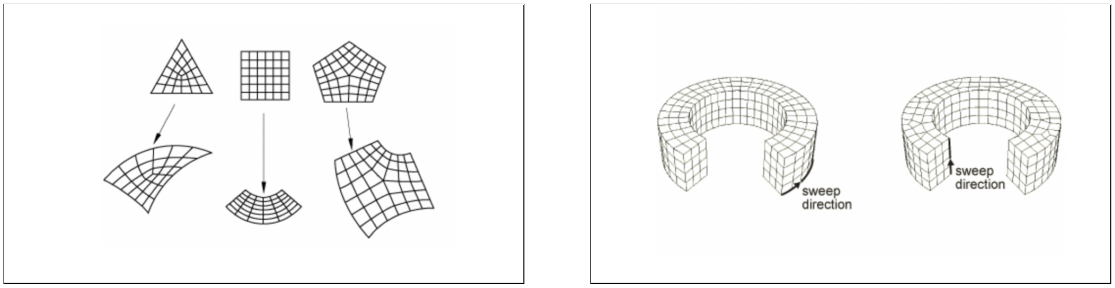

(a) *(b)*

Figure 2.10: Structured meshing (a) and swept meshing (b) [35]

2.2 Finite elements model

The main geometrical parameters of this case study (already presented at the beginning of *Section 1.2*) are collected in the following two tables: setup parameters are listed in *Table 2.2*, while *Table 2.3* shows all the information referred to the groove.

Component	Symbol	Size
Aluminum sheet	-	$240 \times 240 \times 1\ mm$
Tool radius	R_T	$7.5\ mm$
Inner radius of the clamping device	$R_{BH,int}$	$70\ mm$
Outer radius of the clamping device	$R_{BH,out}$	$95\ mm$

Table 2.2: Geometrical parameters of the instrumentation

Dimension	Symbol	Size
Length of the groove	L	$70\ mm$
Width of the groove	W	$15\ mm$
Height of the groove	H	$10\ mm$
Wall angle	α	$63.43°$

Table 2.3: Geometrical parameters of the final part

The wall angle α equal to $63.43°$ is obtained taking into account the height of the final groove, a groove's horizontal length reduction per pass $RpP = 1\ mm$ and a total number of passes $N = 10$. It follows the formulation of *Equation 2.8*, considering a constant increment of the depth of $1\ mm$ each pass.

$$\tan(\alpha) = \frac{H \cdot 2}{N \cdot RpP} \tag{2.8}$$

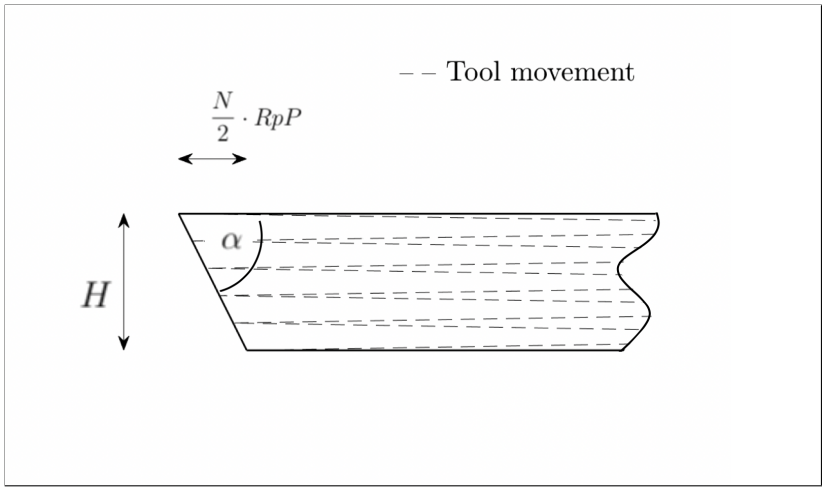

Figure 2.11: Wall angle

The geometry implemented in the analysis coincides with the area encircled in the clamping system; outside this limit, in fact, the metal sheet is unloaded and essentially useless for computation purposes. The assembly is composed by three parts: the circular support (which is considered connected to the ground), the aluminum sheet and the deforming tool. The blank holder is directly modeled as the pressure that it exerts on the structure, following the formulation exposed in *Subsection 1.2.1.*

The shape of the components involved in the process, the loading condition applied to the structure and the trajectory followed by the tool make the system symmetric along the diameter of the blank holder aligned as the axis of the groove. This consideration allows a strong simplification of the model, leading to *Figure 2.12.*

The contact between the support and the sheet is designed considering a friction coefficient $f_{SS} = 0.2$ [26], while the interaction between the tool and the sheet f_{ST} is assumed equal to 0.1 (lubricant is used in the experiment). The assumption of quasi-static process allows to neglect all the parameters related to the dynamics of the process such as the damping and the mass of the components.

The support and the deforming tool are considered as rigid body, while the metal sheet is modeled as a deformable body and is characterized by its Young's modulus and Poisson's ratio. As already mentioned, the material is assumed as isotropic.

At the beginning of the simulation the tool is considered in contact with the lamina and it is not able to move, then the pressure is applied to simulate the clamping and finally the machining starts. Some preliminary tests were also performed accounting a step increment of the trajectory; in that cases the initial contact between the tool

and the metal led to the divergency of the analysis. To counteract this instability, an additional touching phase was implemented. By the way, no problems were found during the simulation involving the constant-increment trajectory: since the latter was selected as final choice, the additional touching phase mentioned before was omitted to simplify the simulation.

ABAQUS simulation is aimed at estimating the deforming forces exchanged in correspondence of the contact point between the aluminum sheet and the tool. On this regard an important consideration is mandatory; since the contact point lays on the symmetry plane of the model, data obtained by the simulation must be doubled along the thickness direction and the in-plane machining direction. Vice versa, the force obtained along the direction normal to the symmetry plane has to be summed to its complementary.

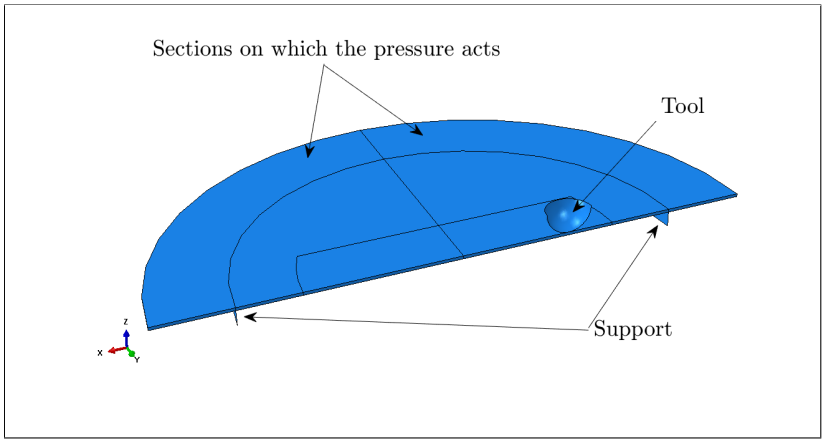

Figure 2.12: Model used for the simulation

2.2.1 Mesh definition

The result of the numerical simulation is very sensitive with respect to the mesh size. A great number of elements leads to a more accurate analysis, but it requires a huge amount of computational time: a proper trade-off has to be found.

Essentially, element dimension further affects the output of the regions subjected to large deformations. Rigid parts do not need a special attention to the meshing, while the metal sheet represents the bottleneck of the analysis. In particular, the central part of the lamina – on which the tool acts – requires a particular consideration with respect to the peripheral part that is not primary involved in the machining.

Tool and support have been designed as rigid bodies using shell formulation. The elements used to discretize the bodies are R3D4, that are 4-node bilinear quadrilateral elements working in 3D modeling space. Only the global dimension of the parts is taken into account to define the proper distance between the seeds of the mesh. According to the geometry of the tool, an approximate distance of 1 mm is enough to properly define the object; a total number of 237 nodes is generated and connected through 208 R3D4 elements. 8 additional linear triangular elements of type R3D3 are generated to effectively fit the surface of the tool. Concerning the support, an approximate distance of 11 mm in the circumferential dimension is set: 120 R3D4 elements are generated imposing a single element along the radial component.

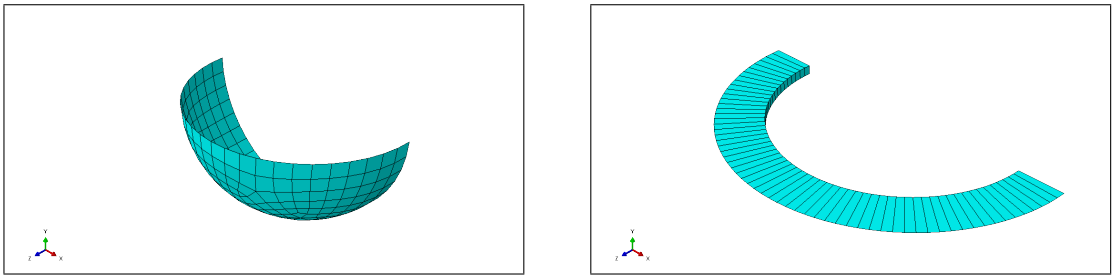

(a) *(b)*

Figure 2.13: Tool (a) and support (b)

Metal sheet is characterized by a series of partitions useful to determine different regions of interest. In particular, an external crown is defined to circumscribe the clamped zone (i.e. the area subjected to the pressure) and a central strip is delimited to confine the primary working zone (the sector entering in contact with the tool). Moreover, a central partition "cuts" the sheet in two symmetric parts and it is useful to define a path to measure the effective deformation after the machining.

Thickness of the plate has been divided into 4 elements. The external part has been meshed using the structured technique and defining an approximate distance of the nodes equal to 5 mm. The central part adopts the swept meshing technique using, also in this case, a distance among the nodes of 5 mm. Finally, the simple geometry of the central strip allows to use the structured meshing again; since a high density of elements is required, the approximate distance is set equal to 0.5 mm. A total number of 62815 nodes are created, corresponding to 49544 C3D8R elements plus 296 C3D6 (linear wedge element) used to smoothly fit the regions.

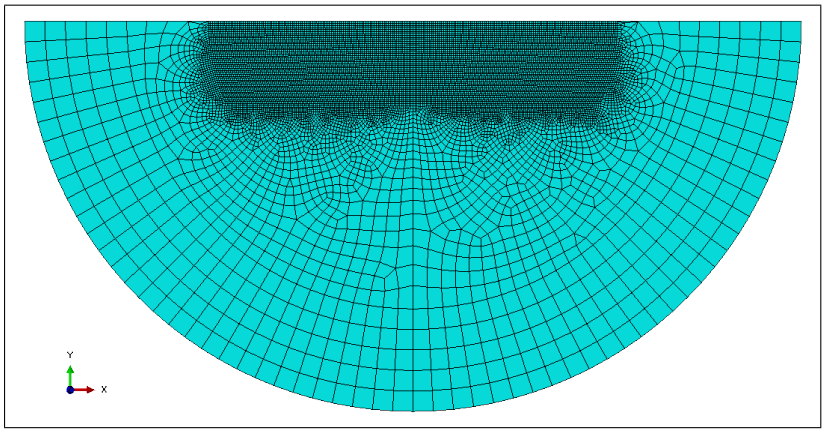

Figure 2.14: Sheet

	R3D4	R3D4	C3D8R	C3D6
Tool	8	208	-	-
Support	-	120	-	-
Sheet	-	-	49544	296

Table 2.4: Number and type of elements

2.2.2 Results of the simulation

Simulation was launched on a HP 15-da0065nl Notebook equipped with an Intel® Core™ i7-8550U; computation required about 40 hours.

In order to lighten the amount of data, evaluation of the contact forces was computed with a frequency equal to the time unit of the simulation: the result is a force matrix containing 1311 samples for each component. The only rows containing useful information are the first and the third ones, namely the force along the in-plane machining direction (from now called x-direction) and the force in the thickness direction (from now called z-direction). The second row of the matrix corresponds to the force pushing against the symmetry plane and has no physical interpretation since the model was virtually cut along that plane. The last three rows collect the moments around the three axis and they refer to the reference point representing the tool. Again, they have no physical interpretation, since the reference point is arbitrary placed and do not correspond to a real measure of the deforming machine. By the way, the configuration and the nature of the experiment allow to neglect the effect of the bending in

the compensation procedure.

Figure 2.16 and *Figure 2.17* show the trend of the forces of interest.

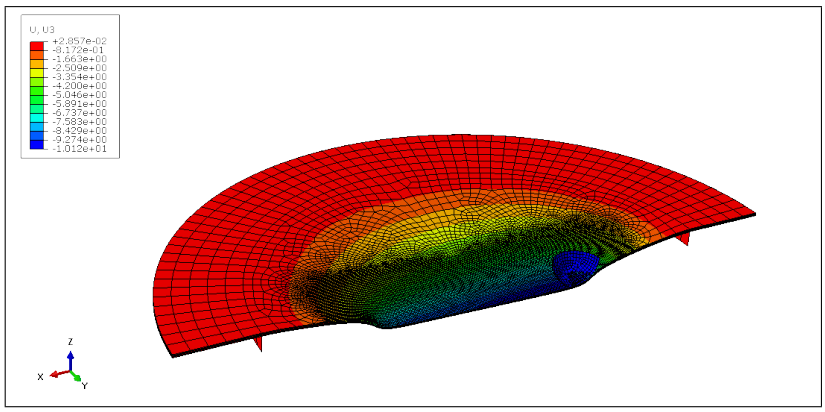

Figure 2.15: Deformed sheeet

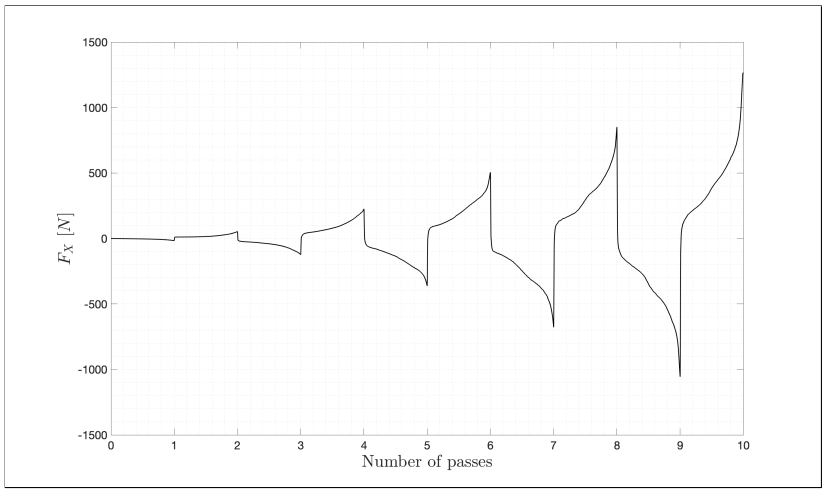

Figure 2.16: Force along in-plane machining direction

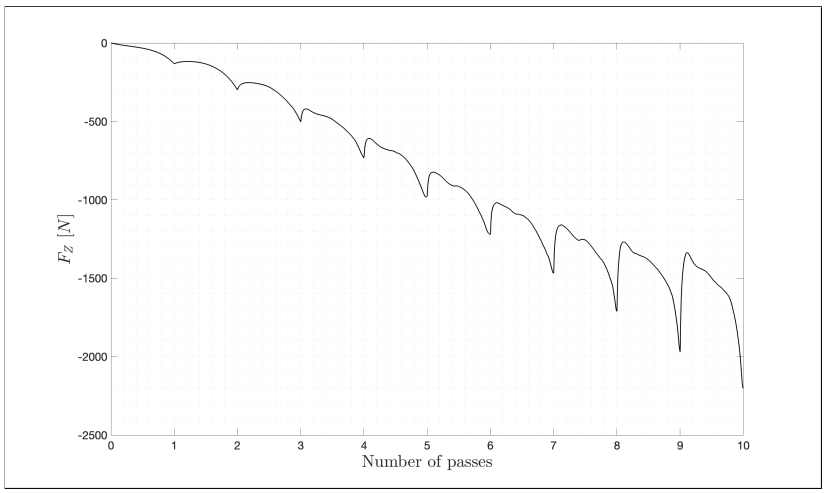

Figure 2.17: Force along thickness direction

2.3 Model validation: CNC machining

Experimental validation of the model was provided machining the part by means of a FAMUP MCX500. It is a CNC machine able to transfer a maximum force of 7000 N on the head of the tool and to reach the desired pose with an accuracy of 15 μm. The stiffness of the machine can be assumed as infinite and therefore the forces measured during the test can be approximated to the ideal values reached by the process. The data acquisition was achieved implementing an ATI Omega160 IP60 force/torque sensor, characterized by the specifications listed in *Table 2.5*. The device was directly fixed on the working bench of the CNC machine and topped by the clamping device lodging the lamina. Sampling frequency and tool feed rate were set respectively equal to 10 Hz and 2 m/min.

	x-axis	**y-axis**	**z-axis**
Force (Overload)	$\pm 18000\ N$	$\pm 18000\ N$	$\pm 48000\ N$
Torque (Overload)	$\pm 1700\ Nm$	$\pm 1700\ Nm$	$\pm 1900\ Nm$
Stiffness (Force)	$7.0 \cdot 10^7\ N/m$	$7.0 \cdot 10^7\ N/m$	$1.2 \cdot 10^8\ N/m$
Stiffness (Torque)	$3.3 \cdot 10^5\ Nm/rad$	$3.3 \cdot 10^5\ Nm/rad$	$5.2 \cdot 10^5\ Nm/rad$

Table 2.5: ATI Omega160 IP60 specifications

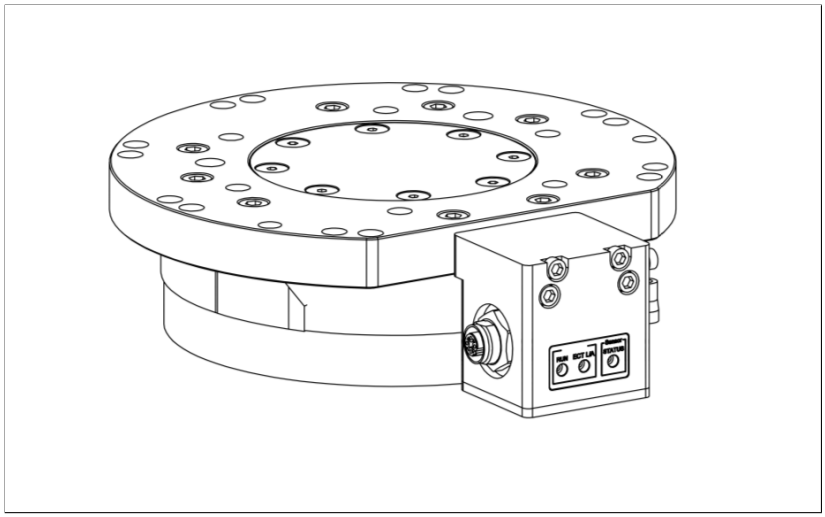

Figure 2.18: ATI Omega160 IP60 [38]

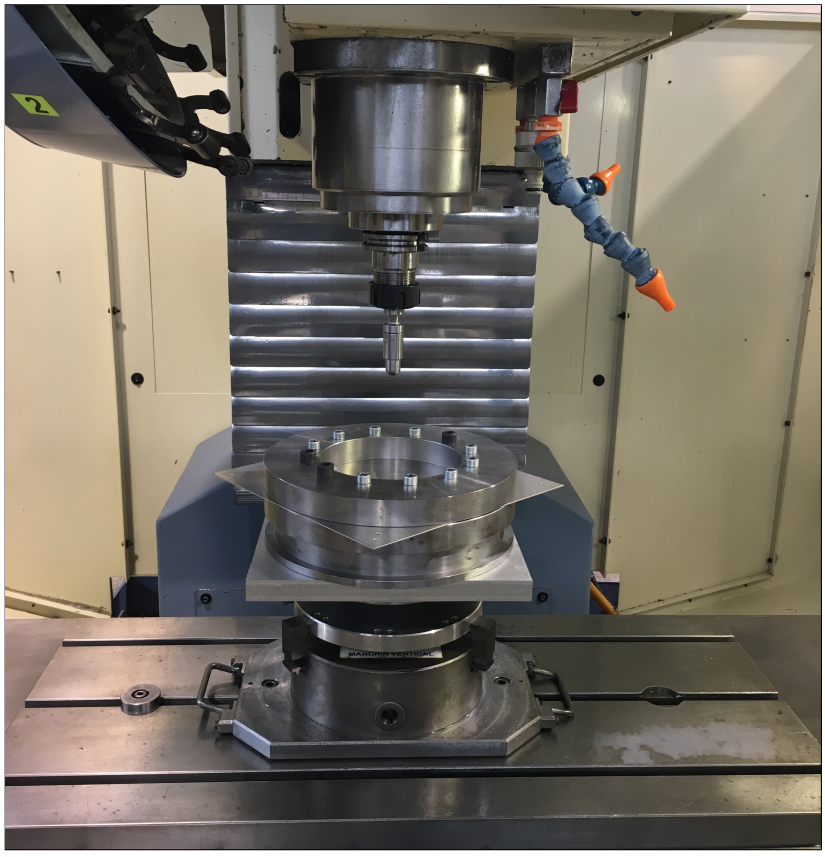

Figure 2.19: Experimental setup

2.3.1 Comparison of the results

Figure 2.20 shows the results of the CNC machining, comparing the measured forces with the predicted ones. It's worth noting how the numerical curves properly fit the

real behavior of the ISF experiment, moving away only when the tool is approaching the boundaries of the stroke. In those regions, in fact, the magnitude of the forces slightly increases and, as a consequence, the predictions become less accurate too. In particular, looking *Figure 2.21*, can be seen how the nominal error along the x-axis (referred as "*Horizontal error*" in the plot) experiences a sharp rise each time the tool inverts the direction of movement; it's due to the fact that the boundary conditions exert an higher impact on the in-plane movement direction, hampering the feed of the tool when it moves toward the blank holder. Moreover, since an inversion of movement implies the change of the sign of the horizontal force, any misalignment – although in very small size – along the abscissa represents a significant local error, which is manifested as the spikes in the plot.

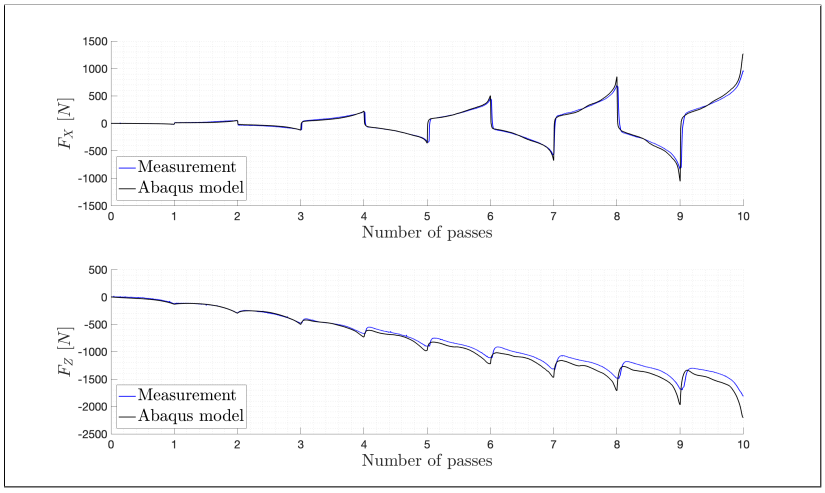

Figure 2.20: Force comparison (CNC vs ABAQUS)

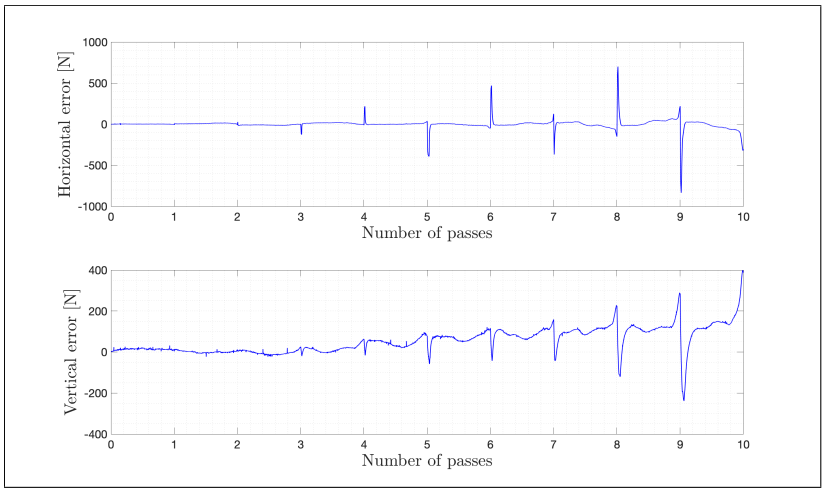

Figure 2.21: Nominal error (CNC vs ABAQUS)

The error $\mathbf{E_{CNC/AB}}$ is defined using the sampled data $\mathbf{F_{CNC}}$ as reference, following the formulation of *Equation 2.9* (where $\mathbf{F_{AB}}$ represents the matrix containing the forces coming from the ABAQUS model).

$$\mathbf{E_{CNC/AB}} = \mathbf{F_{CNC}} - \mathbf{F_{AB}} \tag{2.9}$$

Therefore, focusing the plot representing the vertical error, a positive trend implies an overestimation (in terms of absolute values) of the numerical forces with respect to the measured ones. This divergence of the data can be explained remembering the initial assumption regarding the infinite stiffness of the FAMUP MCX600. It is reasonable, in fact, that a fraction of the power provided by the engine to ensure the right positioning of the tool is, instead, absorbed by the internal deflections of the CNC machine.

Another useful tool to evaluate the reliability of the numerical simulation is the comparison of the effective deformations. *Figure 2.23* shows the profile of machined part along the central partition of the model. The numerical curve is compared with the physical result obtained by means of a 3D laser scansion of the worked lamina. The two figures follow similar trajectories and in both cases the maximum depth of the groove reaches a value close to 8.7 mm. It is well below the target of 10 mm and it is justified by the fact that, after the disengagement of the tool, the lamina relaxes and recovers its elastic deformation. It is a classical issue of the machining processes involving the plastic deformation of the components and this aspect will not be treated in this work. No measurement was provided regarding the deformed lamina before the evacuation of the tool, but this effect can be seen on the ABAQUS results (*Figure 2.24*).

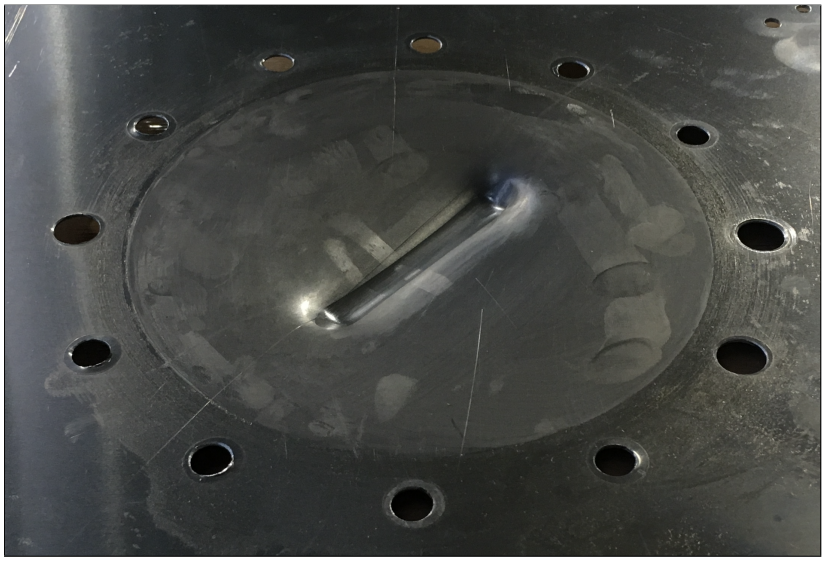

Figure 2.22: Machined part

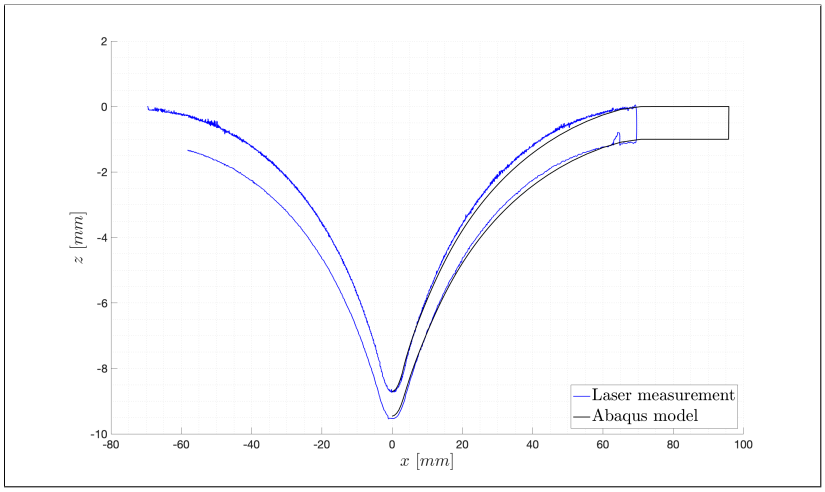

Figure 2.23: Deformation (CNC vs ABAQUS)

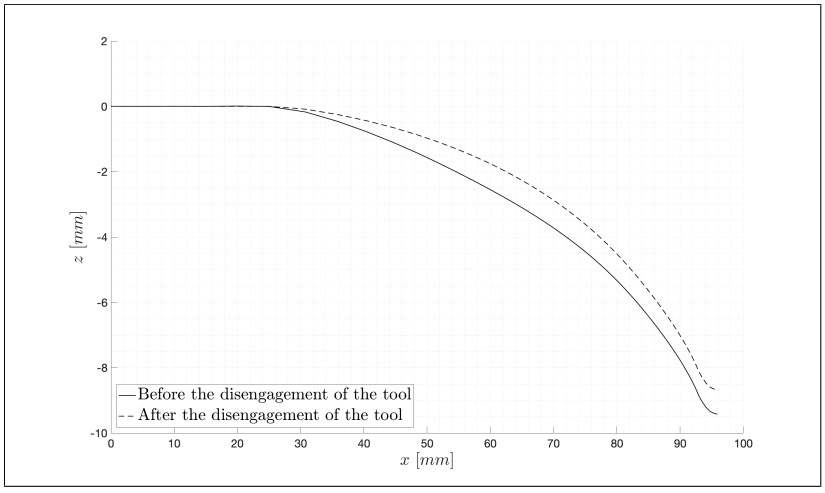

Figure 2.24: Elastic recovery of the lamina (top surface)

2.4 Influence of parameters

The model discussed so far represents the best compromise among a list of several options that was investigated during the preliminary analysis. Some parameters such as the material properties, the boundary conditions and the analysis procedure were univocally defined basing on literature, a priori evaluations and experience. Certain others, vice versa, were identified as key performance indicators and were judged sensitive to the performance of the simulation. The main parameters on which was focused the attention are essentially two: the mesh size and the friction coefficient between the tool and the sheet.

2.4.1 Mesh size

The main variable of any finite element analysis is the mesh size: regardless the nature of the case, the applied load, the boundary conditions and any other possible characteristic of the problem, mesh refinement leads to an improvement of the results. Since the definition of an element represents a discretization of the continuum, the empowerment of the element's density increases the resolution in the part and the result of the numerical approximation is a better estimation of the real field. By the way, also the cost associated to the time consumption is very sensitive to this parameter and, moreover, an asymptotic limit exists beyond which any further improvement is useless in terms of performance. A massive refinement that is not aware of the real cost-benefit ratio may even result harmful for the global performance of the analysis, increasing the computational time without improving the quality of the result.

In the model discussed in this thesis, the refinement procedure concerns the inner partition of the lamina, i.e. the string on which the tool recursively works. The approximate seed distance, as already mentioned, is 0.5 mm but it was also tested a model having a coarse mesh of 1 mm: the results concerning the vertical force were unsatisfactory, while no difference was found on the horizontal force. Since the final simulation required about 2 days of computations, any additional time consumption would not be tolerated and hence the refinement procedure was not deepen investigated. Anyway, the convergence of the numerical curve to the measured one represents a satisfactory result and no important improvements would have been obtained testing

a further refined mesh. The choice to use the force diagrams instead of the deformations to select the optimal mesh size of the lamina is due to the fact that the main attention of the analysis focuses right on the level of the forces; moreover, the comparison between 0.5 *mm* and 1 *mm* simulations reveals an imperceptible variation in terms of deformations, suggesting – erroneously – the futility of 0.5 *mm* refinement.

Also the number of the elements along the thickness was investigated, but the addition of a fifth element led to an identical result. At the same time, the implementation of less than four elements was judged improper according to the evaluations made in *Subsection 2.1.3*.

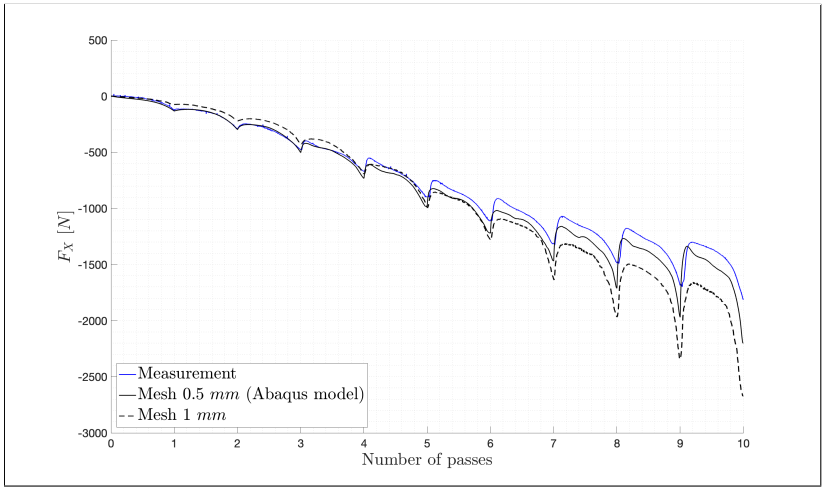

Figure 2.25: Influence of mesh refinement

2.4.2 Friction coefficient

Despite the use of lubricant, the numerical results reveal that the assumption of frictionless interaction between the lamina and the deforming tool is not very reliable. The additional substance interposed between the two surfaces cannot guarantee an ideal behavior and a possible explanation may lie in the movement of the tool. The repetitive passes, in fact, progressively reduce the effect of the lubricant and the advance of the tool results to be more difficult.

Friction contribution seems to affect only the horizontal components of the trajectory, requiring an additional effort to achieve the desired position, while the trend of the vertical force appears unchanged. Due to the surface finishes of the components, a kinetic friction coefficient equal to 0.2 is assumed for the reciprocal movement of

the two metals in absence of lubricant; thus, in case of lubricant-assisted motion, an averaged value of 0.1 was tested. The result of the simulation verified the assumption.

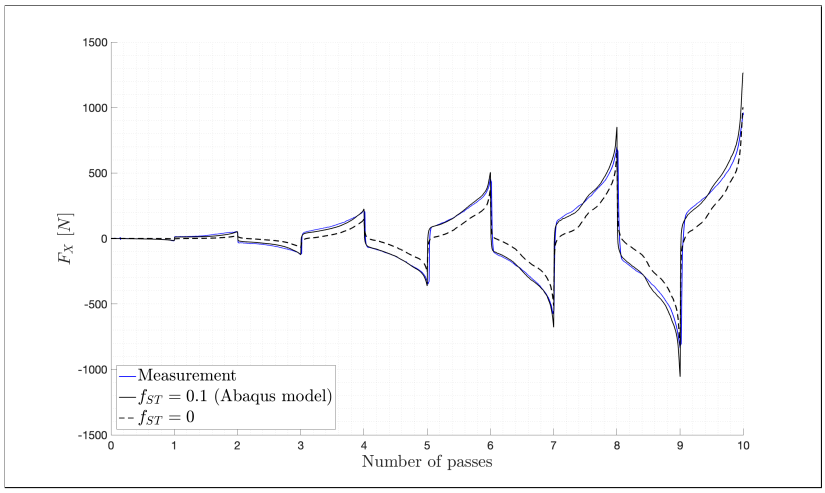

Figure 2.26: Influence of friction coefficient

Chapter 3

Staübli TX200: Nominal trajectory

3.1 Staübli TX200 characterization

Staübli TX200 is a 6-axis robot that provides a high rate of flexibility. Its configuration allows the mounting on both floor or ceiling and – thanks to the fully enclosed structure certified by IP65 classification – it ensures high performances also in harsh environment. Its design guarantees a spherical work envelope, favoring an optimum utilization of cell workspace; it is able to reach a maximum distance of 2194 mm and a maximum payload of 150 kg [39].

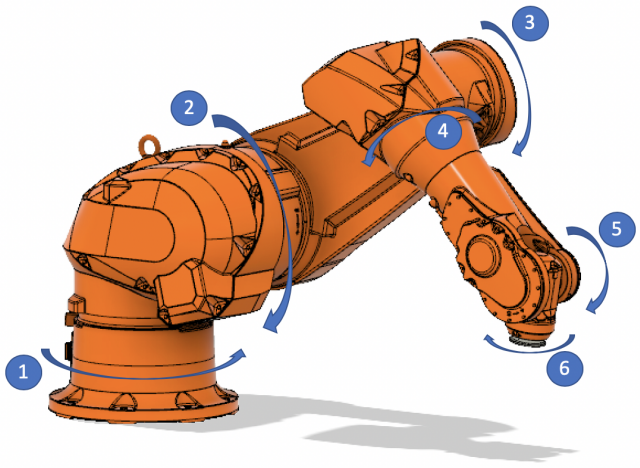

Figure 3.1: Staübli TX200

Staübli TX200	
Maximum load	150 kg
Maximum distance	2194 mm
Number of degrees of freedom	6
Repeatability - ISO 9283	± 0.06 mm
Staübli series control	CS8C HP
Weight	980 kg

Table 3.1: Characteristics of Staübli TX200 (general)

Staübli TX200 (maximum speed)	
Joint 1	$160^\circ/s$
Joint 2	$160^\circ/s$
Joint 3	$160^\circ/s$
Joint 4	$260^\circ/s$
Joint 5	$260^\circ/s$
Joint 6	$400^\circ/s$
Maximum speed at load gravity center	12 m/s
Maximum inertia joint 5	45 $kg \cdot m^2$
Maximum inertia joint 6	20 $kg \cdot m^2$
Brakes	All joints

Table 3.2: Characteristics of Staübli TX200 (velocities)

Staübli TX200 is an open-chain robot characterized by 6 revolute joints. Several models exist in order to describe the kinematics of the manipulators; they are based on different approaches (geometric, algebraic, numeric), but all rely on the same philosophy: the definition of a mathematical model able to provide the control and the position of the end effector. One of the most common method used in robotics is the homogeneous transformation matrix based on Denavit-Hartenberg (D-H) parameters [40]; it's an effective way to completely define the position and the orientation of the end effector starting from a set of four parameters per each joint.

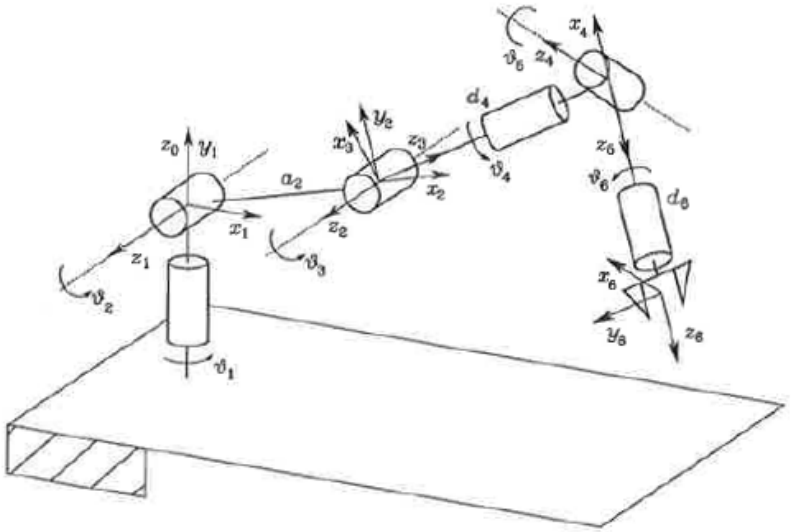

Figure 3.2: Schematic representation of 6R anthropomorphic robot

3.1.1 Homogeneous transformation matrix

Due to its peculiar shape, an anthropomorphic robot with n joints will have *n+1* links. Traditionally, the link referred to the robot base is indicated with 0 and the joint connecting link $i-1$ to link i is indicated as link i. Each joint i defines a degree of freedom of the robot and it is denoted as q_i. Each link i of the manipulator is related to a corresponding reference frame $\mathcal{F}(O_i, x_i, y_i, z_i)$ attached on it and the frame associated to the base is indicated as inertial frame.

Generally speaking, the exact location of the frame $\mathcal{F}(O_i, x_i, y_i, z_i)$ in the 3D space with respect to the reference frame $\mathcal{F}(O_{i-1}, x_{i-1}, y_{i-1}, z_{i-1})$ related to the previous link can be univocally determined by the definition of 6 parameters (3 for the position and 3 for the orientation). The common way to collect these parameters is the homogeneous transformation matrix, that's a 4×4 matrix having the form expressed in *Equation 3.1.*

$$\mathbf{A}_i = \begin{bmatrix} \mathbf{R}_i^{i-1} & \mathbf{T}_i^{i-1} \\ \mathbf{0} & 1 \end{bmatrix} \tag{3.1}$$

$\mathbf{R}_i^{i-1}$ is the 3×3 rotation matrix expressing the orientation of the frame i with

respect to the frame $i-1$ and $\mathbf{T}_i^{i-1}$ is a column vector collecting the offset along the three orthogonal directions from the origin of the frame $i-1$ to the origin of the frame i. The philosophy of the adopted nomenclature is to indicate the related frame with the subscript and to use the apex to identify the reference frame. Adopting the same approach in a cascade way, the position and the orientation of the flange (on which is connected the tool) with respect to the robot base can be defined with an iterative computation as in *Equation 3.2*.

$$\mathbf{H}_n^0 = \prod_{i=1}^{n} \mathbf{A}i(q_i) \tag{3.2}$$

The dependance of the homogeneous transformation matrices on the respective joint is clearly explained by the fact that the location of the flange is determined by the value assumed by the degrees of freedom and that the movement of a link is independent by the movement of the other links.The orientation between two generic frames i and j (with $j > i$) can be determined in a similar way (*Equation 3.3*) and the offset between their origins can be found with *Equation 3.4* [41].

$$\mathbf{R}_j^i = \prod_{k=i}^{j-1} \mathbf{R}_{k+1}^k(q_k) \tag{3.3}$$

$$\mathbf{T}_j^i = \mathbf{T}_{j-1}^i + \mathbf{R}_{j-1}^i \mathbf{T}_j^{j-1} \tag{3.4}$$

3.1.2 Denavit-Hartenberg parameters

The placement of the link's frames is completely arbitrary, but several techniques exist to make the computation easier. In particular, Denavit-Hartenberg methodology allows to reduce the number of parameters required to completely define the location of an object from six to four. These four parameters are:

- Joint angle θ_i

- Link length a_i
- Link twist α_i
- Link offset d_i

The choice of these parameters is based on the geometry of the robot and follows some particular rules. In some cases the definition of the variables is not univocal, may thus exist different D-H classifications for the same robot, but all lead to the same homogeneous transformation matrix. Since Staübli TX200 is characterized by only revolute joints, the following explanation will neglect the case of prismatic joints despite the procedure may be adapted also for the coexistence of both kind of joints.

The method starts from the allocation of the reference frame of the robot base. The z-axis lies on the rotational axis of the joint (the same will be valid also for the sequent joints) and – since no other reference frames were still defined – the choice of the x-axis is completely free; the orientation of the third axis simply follows the right-hand rule. For the sequent joints the origin is determined by the common normal of the corresponding z-axis (as before, identified by the rotational axis) and the z-axis of the previous joint; the x-axis lies along this common normal and the right-hand rule completes the definition of the frame. The distance between the origin of the new frame with respect to the previous one evaluated along the previous z-axis represents the *link offset* d_i, the distance along the common normal from the previous z-axis and the origin of the new reference frame is the *link length* a_i and the *link twist* α_i expresses the angle between the rotational axis of the two joints. The forth parameter, the *joint angle* θ_i, is the angle around the previous z-axis to align its x-axis with the new one and is related to the i^{th} degree of freedom of the robot q_i. A special case is the circumstance in which the two adjacent revolution axes are parallel; in that condition the choice of the link offset is completely free and the definition of the other parameters follow the same rules as in the normal case.

Adopting D-H methodology, *Table 3.3* is obtained for Staübli TX200.

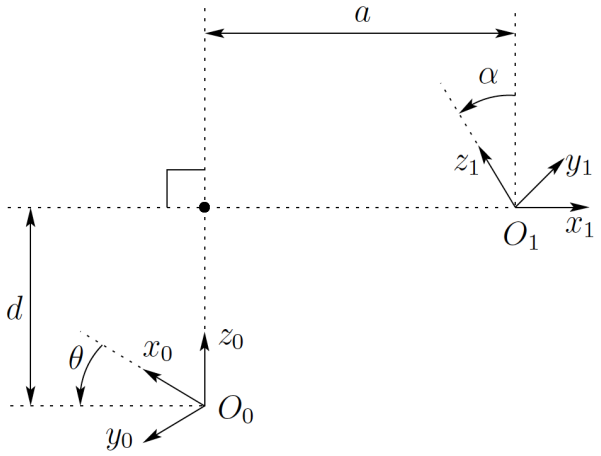

Figure 3.3: Denavit-Hartenberg procedure [41]

Joint	θ $[rad]$	d $[m]$	a $[m]$	α $[rad]$
1	θ_1	0.64	0.26	$-\pi/2$
2	$\theta_2 - \pi/2$	0	0.95	0
3	$\theta_3 - \pi/2$	0	0	$-\pi/2$
4	θ_4	0.8	0	$\pi/2$
5	θ_5	0	0	$-\pi/2$
6	$\theta_6 + \pi/2$	0.19	0	0

Table 3.3: Denavit-Hartenberg parameters for Staübli TX200

As a consequence of the above declared procedure, the homogeneous transformation matrix of a link with respect to its predecessor can be defined as follow:

$$\mathbf{A}_i = \mathbf{Rot}_{z,\theta_i}\mathbf{Trans}_{z,d_i}\mathbf{Trans}_{x,a_i}\mathbf{Rot}_{x,\alpha_i} \tag{3.5}$$

Where $\mathbf{Rot}_{z,\theta_i}$ represents the rotation matrix associated to zero rotation around the z-axis, $\mathbf{Trans}_{z,d_i}$ is the translation matrix associated to zero displacement along z-axis and the other two terms are the equivalent matrices concerning the x-axis. Expanding the terms of *Equation 3.5*:

$$\mathbf{Rot}_{z,\theta_i} = \begin{bmatrix} cos(\theta_i) & -sin(\theta_i) & 0 & 0 \\ sin(\theta_i) & cos(\theta_i) & 0 & 0 \\ 0 & 0 & 1 & 0 \\ 0 & 0 & 0 & 1 \end{bmatrix} \tag{3.6}$$

$$\mathbf{Trans}_{z,d_i} = \begin{bmatrix} 1 & 0 & 0 & 0 \\ 0 & 1 & 0 & 0 \\ 0 & 0 & 1 & d_i \\ 0 & 0 & 0 & 1 \end{bmatrix} \tag{3.7}$$

$$\mathbf{Trans}_{x,a_i} = \begin{bmatrix} 1 & 0 & 0 & a_i \\ 0 & 1 & 0 & 0 \\ 0 & 0 & 1 & 0 \\ 0 & 0 & 0 & 1 \end{bmatrix} \tag{3.8}$$

$$\mathbf{Rot}_{x,\alpha_i} = \begin{bmatrix} 1 & 0 & 0 & 0 \\ 0 & cos(\theta_i) & -sin(\theta_i) & 0 \\ 0 & sin(\theta_i) & cos(\theta_i) & 0 \\ 0 & 0 & 0 & 1 \end{bmatrix} \tag{3.9}$$

And thus:

$$\mathbf{A}_i = \begin{bmatrix} cos(\theta_i) & -sin(\theta_i) \cdot cos(\alpha_i) & sin(\theta_i) \cdot sin(\alpha_i) & a_i \cdot cos(\theta_i) \\ sin(\theta_i) & cos(\theta_i) \cdot cos(\alpha_i) & -cos(\theta_i) \cdot sin(\alpha_i) & a_i \cdot sin(\theta_i) \\ 0 & sin(\alpha_i) & cos(\alpha_i) & d_i \\ 0 & 0 & 0 & 1 \end{bmatrix} \tag{3.10}$$

Recalling *Equation 3.2*, the position and orientation of the flange with respect the robot base can be thus defined and, knowing the geometrical properties of the tool, the previous relationship can be simply shifted from the flange to the end effector.

3.1.3 Jacobian matrix

The procedure showed in the previous sections is known in literature as forward kinematics and represents a useful mathematical model to describe the position of the end effector as function of robot joints. Switching to velocity domain, the analysis refers to the so-called differential kinematics and it allows to introduce a very powerful tool called Jacobian ($\mathbf{J}$). It formally represents the dynamic relationship between the velocity of the end effector $\boldsymbol{\zeta}$ and the velocity of the joints $\dot{\mathbf{q}}$ and it appears in the form of a matrix having dimensions $6 \times n$:

$$\boldsymbol{\zeta} = \mathbf{J}(\mathbf{q}) \cdot \dot{\mathbf{q}} \tag{3.11}$$

The number of the rows is related to the six components of the velocity of the end effector, while the number of columns refers to the number of joints of the robot. Thus, the Jacobian can be split into two submatrices according to linear and angular velocities:

$$\mathbf{J}(\mathbf{q}) = \begin{bmatrix} \mathbf{J}_v \\ \mathbf{J}_\omega \end{bmatrix} \tag{3.12}$$

Thanks to the fact that in the D-H convention the rotation of the joints always arises around the z-axis, recalling *Equation 3.1* can be shown that the i-th column of the upper and bottom parts of the Jacobian can be respectively expressed as in *Equation 3.13* and *Equation 3.14*.

$$\mathbf{J}_{v_i} = \mathbf{R}^0_{i-1} \cdot \begin{bmatrix} 0 \\ 0 \\ 1 \end{bmatrix} \times \left(\mathbf{T}^0_{EE} - \mathbf{T}^0_{i-1} \right) \tag{3.13}$$

$$\mathbf{J}_{\omega_i} = \mathbf{R}^0_{i-1} \cdot \begin{bmatrix} 0 \\ 0 \\ 1 \end{bmatrix} \tag{3.14}$$

The subscript EE indicates the frame of the end effector; the tool is considered attached to the flange of the robot and is treated as an additional link placed in series with the robot ones. $\mathbf{T}^0_{EE}$ is thus simply derived adding the length of the tool L_T to the translation vector linking the flange to the robot base.

$$\mathbf{T}^0_{EE} = \mathbf{T}^0_n + \begin{bmatrix} 0 \\ 0 \\ L_T \end{bmatrix} \tag{3.15}$$

The numerical result of the Jacobian and the code used to evaluate it can be found in *Appendix B*.

3.1.4 Robot singularities

The Jacobian was defined as the matrix which relates changes in joint velocities to end effector velocities. Since the movement of a robot is mapped out in Cartesian space but carried out in joint space, the study of the domain of the Jacobian (and its inverse) is very useful to provide a correct control of the robot. May exist some configurations

that lead to a difficult – or even unfeasible – movement of the manipulator; these events are represented by all the joint combinations that nullify the determinant. Indeed, the determinant equal to zero represents the conditions in which the Jacobian is not invertible and its rank is not maximum, making some components of the end effector velocity not controllable by the joint domain. Such points are called *singularities* and rely to two possible cases:

- **Workspace singularity (or boundary singularity)**: it is due to the maximum extension of a link, asking the robot to reach a position outside its workspace.
- **Joint space singularity (or internal singularity)**: it is caused by the alignment of two axis and leads to infinite possible solutions of the inverse kinematic or the need of an infinite joint velocity.

The determinant of Staübli TX200 is:

$$\begin{aligned} det(\mathbf{J}) = & -\frac{19}{2500} \cdot sin(q_5) \cdot [\ 80 \cdot cos(q_2) + 26 \cdot sin(q_3) + \\ & + 95 \cdot sin(q_2) \cdot sin(q_3) - 80 \cdot cos(q_2) \cdot cos(q_3)^2 + \\ & + 80 \cdot cos(q_3) \cdot sin(q_2) \cdot sin(q_3)\ ] \end{aligned} \tag{3.16}$$

The study of the values that bring to a null determinant immediately leads to the solution $q_5 = 0 + k \cdot \pi$ with $k \in \mathbb{N}$. It corresponds to the alignment of the flange axis (joint 6) with the forearm axis (joint 4); in this case the robot is not able to choose how to perform a rotation around the common axis since several options exist. Another intuitive solution is the case $q_3 = 0 + k \cdot \pi$: in this configuration the robot reaches its maximum extension aligning the links 2 and 4.

All the other possible singularities can be found imposing *Equation 3.16* equal to zero; solving it numerically, the following mapping is obtained.

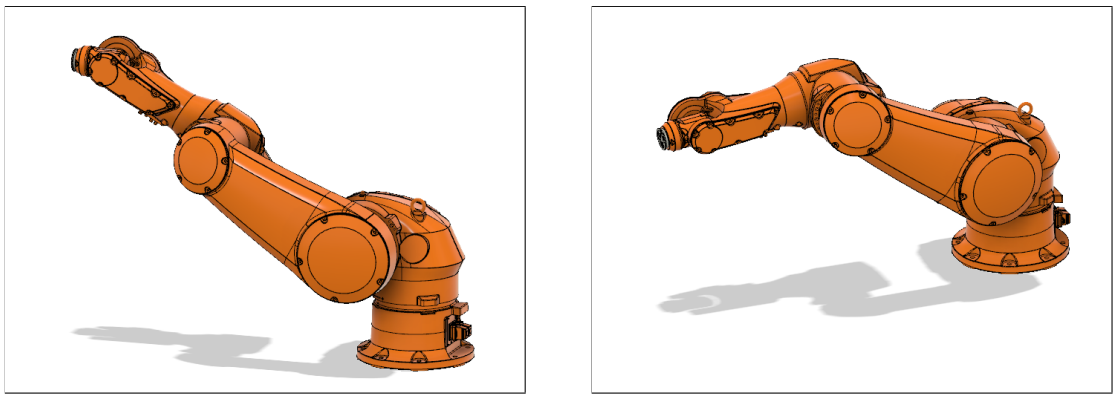

(a) *(b)*

Figure 3.4: Workspace singularity with $q_3 = 0$ (a) and internal singularity with $q_5 = 0$ (b)

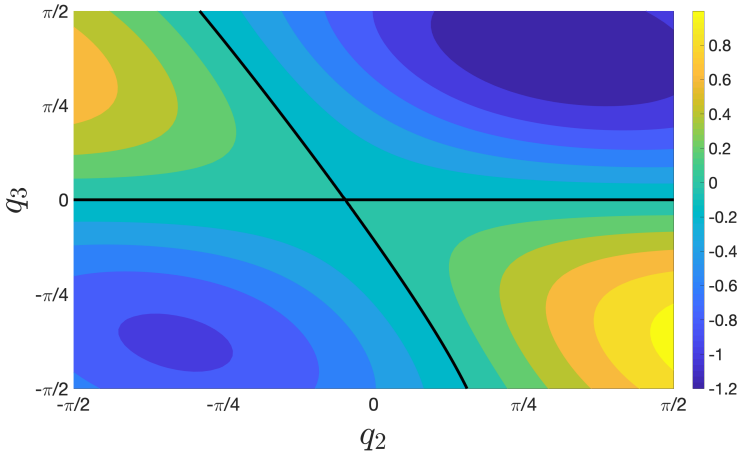

Figure 3.5: Singularity domain ($q_2 - q_3$ plane)

3.2 Post processor: RoboDK

Till now the analysis neglected the presence of the robot and only focused on the trend of the forces based on a simulation software and the subsequent experimental validation by means of a CNC machine. In order to implement the trajectory on the anthropomorphic device an additional digital tool is needed to convert the current information in the robot language: the tool used for this purpose is RoboDK.

RoboDK is a powerful software for offline programming and simulation of industrial machining; it includes in its library more than 300 robots from more than 30 different manufacturers and is compatible with all the main operating systems on the market. The software is able to manage all the tasks needed for this stage of the experiment:

the reconstruction of the experimental environment, the simulation of the test and the generation of the code in robot native language.

3.2.1 Experimental setup

To have a digital representation of the working station, the position of all the components was accurately measured through a Krypton K-610 CMM. It is a coordinate-measuring machine able to measure the location of a single point, by means of an infrared hand-held space probe, with an accuracy of 40 μm within a volume of 17 m^3. The accuracy is guaranteed in a temperature range between 15°C and 40°C and the resolution is 2 μm up to a distance of 2.5 m from the measuring system.

In alternative, it can triangulate the position of the target point with a variable accuracy according to the distance from the source. Detailed information about this kind of functioning are collected in the following table.

Distance	**Accuracy**	**Uncertainty**
$x \leq 3\ m$	60 μm	+10 μm
$3\ m < x \leq 5\ m$	70 μm	+25 μm
$5\ m < x \leq 6\ m$	140 μm	+25 μm

Table 3.4: Characteristics of K-610 CMM for volumetric application

The indicated measurement uncertainty is expressed for a confidence level of 95%, according to the ISO 10360 II, VDI 2617 and ANSI / ASME B89.1.12M standards for acceptance of CMMs [42].

To measure the length of the tool, a redundant set of measurements was taken; the tool, attached to the robot, was put in contact with a known point and the flange was moved in four different positions maintaining the contact point between the end effector and the reference. The extracted measurements (identified by the poses of the robot) were implemented in a simple MATLAB code to build the sphere best fitting the 4 measurements of the flange: the radius of that sphere can be assumed as the length of the tool ($L_T = 274.94\ mm$).

The metal sheet with its clamping system was fixed on a rigid support properly balanced to be symmetric to the floor of the laboratory and then, with an approach

similar to the one used for the tool, the centre of the lamina was identified. This point will be used as origin of the reference frame of the trajectory.

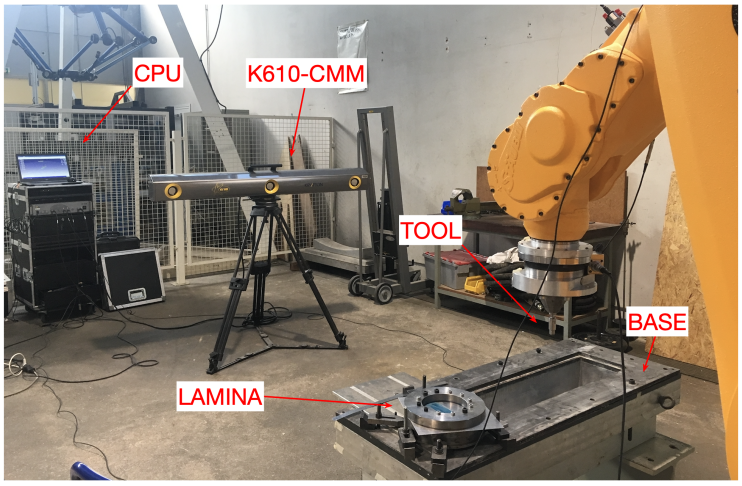

Figure 3.6: Experimental environment

3.2.2 Nominal trajectory

The definition of the trajectory must guarantee the feasibility of the process. The inverse kinematics has to be solved avoiding singularities during the whole machining and the velocity of the tool may be ranged to prevent the saturation of the actuators. In the case under analysis, singularities may be simply bypassed since the working area is small and only a limited number of joints are involved in the action. The minimum number of points needed to correctly reconstruct the trajectory is eleven (one at each change of direction), but in this way the span between two consecutive points becomes not negligible. Along the path, indeed, the tool has to deform the metal sheet and a higher number of points may simplify its advancement and make it more linear. Moreover, the aim of the test is to obtain a nominal trajectory and then to compensate it with a coefficient (i.e. the term related to the compliance of the robot in that particular configuration) to achieve the right shape in the lamina; higher the point density along the path, higher will be the accuracy of the compensation. On the other end, despite the robot speed was properly defined equal to 33.33 mm/s, the simulation shown a decrease of the speed with the increase of the points' density and this trend was then confirmed also in the real experiment. It may be explained with

the saturation of the actuators that are not able to reach the required speed between one point and the next one; by the way, as already mentioned, the low level of speed involved in ISF classifies the process as quasi-static and thus a further slowdown due to mechanical issues does not affect the result of the machining.

3.2.3 Generation of G-code

The trajectory is stored in a text file and read by a Pyhton code that communicates with RoboDK and commutes input data in a list of robot poses. The software is able to carry out the simulation of the machining using the information sent by Python and can generate the corresponding G-code that is then implemented in the robot controller to move Staübli TX200.

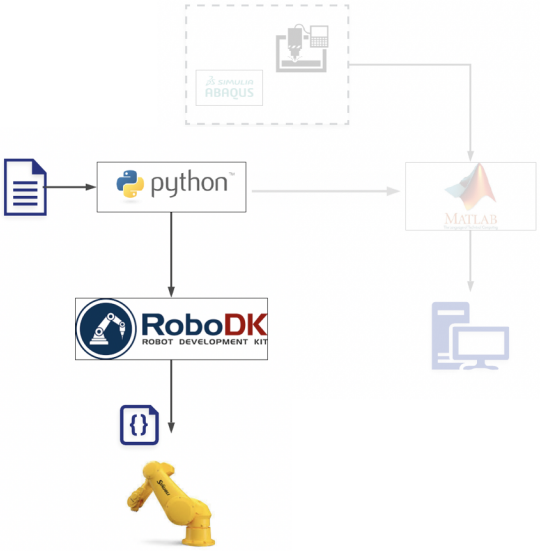

Figure 3.7: From trajectory to G-code

The orientation of the trajectory with respect to the robot reference frame is not trivial, since it defines how the robot will move and which joints will be involved during the process. The frame of the tool is selected as reference for the trajectory and is aligned exactly as the frame of the robot base. Two main options may be selected; the first one is the simultaneous rotation of joint 2 and joint 3, providing a linear motion along the x-axis of the tool (red line in *Figure 3.8*) or, in alternative, the concurrent rotation of joint 1 and joint 3 to obtain a straight line following the y-axis of the tool (green line in *Figure 3.8*). In both cases the longitudinal axis of the tool remain orthogonal to the metal sheet during the whole machining. Due to the geometry of

the robot, is reasonable to assume that the joint 1 is stiffer with respect joint 2; by the way, for simplicity in operations – and to emphasize the compliant effect – the first option was selected.

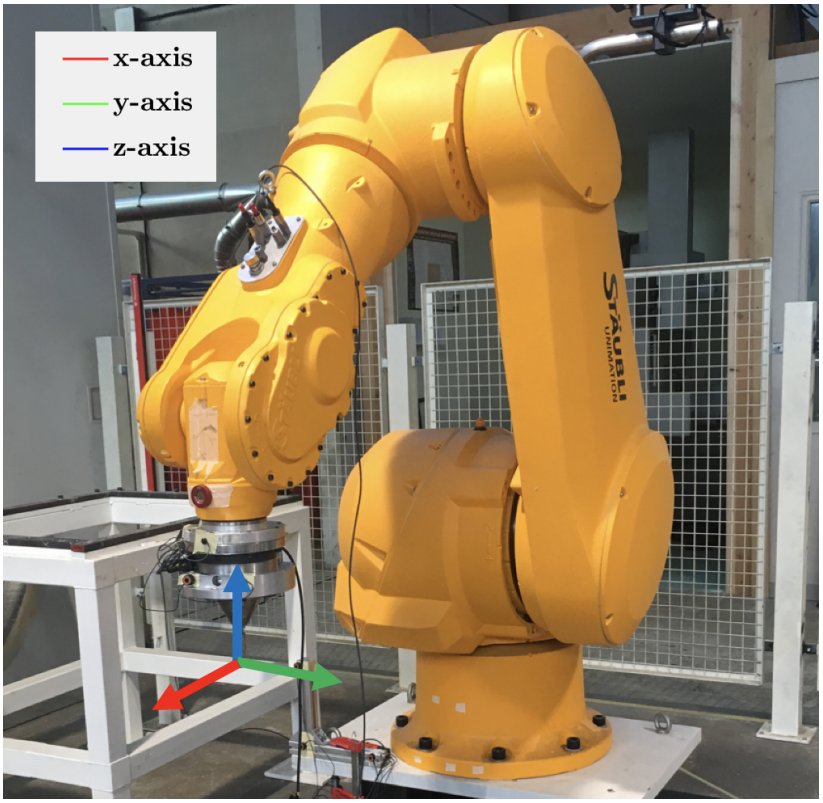

Figure 3.8: Reference frame of the tool

3.3 Experimental test

Krypton K-610 CMM is used to track the movement of the end effector and the same force sensor already used for CNC test is implemented to store the information regarding the forces exchanged with the metal sheet. The sampling frequency of CMM is set equal to 50 Hz, while the forces are measured with a frequency of 30 Hz. The discrepancy between the two different frequencies is not a problem since the two set of data have not to be compared between them: displacements will be confronted with the ABAQUS simulation to provide an index of the inner deflection of the robot, while the forces coming from the experiment will be used to provide an additional prove of the effectiveness of the methodology. Indeed, once the stiffness matrix will be evaluated, its contribution is expected to balance also the misalignment between the

ideal forces and the forces measured during the nominal test.

3.3.1 Results

Figure 3.9 shows the movement of the tool during a *trial* machining performed without the interaction with the lamina and it is compared with the ideal trajectory numerically computed.

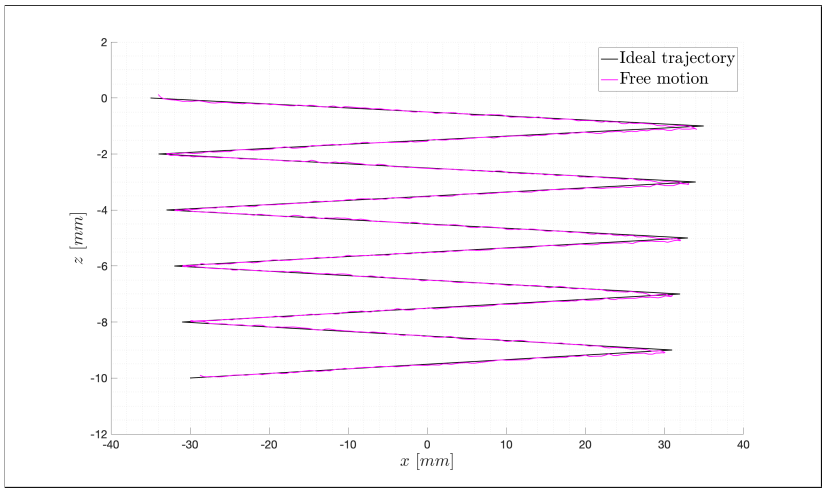

Figure 3.9: "Free" motion of the tool with respect to the ideal trajectory

The robot is ideally able to reproduce the trajectory with a high degree of accuracy, but the real application would show a strong worsening of the results due to the compliance of the joints and the springback effect. The real path defined by the robot can be observed in *Figure 3.10* and the corresponding forming forces are reported in *Figure 3.11*.

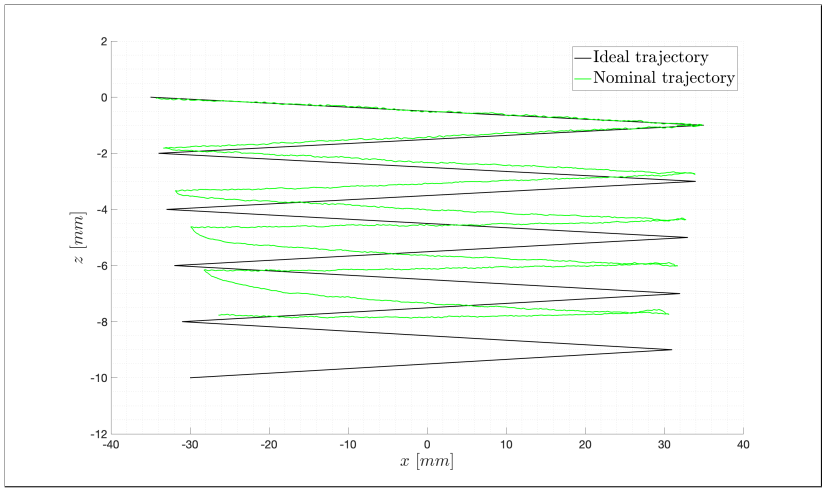

Figure 3.10: Nominal trajectory

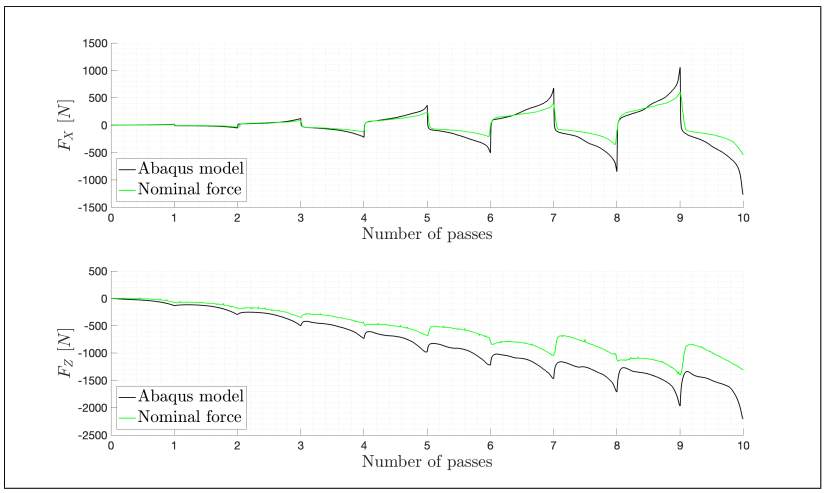

Figure 3.11: Nominal forces

The force sensor is placed between the flange of the robot and the tool; a fraction of the load is absorbed by the gears of the robot and the useful force transmitted to the end effector is less than the ideal one. The result is a geometrical distortion of the final shape, with a visible error on both x and z axis.

Despite the process appears as a quasi-symmetric machining, the test reveals a strong asymmetry in the movement of the tool. When the joints' actuators invert the rotation to switch from backward to forward travel direction, a visible distortion appears in the first part of the stroke (left side of *Figure 3.10*). This may not be explained by the interaction between the tool and the metal sheet, since their behavior should be exactly the same in both direction. Vice versa, it can be explained by the fact that the robot structure is not symmetric and the global movement of the links is different according with the direction of motion. The result is a stiffer robot when the actuators push the tool from left to right and a compliant attitude when the tool is backed out from right to left.

Chapter 4

Compensation algorithm

4.1 The compliance problem

As already mentioned, the bad result of the test presented in *Chapter 3* is mainly due to two different aspects: springback effect and robot compliance. While the first one is attributable to the nature of the technology and to the material characteristics, the latter is completely related to the robot side. The goal of this chapter is to deal with this issue and exploit a methodology to counteract its influence in the final result.

The power transmission is provided by the joints of Staübli TX200, which carry the movement of the links by means of a series of mechanical elements such as gears, pins and bearings. The assembly of all these components generates a set of deformable structures that contribute to the global compliance of the robot.

4.1.1 The mechanics of revolute joint

A revolute joint, also called pin joint or pivot, is generally composed by a pin passing through two links. The movement of the mechanism is provided by an actuator that can be electric, pneumatic or hydraulic. As a matter of fact, almost the totality of the commercialized robots works with electric actuators and, more in detail, with brushless motors. Brushless motors allow longer life with respect to other kinds of actuator, they are more expensive and need a complex electronics but they can ensure high torque transmission and high speed rates. The electric part is coupled with the mechanical part, composed by the gearbox and the effective mechanism that ensures the movement of the robot links.

Gearbox is the element needed to improve the torque transmitted to the load at the expense of the speed; its design – characterized by gears and backlashes – strongly contributes to final stiffness of the robot. The pin, splined on roller bearings, is housed in a case, connects the two links and is too composed by compliances such as the clearances among the components.

Staübli International AG produces their revolute joints on the basis of an in-house patent [43] ensuring a compact design and a theoretical zero clearance. *Figure 4.1* shows the technical drawing of the case of the joint: a screw (20c) is lodged within a bearing (20) and connects the extremity of a link (9) with the extremity of the adjacent movable link (10). The motion is provided by the rotation of a toothed cam (13).

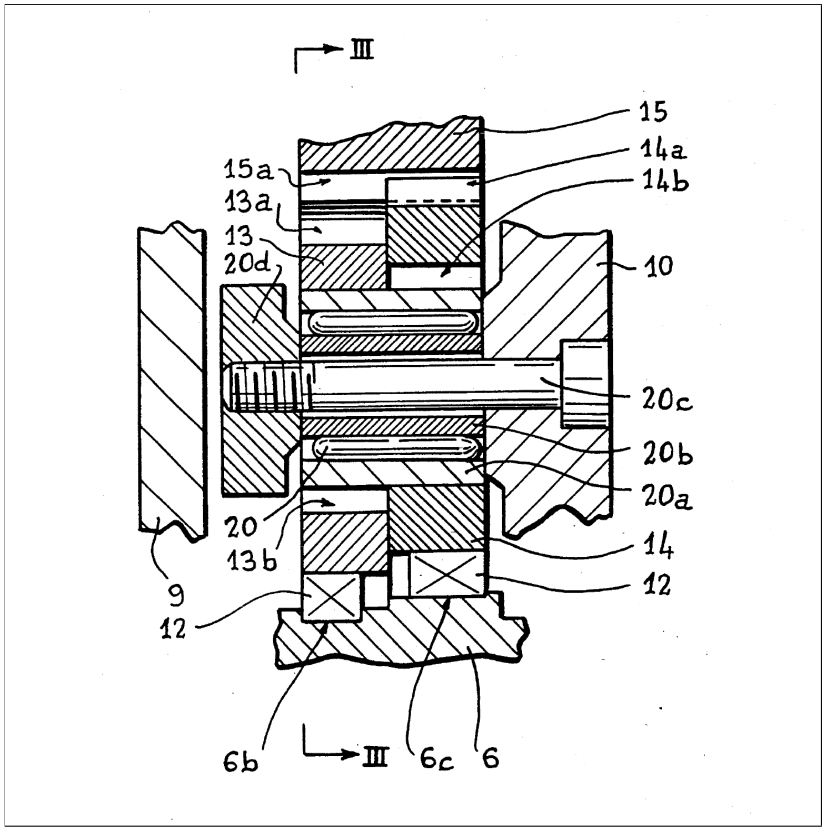

Figure 4.1: Speed reducer of the cycloidal type for robot (Patent number 5,312,305 [43])

Despite the compactness of the design the intrinsic stiffness of the materials and the unavoidable backlash generate a deflection of the joint when a load is transmitted. The purpose will be now to quantify that deflection.

4.1.2 Joint stiffness identification

Since the historical role of robots in industry is strictly related to compliant applications, robot manufacturers never focused on the study of joints' stiffness and their values are usually missing in the technical data sheets. Either literature shows a lack of references regarding this topic, but a recent study carried out by Claire Dumas et al. [44] proposes an innovative procedure to deal with this issue.

The relation between the torques $\mathbf{\Gamma}$ acting on the joints and the forces and moments transmitted to the end effector $\mathbf{f}_{ee}$ is ruled by the Jacobian following *Equation 4.1.*

$$\mathbf{\Gamma} = \mathbf{J}^T \cdot \mathbf{f}_{ee} \tag{4.1}$$

Likewise, $\mathbf{\Gamma}$ can be expressed as function of the stiffnesses of the joints.

$$\mathbf{\Gamma} = \mathbf{K_q} \cdot \delta\mathbf{q} \tag{4.2}$$

Where $\delta\mathbf{q}$ represents the infinitesimal variations of the rotations of the joints $\mathbf{q}$. Differentiating *Equation 4.1* with respect to the degrees of freedom and applying the chain rule:

$$\frac{\partial \mathbf{\Gamma}}{\partial \mathbf{q}} = \frac{\partial \mathbf{J}^T}{\partial \mathbf{q}} \cdot \mathbf{f}_{ee} + \mathbf{J}^T \cdot \frac{\partial \mathbf{f}_{ee}}{\partial \mathbf{d}} \frac{\partial \mathbf{d}}{\partial \mathbf{q}} \tag{4.3}$$

Where $\mathbf{d}$ is the displacement of the end effector. Recalling *Equation 3.11*, the latter equation can be rewritten as follow.

$$\mathbf{K_q} = \mathbf{K}_C + \mathbf{J}^T \cdot \mathbf{K}_R \cdot \mathbf{J} \tag{4.4}$$

$\mathbf{K_q}$ represents the joints' stiffness matrix; is defined as the derivative of the torques applied to the joints with respect to the joints rotation, is a 6×6 squared matrix and – since the joints are independently controlled – is diagonal. Each terms of the diagonal

represents the stiffness of the corresponding joint. $\mathbf{K}_C$ is the complementary stiffness matrix and each column is represented by the differentiation of the transposed Jacobian with respect to one degree of freedom of the robot and multiplied by $\mathbf{f}_{ee}$. Finally, $\mathbf{K}_R$ represents the global stiffness matrix of the robot and links the displacement of the end effector to the forces and moments applied on it. Considering that the displacements of the links are small according to the given wrench applied to the end effector, the first term of the right side of the latter equation can be neglected, leading to the following formulation.

$$\mathbf{K_q} \simeq \mathbf{J}^T \cdot \mathbf{K}_R \cdot \mathbf{J} \tag{4.5}$$

4.1.3 The symmetry of robot stiffness matrix

Considering a generic volume subjected to a discrete number of external forces inducing a matching number of displacements, the potential energy of the body is given by the sum of the internal deformation energy and a contribution due to the position of the external load.

The internal energy is function of the strains of the structure and, by means of the kinematic relations, can be expressed as expression of the displacements u_i. For a discrete number of forces applied to the body, the associated external energy is equal to the sum of the forces multiplying the corresponding displacements; since the forces are reaction forces, a negative sign precedes the sum.

$$E_{pot} = E_s(u_1, u_2, \cdots, u_n) - \sum_{i=1}^{n} F_i \cdot u_i \tag{4.6}$$

Potential energy has to be stationary with respect to variations of each of the displacements:

$$\delta E_{pot} = \sum_{i=1}^{n} \left(\frac{\partial E_s}{\partial u_i} - F_i \right) \cdot \delta u_i = 0 \tag{4.7}$$

From *Equation 4.7* the first theorem of Castigliano can be derived:

$$F_i = \frac{\partial E_s}{\partial u_i} \tag{4.8}$$

In a specular way, if the system is supported so that rigid movements are prevented, a complementary energy can be defined as sum of a internal volume part depending on the stresses experienced by the body and an external surface component derived as the sum of the single displacements multiplied by the corresponding forces. From the equilibrium equations a relation between stresses and forces can be established and the internal volume contribution can be redefined as function of the forces acting on the system:

$$E_{comp} = E_c(F_1, F_2, \cdots, F_n) - \sum_{i=1}^{n} u_i \cdot F_i \tag{4.9}$$

Since the complementary energy has to be stationary with respect to the variations of each of the displacements, the second theorem of Castigliano is found (*Equation 4.11*).

$$\delta E_{comp} = \sum_{i=1}^{n} \left(\frac{\partial E_c}{\partial F_i} - u_i \right) \cdot \delta u_i = 0 \tag{4.10}$$

$$u_i = \frac{\partial E_c}{\partial F_i} \tag{4.11}$$

For linear elastic materials and neglecting non-linear geometric effects, internal energy E_s and the volume part of the complementary energy E_c are equivalent and strong simplifications can be made. Adopting the superposition effect, generic forces

F_i and F_j can be written as a linear combination of the displacements:

$$F_i = \sum_{k=1}^{n} k_{ik} \cdot u_k \tag{4.12a}$$

$$F_j = \sum_{k=1}^{n} k_{jk} \cdot u_k \tag{4.12b}$$

Vice versa, also two generic displacements u_i and u_j can be expressed as linear combination of the forces applied to the system:

$$u_i = \sum_{k=1}^{n} c_{ik} \cdot F_k \tag{4.13a}$$

$$u_j = \sum_{k=1}^{n} c_{jk} \cdot F_k \tag{4.13b}$$

From *Equation 4.12* the generic stiffness coefficient k_{ij} can be derived by differentiating the force F_i with respect to the displacement u_j, obtaining the expression reported in *Equation 4.14*.

$$k_{ij} = \frac{\partial F_i}{\partial u_j} \tag{4.14}$$

Finally, substituting the first theorem of Castigliano:

$$k_{ij} = \frac{\partial^2 E_s}{\partial u_i \partial u_j} = k_{ji} \tag{4.15}$$

Collecting all the stiffness parameters in a generic stiffness matrix, a symmetric matrix is thus obtained; an analog result can be obtained considering the compliance coefficient c_{ij} and the second theorem of Castigliano. This procedure is known as *Maxwell-Betti principle of reciprocity* and informally states that the work done by one

load through the displacement due to a second load is equal to the work done by the second load through the displacement due to the first load.

The above principle is coherent with the result obtained in *Equation 4.5*; indeed, inverting the expression, the robot stiffness matrix results to be symmetric. By the way, it must be noted that the symmetric property is obtained by the assumption of absence of non-linear geometric effects.

As a first approximation, the stiffness of the joints should be found by a set of experimental tests. Then, evaluating the Jacobian in correspondence of the robot configuration at the beginning of the machining, the robot stiffness matrix can be found. Moreover, as additional assumption, the machining should be considered restricted to a working space in which the Jacobian fluctuations are negligible.

Anyway, the hypothesis of linear geometric effects is too strong to be reliable in a robot assisted Incremental Sheet Forming application and, in the specific case, the results of the experiment of *Chapter 3* already revealed the non-linear dynamic of the machining. Thus, another approach based on an experimental evaluation of the stiffness matrix will be proposed.

4.2 Identification of Staübli TX200 stiffness matrix

In this section two different experimental procedures will be shown with the common goal of the definition of the Staübli TX200 stiffness matrix. The first method concerns a redundant set of measurements of the robot deflection when it's subjected to different loading conditions; the second is based on the comparison of the input and output trajectories of the end effector during the nominal test.

The strength points of the first methodology are the cost-effectiveness and the simple procedure; on the other hand, it requires a high number of tests to be statistically significant and the setup time is high. Opposite considerations are valid for the second procedure: it manages a huge amount of data, the test is tailored for the specific application ensuring a high correlation between the preparation test and the real experiment and it allows a fast estimation of the stiffness matrix since the same setup can be used for both the machining. On the contrary, the additional machining test induces a cost that may be relevant (metal sheet, tool consumption, electric power).

It must be noted that both procedures are strictly related to the robot configuration and have local validity. If the machining leads to slight changes in the orientation of the links, the path would be discretized in regions for which the robot stiffness can be assumed constant and for each of these zones a different stiffness matrix would be computed.

4.2.1 Method 1

The complete stiffness matrix $\mathbf{K}_R$ is a 6×6 matrix linking deformations and rotations in the 3D space to the forces and moments applied to the robot in three orthogonal directions. The machining of the straight groove analyzed in this work, as already seen, does not exert any relevant torque on the end effector; the study of the stiffness matrix can be thus restricted to the tension part only, completely ignoring the torsion coefficients since they are not involved in the process.

Five tests were performed using different loading conditions. The flange of the robot was pulled by a system of weights and cables aimed at generating forces on each of the three orthogonal direction of the reference frame. Staübli TX200 has been placed in a configuration coherent with the pose used for both the nominal and compensated tests, it was then locked, loaded and the deflections were measured by the same measurement system already introduced in *Chapter 3*.

	q_1	q_2	q_3	q_4	q_5	q_6
degrees	-0.08	38.03	90.62	-0.33	51.72	-7.91

Table 4.1: Configuration of Staübli TX200 for the test

	F_x	F_y	F_z
$\mathbf{F}_1$	800 N	800 N	1500 N
$\mathbf{F}_2$	500 N	500 N	1000 N
$\mathbf{F}_3$	1500 N	800 N	800 N
$\mathbf{F}_4$	800 N	1500 N	800 N
$\mathbf{F}_5$	1000 N	1000 N	1000 N

Table 4.2: Set of loading conditions

$$\mathbf{F}_i = \begin{bmatrix} k_{xx} & k_{xy} & k_{xz} \\ k_{yx} & k_{yy} & k_{yz} \\ k_{zx} & k_{zy} & k_{zz} \end{bmatrix} \cdot \mathbf{\Delta U}_i \tag{4.16}$$

For each set of measurement, the relation expressed by *Equation 4.16* relates the inputs $\mathbf{F}_i$ to the measured output $\mathbf{\Delta U}_i$. Through an optimization procedure, the aggregate data gives an estimation of the global stiffness matrix $\mathbf{K}_{R(1)}$.

$$\mathbf{K}_{R(1)} = \begin{bmatrix} 716.50 & -949.00 & -135.00 \\ 320.50 & 378.00 & -91.00 \\ -552.00 & 1130.00 & 1080.00 \end{bmatrix} \tag{4.17}$$

Where the above data are expressed in N/mm.

4.2.2 Method 2

The second method follows a similar philosophy, but it manages a different set of data. It takes as input the forces coming from the ABAQUS model and it correlates them with the difference between the ideal trajectory and the measured positions of the end effector during the whole nominal test.

The length of the two inputs are different, since the tracking of the tool is performed with a high sampling rate while ABAQUS simulation stored the value of the forces each millimeter of the tool progress to limit the computational effort. This issue introduces the need of an interpolation to obtain comparable data. Moreover, the information coming from the test (both the simulation and the real experiment) are restricted to only two directions: this method is not able to provide a complete observability of the system and the resulting stiffness matrix will account only x-direction and z-direction.

Information coming from ABAQUS simulation are stored in a $2 \times n$ matrix $\mathbf{F_{ID}}$, where n represents the points of the interpolation and each row contains the force history along one direction (the same matrix already introduced in *Chapter 2* but

with a different discretization). The results of the experimental validation performed on the CNC certify $\mathbf{F_{ID}}$ as a good estimator of the force acting on the metal sheet during the ideal machining.

$$\mathbf{F_{ID}} = \begin{bmatrix} F_{X,1} & F_{X,2} & \cdots & F_{X,n} \\ F_{Z,1} & F_{Z,2} & \cdots & F_{Z,n} \end{bmatrix} \tag{4.18}$$

In the same way, the $2 \times n$ matrix $\mathbf{\Delta U_{NT}}$ stores the difference between the position of the tool in the ideal machining ($\mathbf{U_{ID}}$) and the measurements coming from the nominal test $\mathbf{U_{NT}}$ (i.e. the point by point deflection measured by the nominal test).

$$\mathbf{\Delta U_{NT}} = \mathbf{U_{ID}} - \mathbf{U_{NT}} \tag{4.19}$$

Each column of *Equation 4.18* should be univocally related to one column of *Equation 4.19* by means of a 2×2 stiffness matrix $\mathbf{K}_{R(2)}$.

$$\mathbf{K}_{R(2)} = \begin{bmatrix} k_{xx(2)} & k_{xz(2)} \\ k_{zx(2)} & k_{zz(2)} \end{bmatrix} \tag{4.20}$$

$$\mathbf{F_{ID}} = \mathbf{K}_{R(2)} \cdot \mathbf{\Delta U_{NT}} \tag{4.21}$$

Managing the terms of *Equation 4.21*, the system can be redefined as an overdetermined problem of n equations in 4 unknowns, where the unknowns are the four

components of the robot stiffness matrix. Moreover, it can be decoupled as follows:

$$\mathbf{\Delta U}_{\mathbf{NT}}^{T} \cdot \begin{bmatrix} k_{xx(2)} \\ k_{xz(2)} \end{bmatrix} = \mathbf{F}_{\mathbf{ID}_X}^{T} \tag{4.22a}$$

$$\mathbf{\Delta U}_{\mathbf{NT}}^{T} \cdot \begin{bmatrix} k_{zx(2)} \\ k_{zz(2)} \end{bmatrix} = \mathbf{F}_{\mathbf{ID}_Z}^{T} \tag{4.22b}$$

Where $\mathbf{F}_{\mathbf{ID}_X}^{T}$ and $\mathbf{F}_{\mathbf{ID}_Z}^{T}$ are two $n \times 1$ column vectors extracted form the transpose of $\mathbf{F_{ID}}$. Each of the two systems can be solved with respect to the stiffness coefficients by means of an ordinary least square optimization; the solution would be optimal in the sense that it would minimize the sum of the squares of the residuals made in the results of every single equation. For example, collecting $k_{xx(2)}$ and $k_{xz(2)}$ in a single column vector $\mathbf{k}_{F_X}$, the ordinary least square associated to the first line of *Equation 4.22* can be formally expressed as follows.

$$\min_{\mathbf{k}_{F_X}} \left\| \ \mathbf{\Delta U}_{\mathbf{NT}}^{T} \cdot \mathbf{k}_{F_X} - \mathbf{F}_{\mathbf{ID}_X}^{T} \ \right\|_2^2 \tag{4.23}$$

The optimal solution $\hat{\mathbf{k}}_{F_X}$ is found introducing the Moore-Penrose inverse matrix of $\mathbf{\Delta U}_{\mathbf{NT}}^{T}$.

$$\left[\mathbf{\Delta U}_{\mathbf{NT}}^{T}\right]^{+} = \left[\mathbf{\Delta U_{NT}} \cdot \mathbf{\Delta U}_{\mathbf{NT}}^{T}\right]^{-1} \cdot \mathbf{\Delta U_{NT}} \tag{4.24}$$

$$\hat{\mathbf{k}}_{F_X} = \left[\mathbf{\Delta U}_{\mathbf{NT}}^{T}\right]^{+} \cdot \mathbf{F}_{\mathbf{ID}_X}^{T} \tag{4.25}$$

Repeating the same approach for the stiffness coefficients related to the z-component of the force, $\mathbf{K}_{R(2)}$ can be finally assembled.

$$\mathbf{K}_{R(2)} = \begin{bmatrix} 779.37 & -563.74 \\ -436.71 & 1374.00 \end{bmatrix} \tag{4.26}$$

With N/mm as unit of measurement.

4.2.3 Comparison of the two methods

Comparing the two methods is immediately remarkable the different sizes of the two stiffness matrices. Following method 1, the analysis can be carried out along any direction imposing the right loading condition; vice versa, method 2 is constrained to the machining direction imposed by the experimental test. Anyway, $\mathbf{K}_{R(1)}$ and $\mathbf{K}_{R(2)}$ are perfectly comparable taking into account the right axis. Both the artificial loading of method 1 and the machining of the nominal test used in method 2 refer to the same reference system, the comparison of the two stiffness matrices can be performed taking into account the first and the third row and column of $\mathbf{K}_{R(1)}$.

Results appear to be coherent especially along the first column (i.e. the deflections along the x-axis) while the method 1 seems to react in a stiffer way with respect to method 2 regarding the vertical deflections. The negative sign of the off-diagonal terms suggests that in this particular configuration Staübli TX200 reacts with a negative force along the orthogonal axis when it pushes against the lamina in a given direction.

To better understand how the stiffness of the robot impacts on the final shape of the metal sheet, is useful to refer to the compliance matrix instead of the stiffness one. In this way a direct evaluation of the deflections is provided for given input forces.

$$\mathbf{C}_{R(1)} = \begin{bmatrix} 1.54 & 0.19 \\ 0.79 & 1.02 \end{bmatrix} \tag{4.27a}$$

$$\mathbf{C}_{R(2)} = \begin{bmatrix} 1.67 & 0.68 \\ 0.53 & 0.95 \end{bmatrix} \tag{4.27b}$$

Data are expressed in mm/kN and $\mathbf{C}_{R(1)}$ only accounts the components along x-direction and z-direction coming from the stiffness matrix evaluated by means of method 1.

The two terms on the principal diagonal show a difference of less than 0.15 mm/KN; the deflection along the vertical direction caused by a force applied in the x-direction also appears comparable, with a difference about 0.25 mm if 1000 N are applied. Concerning the other off-diagonal term, as expected, method 1 assumes a stiffer behavior of the robot with respect to the result obtained using the nominal machining as reference. Despite the significant difference between the two compliance terms, the maximum force in the z-direction is expected to be about 2000 N and so, if the wrong value is assumed, the error should be about 1 mm.

Is interesting to note how, even though the principle adopted to reach $\mathbf{K}_{R(2)}$ is purely mathematics and the physics of the problem is not taken into account, the asymmetry of the matrix is not too marked, according with the Maxwell-Betti principle of reciprocity. The same cannot be said for $\mathbf{K}_{R(2)}$.

4.3 Compensated trajectory

So far, the input trajectory applied to Staübli TX200 did not take into account the inner deflections of the robot. A fraction of the torques generated by the actuators is absorbed by the joints of the robot, a lower level of the forces exchanged between the end effector and the metal sheet are measured with respect to the ideal process and the result is an undersized machining with the final shape slight different from the expected one. The information collected in the analysis of the Staübli TX200 stiffness plays a dominant role to fix this issue. According to Hooke's law, is reasonable to assume that the fraction of the transmitted forces absorbed by the robot is proportional to the deflections experienced by itself. The input trajectory can be thus modified accordingly, adding an additional term able to counteract the compliance losses of the process.

$$\mathbf{U_{ALG}} = \mathbf{U_{ID}} + \mathbf{F_{ID}} \cdot \mathbf{C}_R \tag{4.28}$$

The compensated trajectory $\mathbf{U_{ALG}}$ used as input for the final experiment should be able to counteract the internal deflections of Staübli TX200. It merges the information coming from the ABAQUS simulation of the ideal machining and the contribution given by the mechanical compliance of the robot evaluated through the experimental tests.

Chapter 5

Results

5.1 Experimental validation

The same procedure used for the nominal test is proposed again for the compensated experiment: the arrangement of the components, the calibration of the measurement system, the definition of the reference frame and all the process parameters are kept unchanged. $\mathbf{K}_{R(1)}$ is selected for the compensation; an ad hoc Python script processes the data coming from ABAQUS and the stiffness matrix experimentally defined, it merges the data with the ideal trajectory and sends the compensated trajectory to RoboDK. It will be the input for Staübli TX200.

RoboDK simulates the machining and generates the G-code; finally the code is uploaded on the Staübli controller and is run.

5.1.1 An unexpected error

The tracked path of the tool was expected to match the ideal trajectory required to shape the final part. Curiously, the output of the machining do not fit the predicted curves. Forces appear to be not sufficiently high to allow the tool to achieve the right position within the metal sheet. The obtained results are shown in the figures below.

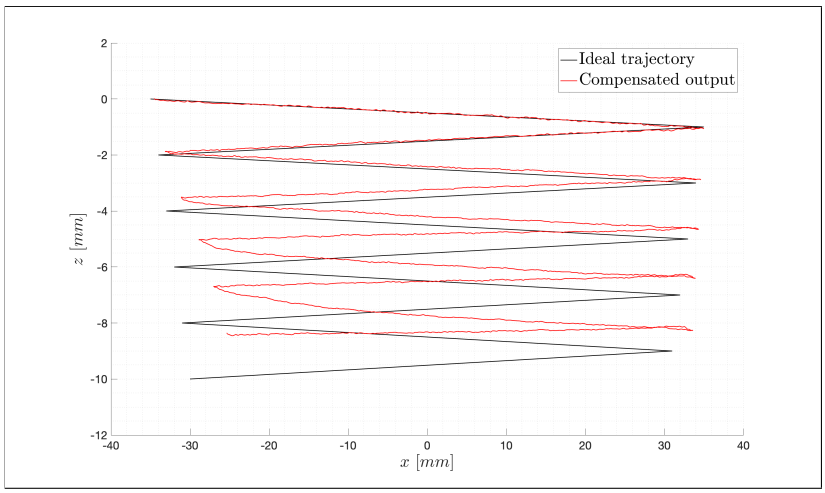

Figure 5.1: Tool trajectory vs Ideal trajectory (Compensated test)

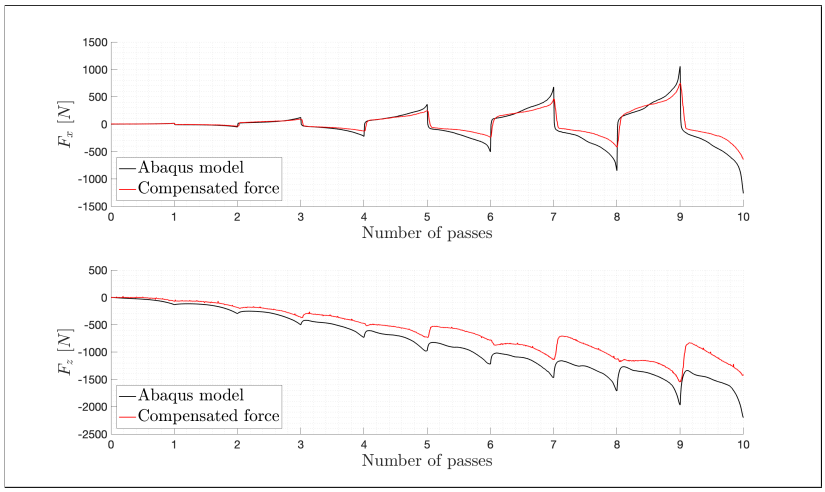

Figure 5.2: Measured forces vs Ideal forces (Compensated test)

The level of the ideal forces were promptly verified with the experimental validation described in *Chapter 2*, no doubt comes from the definition of the ideal trajectory and two different set of data were used to compute a reasonable stiffness matrix. The choice of method 1 with respect to method 2 does not appear to be the cause of the error since the expected difference coming from the different k_{xz} would not justify the result of the experiment.

Granting the correctness of the input, the error must lie in the code implemented to manage the huge amount of information. After an accurate line-by-line review of all the scripts used in the project, the mistake was found in the logic controlling the data acquisition from ABAQUS. When the finite element environment was presented, the symmetry of the model was highlighted to point out the fact that the exported

forces had to be doubled to simulate the correct magnitude reached by the machining. The reason derived from the position of the point at which the forces are evaluated, lying on the symmetry plane of the structure. This issue was correctly implemented when the results of the simulation were compared with the CNC experiment, but it was omitted when the forces where used to evaluate the compensation term. This can reasonably explains the deficiency of the result: the additional term used to compensate the stiffness of the robot is proportional to the forces reached in the process; an underestimation of the forces inexorably lead to the weakness of the compensation.

5.1.2 An intuitive solution

Unfortunately, no further experiments could be carried out due to a lack of 5086-H111 aluminum sheets. The algorithm, indeed, is strictly related to the material-robot coupling since the finite element simulation is affected by the mechanical properties of the lamina.

Anyway, the information collected so far are enough to deploy a plausible solution of the problem. In fact, it is correct to state that the tracked output summed up to the expected deflection experienced during the process should be similar to the input trajectory used for the experiment.

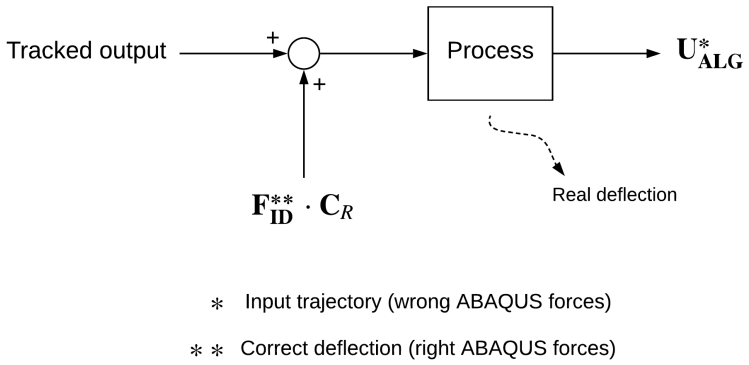

Figure 5.3: Proposed solution (scheme)

This digital solution can be tested with both the compliance matrices previously evaluated. It is a valid alternative to check the reliability of the algorithm since the computation of the stiffness matrices (and compliance matrices) is not depending on the results obtained by the compensated experiment.

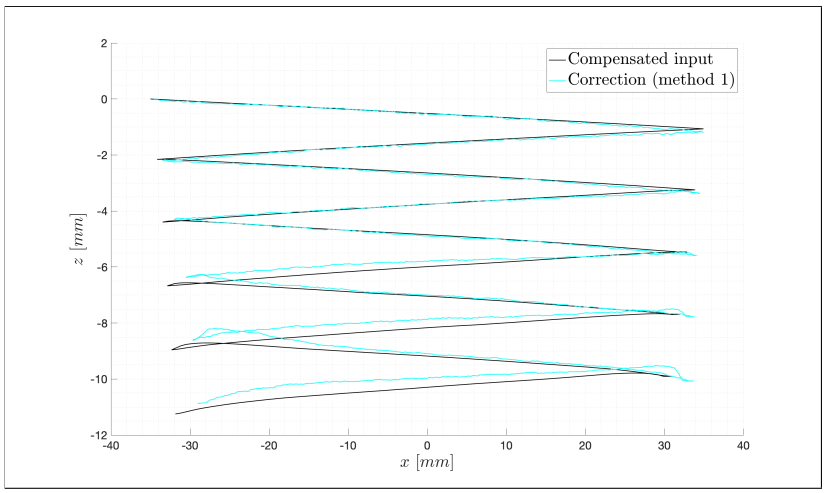

Figure 5.4: Proposed solution (method 1)

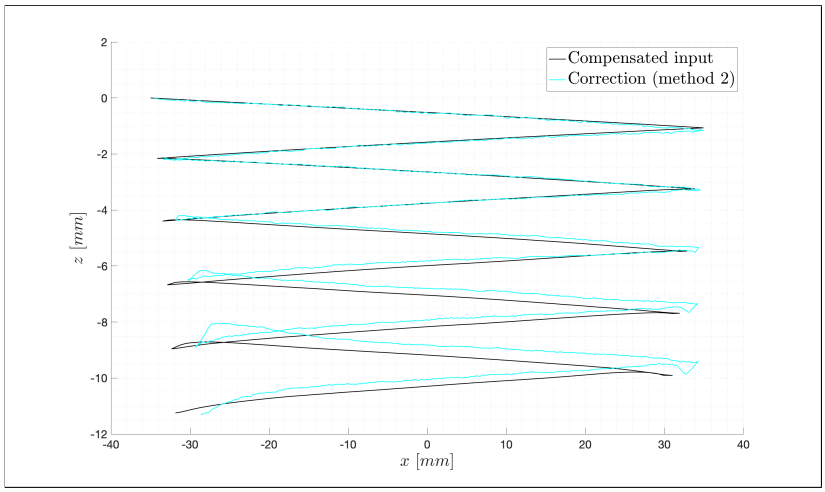

Figure 5.5: Proposed solution (method 2)

Using this approach the results are quite satisfactory. A small offset can be perceived at the boundaries of the strokes of the tool and it may be due to the combination of two effects. The first motivation is the slight increment of the forces when the tool approaches the clamping zone; it's reasonable that some nonlinear and non-predictable effects take place in that area, nullifying the effect of the prediction. The second issue is the confined asymmetric behavior experienced by the tool when the robot changes direction and moves along the positive x-direction (caught in the nominal test). These two aspects may lead to the deficiency of the algorithm in correspondence of the high-depth left boundaries of the furrow and, as consequence, it also causes the misalignment of the successive right boundaries.

In a similar way, also forces can be digital simulated under the hypothesis of cor-

rect prediction of the deflection. In this case the comparison is different, since the available data concerns the ideal forces (coming from ABAQUS) and the forces measured during the compensated experiment. Due to the error made in the evaluation of the compensated trajectory, the algorithm was able to account only the half of the deflection; it's thus possible to sum up the missing percentage to predict the expect trend of the forces.

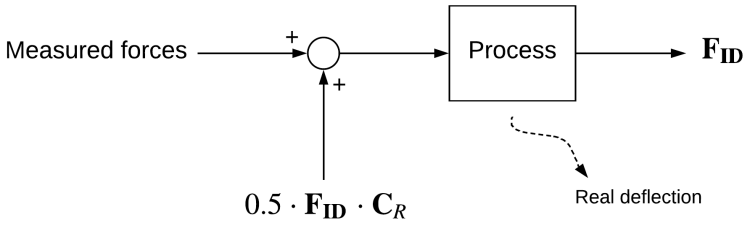

Figure 5.6: Proposed solution applied to forces (scheme)

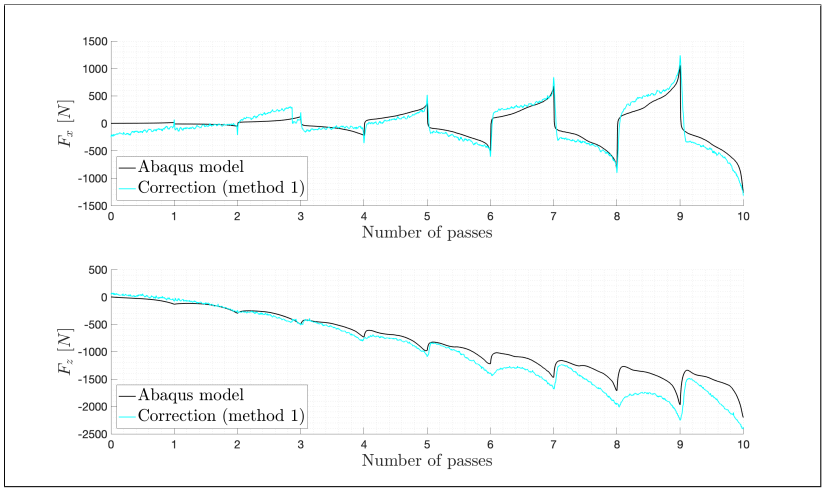

Figure 5.7: Proposed solution applied to forces (method 1)

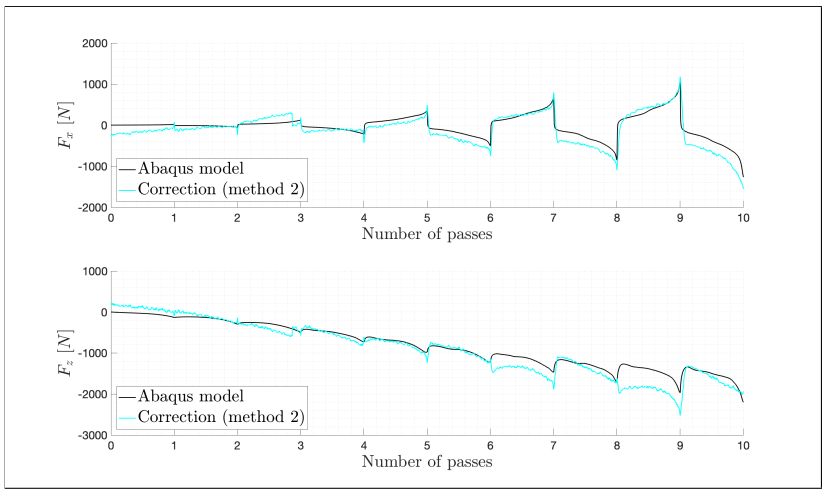

Figure 5.8: Proposed solution applied to forces (method 2)

Again, the simulation seems to confirm the efficiency of the procedure. In this case the compensation appears to be very effective when the robot moves backward (even passes), while some unknown effects degrades the performance in the opposite direction. The results of the trend of the forces are coherent with the graphs plotting the trajectories.

It's difficult to say which of the two stiffness matrices $\mathbf{K}_{R(1)}$ or $\mathbf{K}_{R(2)}$ best represents the real attitude of the Staübli TX200. Method 1 seems to be more coherent according to the trajectories, but method 2 shows best performance in force comparison. Of course, these are not real experiments but only mathematical representations of the phenomena, but both the strategies are coherent and reliable.

Chapter 6

Conclusions and perspectives

6.1 Conclusions

This thesis shown an effective procedure to counteract the geometric errors of a robot assisted ISF application generated by the compliances of Staübli TX200 mechanical parts. The experiment was carried out referring to a linear furrow of 70 mm width and 10 mm depth dug in the center of a 1 mm thickness metal sheet, but the proposed methodology has a general validity and it can be extended to other robot assisted ISF processes. Nevertheless, the application is strictly connected to the material-robot coupling and tailored studies of the material, process and robot are needed.

The compensation of the geometric deficiency due to the inner deflections of the robot is performed adding to the ideal trajectory a term depending on the forces involved in the machining and on the stiffness behavior of the robot. Being an offline algorithm, no particular sensors are needed and no specific control logics have to be implemented. The two key elements are an effective numerical simulation of the process and an accurate study of the elastic response of Staübli TX200. The first goal is achieved by processing through ABAQUS 6.13 a precise finite element reconstruction of the machining able to estimate the forces involved during the manufacturing, while the robot compliance is evaluated by means of experimental tests.

Concerning the finite element simulation, solid elements appear to be more convenient for the design of the metal sheet since the process is affected by nonlinear effects and the localized deformations performed by the movement of the tool makes the hypothesis of thin plate no more reliable. Linear elements are selected to make the

computational cost sustainable and 5 layers of 0.2 *mm* C3D8R are used to reproduce the thickness of the lamina. The combined choice of the multilayer and the linear integration method allows to remove *shear locking* and *hourglassing* effect. The hardening law of the material plays a significant role for the evolution of the plastic zone and it has to be investigated with attention; Voce's law was selected for the description of 5086-H111 aluminum and the parameters were selected from previous studies found in literature. The simulation is very sensitive with respect to the mesh size; a plausible trade-off between performance and computation time was found selecting 0.5 *mm* as distance of the seeds in the part of the plate directly affected by the machining and, introducing different partitions according to the criticality, coarse mesh was selected in zones less prone to deformations. Despite the implementation of lubricant on the worked surface, friction between the tool and the metal sheet seems to be still present and affects the level of the forces: by means of parameter tuning, a friction coefficient equal to 0.1 was selected. The effectiveness of the FE model was proved testing the machining on a CNC machine and assuming an infinite stiffness of the structure.

Mechanical stiffness of Staübli TX200 has been estimated adopting two different approaches. Through a system of weights and cables, the robot was loaded (in the same configuration used for the machining) with a set of different weights, the experienced deflections were measured and the resulting stiffness matrix was found by means of an optimization procedure (method 1). Alternatively, a nominal test was performed and the tracked trajectory of the tool was compared with the ideal expected trajectory; starting from the measured deflection and the available forces coming from ABAQUS, a plausible stiffness matrix is found (method 2). The second method is strictly related to the machining, it does not loose the general validity but it is restricted to the axis loaded during in the process. The two different stiffness matrices are coherent one to each other; both show off-diagonal negative terms and an asymmetric shape. The asymmetry of the matrices (more pronounced in method 1) is justified by the fact that *mathematics does not care about physics* and the optimization procedures numerically evaluate the solution neglecting the nature of the problem and accounting the effect of nonlinear effects. Nevertheless, in the outcome of method 2 asymmetry is not too marked.

The test performed to confirm the procedure unexpectedly failed due to an error

in the script; unfortunately, no other test has been assessed due to the absence of additional 5086-H111 aluminum sheets. Once the error was found, a mathematical correction was added to the results of the experiment to certify the correctiveness of the strategy.

Results are satisfactory. The same numerical values obtained for the stiffness matrix can be used again in others applications keep the same orientation of Staübli TX200; vice versa, finite elements part has to be re-computed if any changes are applied to material or geometry of the part. Computational time of FE represents the bottleneck of the procedure and may become relevant if complex geometries are involved.

6.2 Prespectives

It should be noted that the effectiveness of this methodology is restricted to the error generated by the compliance behavior of the robot and it's not able to balance the springback contribution too. Elastic recovery after machining is the other crucial aspect related to this technology and, more in general, to the processes involving plastic deformations. An interesting improvement could be the modeling of the springback effect to account it in the compensation algorithm.

Moreover, since one of the principal weakness of the robot assisted ISF is the low level of the maximum force reached during the machining, a future study of the department of Génie Mécanique et Automatique dell'Institut National des Sciences Appliquées di Rennes (that already supported this project) will be the implementation of an ultrasonic tool to further decrease the forming forces needed to complete the manufacturing of the part.

Bibliography

[1] L. Edward, "Apparatus and process for incremental dieless forming," Sep. 19 1967, uS Patent 3,342,051.

[2] K. Jackson and J. Allwood, "The mechanics of incremental sheet forming," *Journal of materials processing technology*, vol. 209, no. 3, pp. 1158–1174, 2009.

[3] Y. Kim and J. Park, "Effect of process parameters on formability in incremental forming of sheet metal," *Journal of materials processing technology*, vol. 130, pp. 42–46, 2002.

[4] J. Allwood, D. Shouler, and A. E. Tekkaya, "The increased forming limits of incremental sheet forming processes," in *Key Engineering Materials*, vol. 344. Trans Tech Publ, 2007, pp. 621–628.

[5] P. Eksteen and A. Van der Merwe, "Incremental sheet forming (isf) in the manufacturing of titanium based plate implants in the bio-medical sector," *Proceedings of 42nd Computers and Industrial Engineering*, pp. 15–18, 2012.

[6] T. Trzepieciński, B. Krasowski, A. Kubit, and D. Wydrzyński, "Possibilities of application of incremental sheet-forming technique in aircraft industry," *Zeszyty Naukowe Politechniki Rzeszowskiej. Mechanika*, pp. 87–100, 2018.

[7] Y. Li, X. Chen, Z. Liu, J. Sun, F. Li, J. Li, and G. Zhao, "A review on the recent development of incremental sheet-forming process," *The International Journal of Advanced Manufacturing Technology*, vol. 92, no. 5-8, pp. 2439–2462, 2017.

[8] L. Filice, L. Fratini, and F. Micari, "Analysis of material formability in incremental forming," *CIRP annals-Manufacturing technology*, vol. 51, no. 1, pp. 199–202, 2002.

[9] T. Kim and D. Yang, "Improvement of formability for the incremental sheet metal forming process," *International Journal of Mechanical Sciences*, vol. 42, no. 7, pp. 1271–1286, 2000.

[10] M. Shim and J. Park, "The formability of aluminum sheet in incremental forming," *Journal of Materials Processing Technology*, vol. 113, no. 1-3, pp. 654–658, 2001.

[11] J. Wang, M. Nair, and Y. Zhang, "An efficient force prediction strategy in single point incremental sheet forming," *Procedia Manufacturing*, vol. 5, pp. 761–771, 2016.

[12] I. Bagudanch, G. Centeno, C. Vallellano, and M. Garcia-Romeu, "Forming force in single point incremental forming under different bending conditions," *Procedia Engineering*, vol. 63, pp. 354–360, 2013.

[13] J. Duflou, Y. Tunckol, A. Szekeres, and P. Vanherck, "Experimental study on force measurements for single point incremental forming," *Journal of Materials Processing Technology*, vol. 189, no. 1-3, pp. 65–72, 2007.

[14] G. Ambrogio, L. Filice, F. Gagliardi, and F. Micari, "Sheet thinning prediction in single point incremental forming," in *Advanced materials research*, vol. 6. Trans Tech Publ, 2005, pp. 479–486.

[15] Y. Li, X. Chen, W. Zhai, L. Wang, J. Li, and Z. Guoqun, "Effects of process parameters on thickness thinning and mechanical properties of the formed parts in incremental sheet forming," *The International Journal of Advanced Manufacturing Technology*, vol. 98, no. 9-12, pp. 3071–3080, 2018.

[16] G. Hussain and L. Gao, "A novel method to test the thinning limits of sheet metals in negative incremental forming," *International Journal of Machine Tools and Manufacture*, vol. 47, no. 3-4, pp. 419–435, 2007.

[17] M. Yang, Z. Yao, Y. Li, P. Li, F. Cui, and L. Bai, "Study on thickness thinning ratio of the forming parts in single point incremental forming process," *Advances in Materials Science and Engineering*, vol. 2018, 2018.

[18] F. Han, J. Mo, P. Gong, and M. Li, "Method of closed loop springback compensation for incremental sheet forming process," *Journal of Central South University of Technology*, vol. 18, no. 5, p. 1509, 2011.

[19] F. Han, J. Mo, H. Qi, R. Long, X. Cui, and Z. Li, "Springback prediction for incremental sheet forming based on fem-psonn technology," *Transactions of Nonferrous Metals Society of China*, vol. 23, no. 4, pp. 1061–1071, 2013.

[20] T. Tuominen, "Method and apparatus for forming three-dimensional shapes in a sheet metal," *Patent number WO2004030843A1*, 2004.

[21] L. Vihtonen, A. Puzik, and T. Katajarinne, "Comparing two robot assisted incremental forming methods: incremental forming by pressing and incremental hammering," *International Journal of Material Forming*, vol. 1, no. 1, pp. 1207–1210, 2008.

[22] J. K. Salisbury, "Active stiffness control of a manipulator in cartesian coordinates," in *1980 19th IEEE conference on decision and control including the symposium on adaptive processes*. IEEE, 1980, pp. 95–100.

[23] A. Klimchik, A. Pashkevich, D. Chablat, and G. Hovland, "Compliance error compensation technique for parallel robots composed of non-perfect serial chains," *Robotics and Computer-Integrated Manufacturing*, vol. 29, no. 2, pp. 385–393, 2013.

[24] J. Belchior, M. Guillo, E. Courteille, P. Maurine, L. Leotoing, and D. Guines, "Off-line compensation of the tool path deviations on robotic machining: Application to incremental sheet forming," *Robotics and Computer-Integrated Manufacturing*, vol. 29, no. 4, pp. 58–69, 2013.

[25] H. Meier, B. Buff, R. Laurischkat, and V. Smukala, "Increasing the part accuracy in dieless robot-based incremental sheet metal forming," *CIRP annals*, vol. 58, no. 1, pp. 233–238, 2009.

[26] J. Belchior, "Développement d'une approche couplée matériau / structure machine: application au formage incrémental robotisé," Ph.D. dissertation, INSA Rennes, 2013.

[27] J. L. Fanchon, *Guide des sciences et technologies industrielles.* Nathan, 2013.

[28] J. E. Shigley, *Shigley's mechanical engineering design.* Tata McGraw-Hill Education, 2011.

[29] D. Ludwigson, "Modified stress-strain relation for fcc metals and alloys," *Metallurgical Transactions*, vol. 2, no. 10, pp. 2825–2828, 1971.

[30] C. Marilena, C. T. Butuc, and G. J. J. Barlat, "Analysis of sheet metal formability through isotropic and kinematic hardening models [j]," *European Journal of Mechanics A/Solids*, vol. 30, no. 4, pp. 532–546, 2011.

[31] C. Henrard, C. Bouffioux, P. Eyckens, H. Sol, J. Duflou, P. Van Houtte, A. Van Bael, L. Duchene, and A. Habraken, "Forming forces in single point incremental forming: prediction by finite element simulations, validation and sensitivity," *Computational mechanics*, vol. 47, no. 5, pp. 573–590, 2011.

[32] C. Zhang, L. Leotoing, D. Guines, and E. Ragneau, "Experimental and numerical study on effect of forming rate on aa5086 sheet formability," *Materials Science and Engineering: A*, vol. 527, no. 4-5, pp. 967–972, 2010.

[33] J. Belchior, L. Leotoing, D. Guines, E. Courteille, and P. Maurine, "A process/-machine coupling approach: application to robotized incremental sheet forming," *Journal of Materials Processing Technology*, vol. 214, no. 8, pp. 1605–1616, 2014.

[34] W. Emmens and A. H. van den Boogaard, "An overview of stabilizing deformation mechanisms in incremental sheet forming," *Journal of Materials Processing Technology*, vol. 209, no. 8, pp. 3688–3695, 2009.

[35] D. Systèmes, "Abaqus analysis user's manual," *Simulia Corp. Providence, RI, USA*, 2007.

[36] R. D. Cook, *Finite element modeling for stress analysis.* Wiley, 1994.

[37] R. D. Cook *et al.*, *Concepts and applications of finite element analysis.* John Wiley & Sons, 1989.

[38] ATI, *Six-Axis Force/Torque Sensor System, Installation and Operation Manual.*

[39] Staübli, "TX200 Range, 6 axis industrial robot," https://www.staubli.com/en/file/5258.show, 2019, [Online; accessed 30-June-2019].

[40] R. S. Hartenberg and J. Denavit, "A kinematic notation for lower pair mechanisms based on matrices," *Journal of applied mechanics*, vol. 77, no. 2, pp. 215–221, 1955.

[41] M. W. Spong and M. Vidyasagar, *Robot dynamics and control*. John Wiley & Sons, 2008.

[42] Metris, "K610-CMM, the High-Accuracy Portable CMM with 17 m^3 measurement volume," http://www.metris3d.hu/k610_cmm_eu_0905.pdf, 2005, [Online; accessed 30-June-2019].

[43] J. Palau, "Speed reducer of the cycloidal type for robots and other industrial manipulators," May 17 1994, uS Patent 5,312,305.

[44] C. Dumas, S. Caro, M. Cherif, S. Garnier, and B. Furet, "Joint stiffness identification of industrial serial robots," *Robotica*, vol. 30, no. 4, pp. 649–659, 2012.

Appendix A

Finite element procedure

A.1 Strain-Displacement matrix

Finite element method is based on a sequence of steps aimed at define and solve a set of algebraic equations. From the solution of a continuum problem, typically based on a partial differential equations system, the problem is approximated with a system of algebraic linear equations, where the quantities of interest are determined at specific points, i.e. the nodes. In this way, the problem passes from an infinite number of unknowns to a finite number of unknowns. The system of algebraic equations can be solved automatically by a computer. The results obtained by using this model are of high accuracy, within the limitations of the chosen model and the precision of the computer code. Generally, the physical phenomenon is not known or cannot be solved exactly; thus a hypothesis is formulated about the trend of the displacements within every element. In each element, the value of field quantity, for example displacement, is interpolated from its values on the nodes. By connecting elements, this field quantity will be interpolated throughout the whole structure. Interpolation functions used to approximate the unknown field in terms of nodal values are called *shape functions*.

Typically the shape functions are polynomial, independent from the physical phenomenon that has to be simulated. The solution of the elastic problem is obtained in terms of nodal displacements. Since strains and consequently stresses are derived from displacements, their accuracy depends highly on the shape functions. By suitably assigning the loads and the boundary conditions, in such a way that they are referred to the nodes, the following system of equations is obtained:

$$\mathbf{K_{FE}} \cdot \mathbf{d_{FE}} = \mathbf{f_{FE}} \tag{A.1}$$

Forces applied to the node (loads and boundary conditions) are described by the vector $\mathbf{f_{FE}}$ and the displacements are collected in vector $\mathbf{d_{FE}}$. $\mathbf{K_{FE}}$ is the stiffness matrix that introduces the geometry and the material. It expresses the reaction (nodal) forces of the model when a unit displacement is applied at nodes. The displacement can be obtained by the inversion of the stiffness matrix.

$$\mathbf{d_{FE}} = \mathbf{K_{FE}}^{-1} \cdot \mathbf{f_{FE}} \tag{A.2}$$

In FE, the trend of the displacements within an element is assumed as a polynomial shape function. Each single shape function describes how the displacement varies when the corresponding degree of freedom is equal to 1 and the others are zero. Degrees of freedom are defined as the movements and the rotations of the node.

Let's assume, as example, the case of an in-plane beam. It is characterized by two nodes and six degrees of freedom (horizontal and vertical translation and rotation of each node). The curvature $v''(x)$ of the elastic beam is described by *Equation A.3*.

$$v''(x) = -\frac{M(x)}{E \cdot I_{xx}} \tag{A.3}$$

$M(x)$ represents the generic moment applied to the node, E is the Young's modulus and I_{xx} is the second moment of the cross sectional area. If constant loads are applied to the nodes, following the beam theory the distribution of the moment must be linear along the thickness and thus the vertical displacement v of the beam will be described by a third order polynomial as expressed in *Equation A.4*.

$$v(x) = a_1 \cdot x^3 + a_2 \cdot x^2 + a_3 \cdot x + a_4 \tag{A.4}$$

The four parameters a_i can be found defining a set of boundary conditions referred to the vertical translation and to the rotation of the two nodes. The goal is to define four different polynomials associated to the unitary movement of each of the degree of freedom while the others are locked. It means to solve four systems of four equations by equalizing to zero three of the four boundary conditions and imposing equal to 1 the fourth. Solving each of these systems, the shape function related to the correspondent moving DoF. As example, the shape function referred to a unitary vertical displacement of the left node of the beam is derived starting from the set of boundary conditions shown in *Equations A.5*.

$$v(0) = 1 \tag{A.5a}$$

$$v'(0) = 0 \tag{A.5b}$$

$$v(l) = 0 \tag{A.5c}$$

$$v'(l) = 0 \tag{A.5d}$$

With l the length of the beam.

Substituting the latter set of equations into *Equation A.4*, the first shape function N_1 is found. In the same way, varying the non-null boundary condition, also N_2, N_3 and N_4 can be evaluated.

$$N_1 = 1 - \frac{3 \cdot x^2}{l^2} + \frac{2 \cdot x^3}{l^3} \tag{A.6a}$$

$$N_2 = x - \frac{2 \cdot x^2}{l} + \frac{x^3}{l^2} \tag{A.6b}$$

$$N_3 = \frac{3 \cdot x^2}{l^2} - \frac{2 \cdot x^3}{l^3} \tag{A.6c}$$

$$N_4 = -\frac{x^2}{l} + \frac{x^3}{l^2} \tag{A.6d}$$

The total displacement of any point within the beam is a combination of the single displacements ruled by the corresponding shape functions. Collecting this information

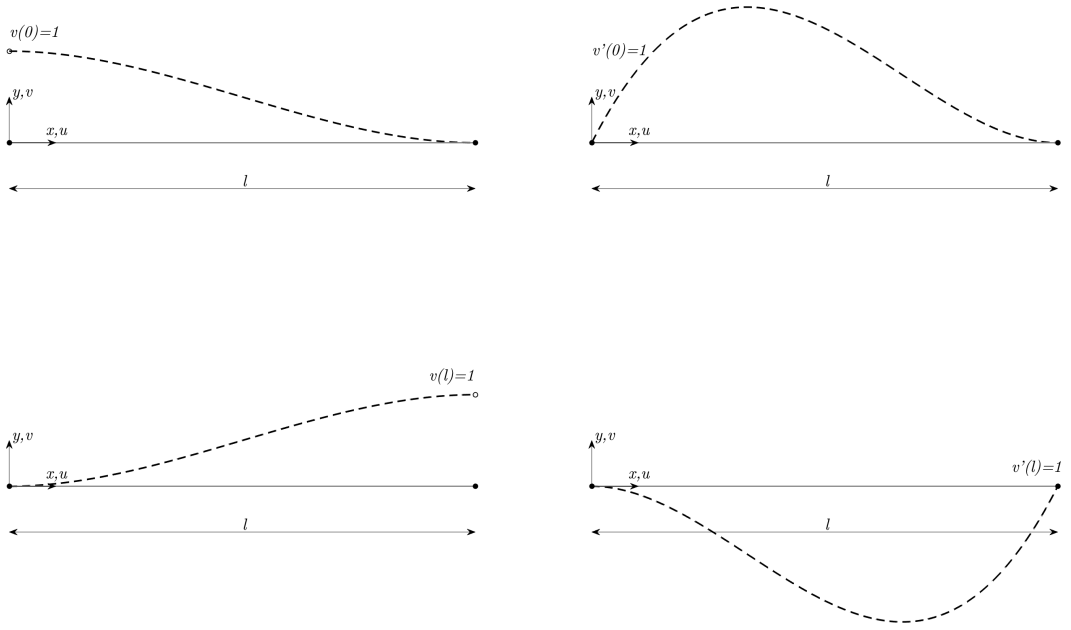

Figure A.1: Shape functions

in matrix form, the expression of the displacement of any generic coordinate of the element $v_B(x)$ can be found.

$$v_B(x) = \begin{bmatrix} N_1 & N_2 & N_3 & N_4 \end{bmatrix} \cdot \begin{Bmatrix} v(0) \\ v'(0) \\ v(l) \\ v'(l) \end{Bmatrix} \tag{A.7}$$

The vector containing the vertical displacements and the rotations of the boundaries of the beam, collects four of the six degrees of freedom of the element and can be expressed in compact form as **v**:

$$\mathbf{v} = \begin{Bmatrix} v(0) & v'(0) & v(l) & v'(l) \end{Bmatrix}^T \tag{A.8}$$

The curvature of the beam is defined as the second derivative of *Equation A.4* and thus becomes:

$$v_B''(x) = \frac{d^2 v_B(x)}{dx^2} = \left[\frac{d^2 N_1}{dx^2} \quad \frac{d^2 N_2}{dx^2} \quad \frac{d^2 N_3}{dx^2} \quad \frac{d^2 N_4}{dx^2} \right] \cdot \mathbf{v} \tag{A.9}$$

The matrix collecting the second derivatives of the shape functions is named *strain-displacement matrix* $\mathbf{B_{FE}}$.

$$\mathbf{B_{FE}} = \left[-\frac{6}{l^2} + \frac{12 \cdot x}{l^3}; \quad -\frac{4}{l} + \frac{6 \cdot x}{l^2}; \quad \frac{6}{l^2} - \frac{12 \cdot x}{l^2}; \quad -\frac{2}{l} + \frac{6 \cdot x}{l^2} \right] \tag{A.10}$$

In the case of two-dimensional beam, $\mathbf{B_{FE}}$ assumes the form of a vector. It is important to note that strain-displacement matrix depends only on the shape of the element.

A.2 Stiffness matrix

Until now, horizontal displacements have been omitted from the evaluation of the total displacement. In fact, since the horizontal displacement generated by an axial load is decoupled from the bending deformation, horizontal contributions can be added separately. Before of that, let's focus on the relationship between the strain-displacement matrix and the stiffness matrix of the beam in the case of zero axial stress. According to Euler-Bernoulli beam theory, strain$\boldsymbol{\varepsilon}$ within the element is expressed by *Equation A.11* (in the simple case of a two-dimensional beam it coincides with the axial strain ε_{xx}, but for a general dissertation vector notation is maintained).

$$\boldsymbol{\varepsilon} = \mathbf{B_{FE}} \cdot \mathbf{v} \tag{A.11}$$

Strain energy U of the beam is evaluated computing the integral of the volumetric strain energy over the whole element volume V (*Equation A.12*).

$$U = \frac{1}{2} \cdot \int_V \boldsymbol{\varepsilon}^T \cdot \mathbf{E_{FE}} \cdot \boldsymbol{\varepsilon} \; dV \tag{A.12}$$

But it can be also expressed as function of the stiffness matrix:

$$U = \frac{1}{2} \cdot \mathbf{v}^T \cdot \mathbf{K_{FE}} \cdot \mathbf{v} \tag{A.13}$$

Thus, equalizing *Equation A.12* and *Equation A.13* and substituting *Equation A.11*, the following formulation of the stiffness matrix is obtained.

$$\mathbf{K_{FE}} = \int_V \mathbf{B_{FE}}^T \cdot \mathbf{E_{FE}} \cdot \mathbf{B_{FE}} \, dV \tag{A.14}$$

Again, for the beam case the latter equation can be rewritten as:

$$\mathbf{K_{FE}} = \int_0^l \mathbf{B_{FE}}^T \cdot E \cdot I_{xx} \cdot \mathbf{B_{FE}} \, dx \tag{A.15}$$

And so:

$$\mathbf{K_{FE}} = E \cdot I_{xx} \cdot \begin{bmatrix} \frac{12}{l^3} & \frac{6}{l^2} & -\frac{12}{l^3} & \frac{6}{l^2} \\ \frac{6}{l^2} & \frac{4}{l} & -\frac{6}{l^2} & \frac{2}{l} \\ -\frac{12}{l^3} & -\frac{6}{l^2} & \frac{12}{l^3} & -\frac{6}{l^2} \\ \frac{6}{l^2} & \frac{2}{l} & -\frac{6}{l^2} & \frac{4}{l} \end{bmatrix} \tag{A.16}$$

A.3 Axial contribution

Contribution of axial load can be added following a similar procedure. No rotation of the beam is induced by the axial load, thus a linear displacement is deduced.

$$u(x) = a_5 \cdot x + a_6 \tag{A.17}$$

Two couples of the unknown parameters can be found solving two systems alternatively imposing the unitary movement of one node and the null-movement of the other. The results will be the two shape functions associated to the horizontal coordinates of the nodes.

Merging the horizontal degrees of freedom of the beam ($u(0)$ and $u(l)$) with the previous vector $\mathbf{v}$ and rearranging the terms, the vector $\mathbf{d_{FE}}$ containing all the DoF of the beam is obtained.

$$\mathbf{d_{FE}} = \left\{ \begin{array}{cccccc} u(0) & v(0) & v'(0) & u(l) & v(l) & v'(l) \end{array} \right\}^T \tag{A.18}$$

To relate the strain $\boldsymbol{\varepsilon}$ to the DoF $\mathbf{d_{FE}}$, the strain-displacement matrix has to be modified accounting the missing contributions related to the horizontal degrees of freedom. These two terms correspond to the first derivative of the two shape functions derived from the solutions of *Equation A.17*. $\mathbf{B_{FE}}$, in fact, collects the strains associated to the degrees of freedom with respect the corresponding loading conditions (i.e. the unitary displacement).

Using the same arrangement of vector $\mathbf{d_{FE}}$, strain-displacement matrix becomes:

$$\mathbf{B_{FE}} = \left[\begin{array}{cccccc} -\dfrac{1}{l}; & -\dfrac{6}{l^2}+\dfrac{12\cdot x}{l^3}; & -\dfrac{4}{l}+\dfrac{6\cdot x}{l^2}; & \dfrac{1}{l}; & \dfrac{6}{l^2}-\dfrac{12\cdot x}{l^2}; & -\dfrac{2}{l}+\dfrac{6\cdot x}{l^2} \end{array} \right] \tag{A.19}$$

And, including the formulation of the axial stiffness, $\mathbf{K_{FE}}$ becomes:

$$\mathbf{K_{FE}} = \left[\begin{array}{cccccc} \dfrac{A_B\cdot E}{l} & 0 & 0 & -\dfrac{A_B\cdot E}{l} & 0 & 0 \\ 0 & \dfrac{E\cdot I_{xx}\cdot 12}{l^3} & \dfrac{E\cdot I_{xx}\cdot 6}{l^2} & 0 & -\dfrac{E\cdot I_{xx}\cdot 12}{l^3} & \dfrac{E\cdot I_{xx}\cdot 6}{l^2} \\ 0 & \dfrac{E\cdot I_{xx}\cdot 6}{l^2} & \dfrac{E\cdot I_{xx}\cdot 4}{l} & 0 & -\dfrac{E\cdot I_{xx}\cdot 6}{l^2} & \dfrac{E\cdot I_{xx}\cdot 2}{l} \\ -\dfrac{A_B\cdot E}{l} & 0 & 0 & \dfrac{A_B\cdot E}{l} & 0 & 0 \\ 0 & -\dfrac{E\cdot I_{xx}\cdot 12}{l^3} & -\dfrac{E\cdot I_{xx}\cdot 6}{l^2} & 0 & \dfrac{E\cdot I_{xx}\cdot 12}{l^3} & -\dfrac{E\cdot I_{xx}\cdot 6}{l^2} \\ 0 & \dfrac{E\cdot I_{xx}\cdot 6}{l^2} & \dfrac{E\cdot I_{xx}\cdot 2}{l} & 0 & -\dfrac{E\cdot I_{xx}\cdot 6}{l^2} & \dfrac{E\cdot I_{xx}\cdot 4}{l} \end{array} \right] \tag{A.20}$$

With A_B the cross section of the beam.

Appendix B

Jacobian evaluation

B.1 MATLAB code

```
clearvars
close all
clc

% Definition of DoF (q) and DH parameters (DH.*)

N=6;
q=sym('q',[N,1]);
DH.q=[q(1),q(2)-pi/2,q(3)-pi/2,q(4),q(5),q(6)+pi/2];
DH.d=[0.64,0,0,0.8,0,0.19]; % [m]
DH.r=[0.26,0.95,0,0,0,0]; % [m]
DH.a=[-pi/2,0,-pi/2,pi/2,-pi/2,0];

% Definition of homogeneous transformation matrices (A)

for i=1:N
    Rz{i}=[cos(DH.q(i)),-sin(DH.q(i)),0,0;sin(DH.q(i)),cos(DH.
        q(i)),0,0;0,0,1,0;0,0,0,1];
    Tz{i}=[1,0,0,0;0,1,0,0;0,0,1,DH.d(i);0,0,0,1];
    Tx{i}=[1,0,0,DH.r(i);0,1,0,0;0,0,1,0;0,0,0,1];
```

```
20      Rx{i}=[1,0,0,0;0,cos(DH.a(i)),-sin(DH.a(i)),0;0,sin(DH.a(i
            )),cos(DH.a(i)),0;0,0,0,1];
21      A{i}=Rz{i}*Tz{i}*Tx{i}*Rx{i};
22  end
23
24  % From symbolic to double
25
26  for k=1:N
27      for i=1:4
28          for j=1:4
29              [c,w]=coeffs(A{k}(i,j));
30              C=round(double(c),4);
31              AA{k}(i,j)=dot(C,w);
32          end
33      end
34  end
35
36  % Definition of rotation matrices (R0{*}) and translation
        vectors (T0{*})
37
38  H0{1}=AA{1};
39  z{1}=sym([0;0;1]);
40
41  for i=2:N
42      H0{i}=H0{i-1}*AA{i};
43      z{i}=H0{i-1}(1:3,3);
44  end
45  O{1}=[0;0;0]; % Robot base
46  for i=2:N
47      O{i}= H0{i-1}(1:3,4);
48  end
49
```

```
50 P=H0{N}(1:3,4)+[0;0;.0.275]; % End effector [m]
51
52 % Definition of the Jacobian (J)
53
54 for i=1:N
55     Jv(:,i)=cross(z{i},P-O{i});
56     Jw(:,i)=z{i};
57 end
58
59 J=simplify([Jv;Jw]);
```

B.2 Jacobian

The elements of Staübli TX200 Jacobian are reported. Please note that for a correct estimation the unite of measurement of L_T must be in meter.

$$\mathbf{J} = \begin{bmatrix} J_{11} & J_{12} & J_{13} & J_{14} & J_{15} & J_{16} \\ J_{21} & J_{22} & J_{23} & J_{24} & J_{25} & J_{26} \\ J_{31} & J_{32} & J_{33} & J_{34} & J_{35} & J_{36} \\ J_{41} & J_{42} & J_{43} & J_{44} & J_{45} & J_{46} \\ J_{51} & J_{52} & J_{53} & J_{54} & J_{55} & J_{56} \\ J_{61} & J_{62} & J_{63} & J_{64} & J_{65} & J_{66} \end{bmatrix} \tag{B.1}$$

$$
\begin{aligned}
J_{11} = & + \frac{19}{100} \cdot cos(q_4) \cdot sin(q_1) \cdot sin(q_2) \cdot sin(q_3) \cdot sin(q_5) - \frac{19}{20} \cdot sin(q_1) \cdot sin(q_2) + \\
& - \frac{4}{5} \cdot cos(q_2) \cdot sin(q_1) \cdot sin(q_3) - \frac{4}{5} \cdot cos(q_3) \cdot sin(q_1) \cdot sin(q_2) + \\
& - \frac{19}{100} \cdot cos(q_1) \cdot sin(q_4) \cdot sin(q_5) - \frac{19}{100} \cdot cos(q_2) \cdot cos(q_5) \cdot sin(q_1) \cdot sin(q_3) + \\
& - \frac{19}{100} \cdot cos(q_3) \cdot cos(q_5) \cdot sin(q_1) \cdot sin(q_2) + \\
& - \frac{19}{100} \cdot cos(q_2) \cdot cos(q_3) \cdot cos(q_4) \cdot sin(q_1) \cdot sin(q_5) - \frac{13}{50} \cdot sin(q_1)
\end{aligned}
\tag{B.2}
$$

$$
\begin{aligned}
J_{12} = & + \frac{1}{100} \cdot cos(q_1) \cdot \Big[\, 95 \cdot cos(q_2) + 80 \cdot cos(q_2) \cdot cos(q_3) - 80 \cdot sin(q_2) \cdot sin(q_3) + \\
& + 19 \cdot cos(q_2) \cdot cos(q_3) \cdot cos(q_5) - 19 \cdot cos(q_5) \cdot sin(q_2) \cdot sin(q_3) + \\
& - 19 \cdot cos(q_2) \cdot cos(q_4) \cdot sin(q_3) \cdot sin(q_5) + \\
& - 19 \cdot cos(q_3) \cdot cos(q_4) \cdot sin(q_2) \cdot sin(q_5) + L_T \, \Big]
\end{aligned}
\tag{B.3}
$$

$$
\begin{aligned}
J_{13} = & - \frac{1}{100} \cdot cos(q_1) \cdot \Big[\, 80 \cdot sin(q_2) \cdot sin(q_3) - 80 \cdot cos(q_2) \cdot cos(q_3) + \\
& - 19 \cdot cos(q_2) \cdot cos(q_3) \cdot cos(q_5) + 19 \cdot cos(q_5) \cdot sin(q_2) \cdot sin(q_3) + \\
& + 19 \cdot cos(q_2) \cdot cos(q_4) \cdot sin(q_3) \cdot sin(q_5) + \\
& + 19 \cdot cos(q_3) \cdot cos(q_4) \cdot sin(q_2) \cdot sin(q_5) - L_T \, \Big]
\end{aligned}
\tag{B.4}
$$

$$
\begin{aligned}
J_{14} = & + L_T \cdot cos(q_2) \cdot sin(q_1) \cdot sin(q_3) + L_T \cdot cos(q_3) \cdot sin(q_1) \cdot sin(q_2) + \\
& - \frac{19}{100} \cdot cos(q_4) \cdot sin(q_1) \cdot sin(q_5) - \frac{19}{100} \cdot cos(q_1) \cdot cos(q_2) \cdot cos(q_3) \cdot sin(q_4) \cdot sin(q_5) + \\
& + \frac{19}{100} \cdot cos(q_1) \cdot sin(q_2) \cdot sin(q_3) \cdot sin(q_4) \cdot sin(q_5)
\end{aligned}
\tag{B.5}
$$

$$
\begin{aligned}
J_{15} = \; & + L_T \cdot cos(q_1) \cdot cos(q_4) - \frac{19}{100} \cdot cos(q_5) \cdot sin(q_1) \cdot sin(q_4) + \\
& - L_T \cdot cos(q_2) \cdot cos(q_3) \cdot sin(q_1) \cdot sin(q_4) - \frac{19}{100} \cdot cos(q_1) \cdot cos(q_2) \cdot sin(q_3) \cdot sin(q_5) + \\
& - \frac{19}{100} \cdot cos(q_1) \cdot cos(q_3) \cdot sin(q_2) \cdot sin(q_5) + L_T \cdot sin(q_1) \cdot sin(q_2) \cdot sin(q_3) \cdot sin(q_4) + \\
& + \frac{19}{100} \cdot cos(q_1) \cdot cos(q_2) \cdot cos(q_3) \cdot cos(q_4) \cdot cos(q_5) + \\
& - \frac{19}{100} \cdot cos(q_1) \cdot cos(q_4) \cdot cos(q_5) \cdot sin(q_2) \cdot sin(q_3)
\end{aligned}
\tag{B.6}
$$

$$
\begin{aligned}
J_{16} = \; & + L_T \cdot cos(q_1) \cdot sin(q_4) \cdot sin(q_5) + L_T \cdot cos(q_2) \cdot cos(q_5) \cdot sin(q_1) \cdot sin(q_3) + \\
& + L_T \cdot cos(q_3) \cdot cos(q_5) \cdot sin(q_1) \cdot sin(q_2) + \\
& + L_T \cdot cos(q_2) \cdot cos(q_3) \cdot cos(q_4) \cdot sin(q_1) \cdot sin(q_5) + \\
& - L_T \cdot cos(q_4) \cdot sin(q_1) \cdot sin(q_2) \cdot sin(q_3) \cdot sin(q_5)
\end{aligned}
\tag{B.7}
$$

$$
\begin{aligned}
J_{21} = \; & + \frac{13}{50} \cdot cos(q_1) + \frac{19}{20} \cdot cos(q_1) \cdot sin(q_2) - \frac{19}{100} \cdot sin(q_1) \cdot sin(q_4) \cdot sin(q_5) + \\
& + \frac{4}{5} \cdot cos(q_1) \cdot cos(q_2) \cdot sin(q_3) + \frac{4}{5} \cdot cos(q_1) \cdot cos(q_3) \cdot sin(q_2) + \\
& + \frac{19}{100} \cdot cos(q_1) \cdot cos(q_2) \cdot cos(q_5) \cdot sin(q_3) + \frac{19}{100} \cdot cos(q_1) \cdot cos(q_3) \cdot cos(q_5) \cdot sin(q_2) + \\
& + \frac{19}{100} \cdot cos(q_1) \cdot cos(q_2) \cdot cos(q_3) \cdot cos(q_4) \cdot sin(q_5) + \\
& - \frac{19}{100} \cdot cos(q_1) \cdot cos(q_4) \cdot sin(q_2) \cdot sin(q_3) \cdot sin(q_5)
\end{aligned}
\tag{B.8}
$$

$$
\begin{aligned}
J_{22} = \; & + \frac{1}{100} \cdot sin(q_1) \cdot \Big[\, 95 \cdot cos(q_2) + 80 \cdot cos(q_2) \cdot cos(q_3) - 80 \cdot sin(q_2) \cdot sin(q_3) + \\
& + 19 \cdot cos(q_2) \cdot cos(q_3) \cdot cos(q_5) - 19 \cdot cos(q_5) \cdot sin(q_2) \cdot sin(q_3) + \\
& - 19 \cdot cos(q_2) \cdot cos(q_4) \cdot sin(q_3) \cdot sin(q_5) - 19 \cdot cos(q_3) \cdot cos(q_4) \cdot sin(q_2) \cdot sin(q_5) + \\
& + L_T \, \Big]
\end{aligned}
\tag{B.9}
$$

$$
\begin{aligned}
J_{23} = & -\frac{1}{100} \cdot sin(q_1) \cdot \Big[\, 80 \cdot sin(q_2) \cdot sin(q_3) - 80 \cdot cos(q_2) \cdot cos(q_3) + \\
& - 19 \cdot cos(q_2) \cdot cos(q_3) \cdot cos(q_5) + 19 \cdot cos(q_5) \cdot sin(q_2) \cdot sin(q_3) + \\
& + 19 \cdot cos(q_2) \cdot cos(q_4) \cdot sin(q_3) \cdot sin(q_5) + 19 \cdot cos(q_3) \cdot cos(q_4) \cdot sin(q_2) \cdot sin(q_5) + \\
& - L_T \, \Big]
\end{aligned}
\tag{B.10}
$$

$$
\begin{aligned}
J_{24} = & +\frac{19}{100} \cdot cos(q_1) \cdot cos(q_4) \cdot sin(q_5) - L_T \cdot cos(q_1) \cdot cos(q_3) \cdot sin(q_2) + \\
& - L_T \cdot cos(q_1) \cdot cos(q_2) \cdot sin(q_3) - \frac{19}{100} \cdot cos(q_2) \cdot cos(q_3) \cdot sin(q_1) \cdot sin(q_4) \cdot sin(q_5) + \\
& + \frac{19}{100} \cdot sin(q_1) \cdot sin(q_2) \cdot sin(q_3) \cdot sin(q_4) \cdot sin(q_5)
\end{aligned}
\tag{B.11}
$$

$$
\begin{aligned}
J_{25} = & + L_T \cdot cos(q_4) \cdot sin(q_1) + \frac{19}{100} \cdot cos(q_1) \cdot cos(q_5) \cdot sin(q_4) + \\
& + L_T \cdot cos(q_1) \cdot cos(q_2) \cdot cos(q_3) \cdot sin(q_4) - L_T \cdot cos(q_1) \cdot sin(q_2) \cdot sin(q_3) \cdot sin(q_4) + \\
& - \frac{19}{100} \cdot cos(q_2) \cdot sin(q_1) \cdot sin(q_3) \cdot sin(q_5) - \frac{19}{100} \cdot cos(q_3) \cdot sin(q_1) \cdot sin(q_2) \cdot sin(q_5) + \\
& + \frac{19}{100} \cdot cos(q_2) \cdot cos(q_3) \cdot cos(q_4) \cdot cos(q_5) \cdot sin(q_1) + \\
& - \frac{19}{100} \cdot cos(q_4) \cdot cos(q_5) \cdot sin(q_1) \cdot sin(q_2) \cdot sin(q_3)
\end{aligned}
\tag{B.12}
$$

$$
\begin{aligned}
J_{26} = & + L_T \cdot sin(q_1) \cdot sin(q_4) \cdot sin(q_5) - L_T \cdot cos(q_1) \cdot cos(q_2) \cdot cos(q_5) \cdot sin(q3) + \\
& - L_T \cdot cos(q_1) \cdot cos(q_3) \cdot cos(q_5) \cdot sin(q_2) + \\
& - L_T \cdot cos(q_1) \cdot cos(q_2) \cdot cos(q_3) \cdot cos(q_4) \cdot sin(q_5) + \\
& + L_T \cdot cos(q_1) \cdot cos(q_4) \cdot sin(q_2) \cdot sin(q_3) \cdot sin(q_5)
\end{aligned}
\tag{B.13}
$$

$$
J_{31} = 0 \tag{B.14}
$$

$$\begin{aligned} J_{32} = & + \frac{19}{100} \cdot cos(q_4) \cdot sin(q_2) \cdot sin(q_3) \cdot sin(q_5) - \frac{4}{5} \cdot cos(q_2) \cdot sin(q_3) + \\ & - \frac{4}{5} \cdot cos(q_3) \cdot sin(q_2) - \frac{19}{100} \cdot cos(q_2) \cdot cos(q_5) \cdot sin(q_3) + \\ & - \frac{19}{100} \cdot cos(q_3) \cdot cos(q_5) \cdot sin(q_2) - \frac{19}{100} \cdot cos(q_2) \cdot cos(q_3) \cdot cos(q_4) \cdot sin(q_5) + \\ & - \frac{19}{20} \cdot sin(q_2) \end{aligned} \tag{B.15}$$

$$\begin{aligned} J_{33} = & + \frac{19}{100} \cdot cos(q_4) \cdot sin(q_2) \cdot sin(q_3) \cdot sin(q_5) - \frac{4}{5} \cdot cos(q_3) \cdot sin(q_2) + \\ & - \frac{19}{100} \cdot cos(q_2) \cdot cos(q_5) \cdot sin(q_3) - \frac{19}{100} \cdot cos(q_3) \cdot cos(q_5) \cdot sin(q_2) + \\ & - \frac{19}{100} \cdot cos(q_2) \cdot cos(q_3) \cdot cos(q_4) \cdot sin(q_5) - \frac{4}{5} \cdot cos(q_2) \cdot sin(q_3) \end{aligned} \tag{B.16}$$

$$J_{34} = + \frac{19}{100} \cdot sin(q_2 + q_3) \cdot sin(q_4) \cdot sin(q_5) \tag{B.17}$$

$$\begin{aligned} J_{35} = & + \frac{19}{100} \cdot sin(q_2) \cdot sin(q_3) \cdot sin(q_5) - \frac{19}{100} \cdot cos(q_2) \cdot cos(q_3) \cdot sin(q_5) + \\ & - \frac{19}{100} \cdot cos(q_2) \cdot cos(q_4) \cdot cos(q_5) \cdot sin(q_3) - \frac{19}{100} \cdot cos(q_3) \cdot cos(q_4) \cdot cos(q_5) \cdot sin(q_2) \end{aligned} \tag{B.18}$$

$$J_{36} = 0 \tag{B.19}$$

$$J_{41} = 0 \tag{B.20}$$

$$J_{42} = - sin(q_1) \tag{B.21}$$

$$J_{43} = - sin(q_1) \tag{B.22}$$

$$J_{44} = +sin(q_2+q_3)\cdot cos(q_1) \tag{B.23}$$

$$\begin{aligned} J_{45} = & +cos(q_1)\cdot sin(q_2)\cdot sin(q_3)\cdot sin(q_4) - cos(q_1)\cdot cos(q_2)\cdot cos(q_3)\cdot sin(q_4) + \\ & - cos(q_4)\cdot sin(q_1) \end{aligned} \tag{B.24}$$

$$\begin{aligned} J_{46} = & +cos(q_1)\cdot cos(q_2)\cdot cos(q_5)\cdot sin(q_3) - sin(q_1)\cdot sin(q_4)\cdot sin(q_5) + \\ & + cos(q_1)\cdot cos(q_3)\ \cdot cos(q_5)\cdot sin(q_2) + cos(q_1)\cdot cos(q_2)\cdot cos(q_3)\cdot cos(q_4)\cdot sin(q_5) + \\ & - cos(q_1)\cdot cos(q_4)\ \cdot sin(q_2)\cdot sin(q_3)\cdot sin(q_5) \end{aligned} \tag{B.25}$$

$$J_{51} = 0 \tag{B.26}$$

$$J_{52} = +cos(q_1) \tag{B.27}$$

$$J_{53} = +cos(q_1) \tag{B.28}$$

$$J_{54} = +sin(q_2+q_3)\cdot sin(q_1) \tag{B.29}$$

$$J_{55} = cos(q_1)\cdot cos(q_4) - cos(q_2)\cdot cos(q_3)\cdot sin(q_1)\cdot sin(q_4) + sin(q_1)\cdot sin(q_2)\cdot sin(q_3)\cdot sin(q_4) \tag{B.30}$$

$$\begin{aligned} J_{56} = & +cos(q_1)\cdot sin(q_4)\cdot sin(q_5) + cos(q_2)\cdot cos(q_5)\cdot sin(q_1)\cdot sin(q_3) + \\ & + cos(q_3)\cdot cos(q_5)\cdot sin(q_1)\cdot sin(q_2) + cos(q_2)\cdot cos(q_3)\cdot cos(q_4)\cdot sin(q_1)\cdot sin(q_5) + \\ & - cos(q_4)\cdot sin(q_1)\cdot sin(q_2)\cdot sin(q_3)\cdot sin(q_5) \end{aligned} \tag{B.31}$$

$$J_{61} = +1 \tag{B.32}$$

$$J_{62} = 0 \tag{B.33}$$

$$J_{63} = 0 \tag{B.34}$$

$$J_{64} = +cos(q_2 + q_3) \tag{B.35}$$

$$J_{65} = +sin(q_2 + q_3) \cdot sin(q_4) \tag{B.36}$$

$$\begin{aligned} J_{66} = {} & +cos(q_2) \cdot cos(q_3) \cdot cos(q_5) - cos(q_5) \cdot sin(q_2) \cdot sin(q_3) + \\ & - cos(q_2) \cdot cos(q_4) \cdot sin(q_3) \cdot sin(q_5) - cos(q_3) \cdot cos(q_4) \cdot sin(q_2) \cdot sin(q_5) \end{aligned} \tag{B.37}$$